Validating the surface flux ECUME and ECUME6 parameterizations used in the HARMONIE model

MSc. Thesis

Sophie van den Brekel

TU Delft

Koninklijk Nederlands Meteorologisch Instituut
Ministerie van Infrastructuur en Waterstaat

Validating the surface flux ECUME and ECUME6 parameterizations used in the HARMONIE model

MSc. Thesis

Thesis report

by

Sophie van den Brekel

to obtain the degree of Master of Science
at the Delft University of Technology
to be defended publicly on

Thesis committee:	Dr. A. A. Nuijens,
	Prof. dr. A. P. Siebesma,
	Dr. P. López-Dekker
	Dr. W. de Rooy
	Dr. N. Theeuwes
Place:	Faculty of CEG, Mechanical, Hydraulic Engineering, Delft
Student number:	4561397

Preface

The beginning of my MSc graduation thesis dates back to my time as a Hydraulic Engineering student when I took the elective course, Introduction to Meteorology. My interest in climate and the opportunity to contribute to new knowledge sparked my excitement for this topic. After participating in the course, I became even more interested and started exploring possible graduation topics in this area. A conversation with Louise about the importance of climate model validation further solidified my decision.

I had the privilege of carrying out this research in collaboration with the KNMI, specifically with the Research and Development of Weather and Climate models (RDWK) department. Being a part of their research group and department was inspiring, and I consider myself fortunate to have witnessed their impressive knowledge and passion for their field of study.

Understanding the complexity of parameterizations used in climate modeling, I was prepared for a challenging task. Although I had to familiarize myself with the data processing and terminology, I approached this research with enthusiasm, experiencing moments of both tears and laughter. Throughout the project, I learned a great deal both in terms of content and project management. This project demanded hard work, conducted from home, the Technical University of Delft and, fortunately, the headquarters of the KNMI. I would like to express my gratitude to everyone who has been part of this journey.

First and foremost, I am truly grateful to Louise for her endless patience, empathy, and support throughout the project. You have been supporting me since day one, and I have learned a lot from you. I would also like to thank Wim and Natalie for your expertise, assistance, and guidance during our joint exploration of model cycles. Additionally, I appreciate your warm welcome at the KNMI. My thanks go to Ingo as well, for providing me with the necessary data and helping me find solutions for the correction methodology, along with his valuable answers to my questions. Finally, I want to express my appreciation to Pier and Paco. It was an honor to receive your support, and I thoroughly enjoyed collaborating with you.

In addition to my graduation committee, the moral support from my family and friends helped me navigate through challenging times. I am grateful to my family for always being there to listen, offer advice, and remind me to take breaks when needed. Returning home after a productive day in De Bilt, to the warm welcome of my roommates was the best, and I thank them for patiently listening to my struggles with Python. Of course, I cannot forget to mention my friends who made my thesis period more enjoyable, including all the memorable moments at TU Delft.

As my student days in Delft come to a close, it is time to celebrate and eagerly anticipate the future! I can not wait to keep growing, taking on new challenges wherever they come my way.

Enjoy reading!

Sophie

Abstract

The exchange of energy and mass between the ocean and atmosphere plays a crucial role in shaping oceanic and atmospheric circulation patterns. However, accurately representing these air-sea fluxes remains a challenge for current weather and climate models. Improving the accuracy of bulk flux parameterizations is crucial to improve the quality of weather forecasts and climate predictions, as these parameterizations play a fundamental role in estimating the air-sea fluxes. This study aims to evaluate the performance of the ECUME and ECUME6 parameterizations in simulating air-sea fluxes by utilizing in situ observations obtained from R/V Ron Brown and R/V Meteor, and conducting a comparison with the COARE3.6 parameterization.

To evaluate the ECUME and ECUME6 parameterizations, surface flux diagnostics are established, which illustrate how air-sea fluxes vary with changes in the respective atmospheric variables. By comparing the surface flux diagnostics of the in situ observations with those of the parameterizations, sources of error are identified. The analysis reveals that both ECUME and ECUME6 tend to overestimate the heat fluxes in comparison to EC observations and the COARE3.6 parameterization, with ECUME6 exhibiting a larger overestimation. The degree of overestimation becomes more pronounced as wind speeds increase. Concerning the momentum flux, the parameterizations exhibit an underestimation, with the discrepancy becoming more significant at elevated wind speeds.

By employing an offline model for ECUME and COARE3.6, the iteratively obtained parameters are compared. This analysis demonstrates that the air-sea fluxes derived from the parameterizations strongly depend on the determined neutral transfer coefficients. Addressing these sources of error and refining the parameterization methodology can improve the accuracy of the parameterizations and enhance their applicability for estimating air-sea exchange between the Earth’s surface and the atmosphere.

Contents

Nomenclature

List of Symbols

α Charnock coefficient

β Constant used to define z_0, (COARE: 0.011, ECUME: 10^{-5})

β Roughness Reynolds number for smooth flow

$\Delta\theta$ Potential temperature gradient

$\Delta\theta_{10n}$ 10 m neutral potential temperature gradient

Δq Humidity gradient

Δq_{10n} 10 m neutral humidity gradient

Δu_{10n} 10 m neutral wind speed

κ von-Karman

R Position vector

T Coordinate transformation matrix

$\mathbf{V}_c$ Motion corrected wind

$\mathbf{V}_o$ Ship wind observations

$\mathbf{V}_{sh}$ Ship recorded speed

$\mathcal{L}_v$ Latent heat of vaporization

ν Air kinematic viscosity

Ω Angular velocity vector

ϕ roll

ψ yaw

ψ_h Heat stability function

ψ_m Wind stability function

ψ_q Moist stability function

$\mathcal{R}_d$ Specific dry air gas constant [287.0597 J/kg·K]

$\mathcal{R}_v$ Specific water vapor gas constant [461.525 J/kg·K]

ρ_a Atmospheric density

σ Standard deviation

τ Momentum flux, also referred to as surface stress

τ_x Zonal momentum flux

τ_y Meridional momentum flux

θ pitch

θ_a Air potential temperature

θ_s Surface potential temperature

θ_v Virtual potential temperature

θ_* Characteristic temperature scale

ε Ratio of gas constants for dry air to that for water vapor

ζ Stability parameter

AX Wind acceleration x direction

AY Wind acceleration y direction

AZ Wind acceleration z direction

Bo Bowen ratio

C_{D_n} Neutral drag coefficient

$C_{D_{10n}}$ 10 m neutral drag coefficient

C_D Drag transfer coefficient

C_{E_n} neutral moist transfer coefficient

$C_{E_{10n}}$ 10 m neutral moist transfer coefficient

C_E Moist transfer coefficient

C_{H_n} neutral temperature transfer coefficient

$C_{H_{10n}}$ 10 m neutral temperature transfer coefficient

C_H Temperature transfer coefficient

c_{p_a} Specific heat capacity of air [1004.70 J/kg·K]

CC — CO_2 density

CH — Water vapor concentration

e_o — Standard vapor pressure [0.611 kPa]

F — Turbulent flux density

g — Gravitational acceleration [9.80665 m^2/s]

L — Obukhov length scale

M_{H2O} — Molar mass of water vapor [18.015 g/mol]

P_0 — Constant reference pressure [1013.25 hPa]

P_a — Air pressure

P_s — Surface pressure

q_a — Air specific humidity

q_s — Surface saturation specific humidity

q_* — Characteristic humidity scale

Ri_b — Richardson bulk number

T_a — Air temperature

T_s — Sea surface temperature

T_v — Virtual temperature

T_o — Standard temperature [273.16 K]

T_{son} — Temperature from ultrasonic anemometer

U — Scalar wind speed relative to ocean current

u — Zonal wind velocity

u_z — Reference wind speed

u_* — Friction velocity

U_{10m} — 10 m scalar wind speed

v — Meridional wind velocity

w — Vertical wind velocity

X — Wind component x direction

x — Mixing ratio of a substance

Y — Wind component y direction

Z — Wind component z direction

z — Reference height

z_0 — Roughness length

z_{0_q} — Humidity roughness length

z_{0_t} — Heat roughness length

List of Abbreviations

Q_{LW} — Longwave radiative flux

Q_{SW} — Shortwave radiative flux

W_{AZ} — Vertical wind velocity from USAT

ADXL327 — Acceleration sensor

ATOMIC — Atmosphere Mesoscale Interaction Campaign

COARE — Coupled Ocean-Atmosphere Response Experiment

EC — Eddy covariance

LHF — Latent heat flux

LI-COR — Open-path gas analyzer LI-7500

MO — Monin-Obukhov Similarity Theory

NCEI — National Centers for Environmental Information

NED — North-East-Down

NOAA — National Oceanic and Atmospheric Administration

NWP — numerical weather prediction

PSL — Physical Sciences Lab

R/V — Research vessel

SEAPATH — Ship’s internal measurement system (DSHIP)

SHF — Sensible heat flux

TOGA — Tropical Ocean and Global Atmosphere

USAT2 — 3D ultrasonic anemometer Metek USA-2

WPL — Webb, Pearman, and Leuning

List of Figures

List of Tables

1 Introduction

The dynamic exchange of energy and mass between the ocean and atmosphere significantly influences the circulation patterns of the Earth's oceans and atmosphere. These exchanges, known as air-sea fluxes, play a crucial role in regulating the energy budget at the Earth's surface, ultimately influencing weather and climate conditions (Zhou et al., 2020). Weather and climate models rely on simulating these physical processes to make predictions about future weather and climate scenarios. However, despite extensive field studies, data-set advancements, and model enhancements, current models still face challenges in accurately simulating air-sea fluxes (Reeves Eyre et al., 2021). It is crucial to understand the performance of models in simulating air-sea fluxes and identify sources of errors to improve weather and climate predictions. The improvement in prediction accuracy would have significant economic implications for sectors such as agriculture, water management, energy management, and human and ecosystem health.

1.1. Research Relevance

In weather and climate models, bulk flux parameterizations, commonly known as bulk flux algorithms, are widely utilized to estimate air-sea fluxes by simulating the exchange between the near-surface layer of the atmosphere and the ocean. Numerous studies have demonstrated that the bulk flux parameterizations used in contemporary climate models tend to overestimate fluxes compared to direct flux measurements obtained from field observations (Brunke et al., 2003) (Hsu et al., 2022) (Zhou et al., 2020) (Pradhan et al., 2022). In order to enhance the accuracy of bulk flux parameterizations and reduce associated uncertainties, it is essential to conduct further investigations utilizing both field observations and numerical models. Since parameterizations play a critical role in determining the accuracy of bulk flux estimations, it is crucial to employ parameterizations that have been validated against observational data and continuously refine and enhance them as new information becomes available. These advancements will result in more accurate and reliable estimates of air-sea fluxes, which are essential for understanding and predicting climate variability and change.

To assess the performance of parameterizations, Hsu et al. (2022) developed a surface flux diagnostic. This diagnostic illustrates how air-sea fluxes vary with changes in respective atmospheric variables. The surface flux diagnostics are generated for both observational data and model output. By identifying areas in the diagnostic where differences between the simulated results and observations are greatest, developers can gain a better understanding of the uncertainties and strengths/weaknesses of the bulk parameterizations.

The Koninklijk Nederlands Meteorologisch Instituut (KNMI) is currently employing the Exchange Coefficients from Unified Multi-campaigns Estimates Version 6 (ECUME6) parameterization scheme in order to compute turbulent fluxes of momentum, heat, and water vapor. This parameterization scheme is employed in KNMI's operational model HARMONIE for weather forecasts and regional climate simulations. The ECUME6 scheme is an updated version of the ECUME version 5 parameterization scheme, referred to as ECUME hereafter. The ECUME parameterization scheme was developed through a multi-campaign calibration approach, while for ECUME6, new functions were created by incorporating additional observations. The disparities between these two versions lead to significant differences in the calculated air-sea fluxes, and hence an evaluation is required to assess their performance.

1.2. Research Objectives

The main research goal is to evaluate the accuracy of the ECUME and ECUME6 parameterizations in simulating air-sea fluxes, and to determine the predominant source of error in these parameterizations. The central research question is:

What level of accuracy is demonstrated by the ECUME and ECUME6 parameterizations in simulating air-sea fluxes, and what is the primary source of error identified in these parameterizations?.

The sub-questions that follow are:

1. How are air-sea fluxes simulated using the COARE3.6, ECUME and ECUME6 parameterizations and what are the main differences between these parameterizations?
2. What are the similarities and differences in air-sea flux determinations between the eddy covariance and COARE3.6 bulk method?
3. How do the results obtained from the ECUME and ECUME6 compare with the observed eddy covariance air-sea fluxes and with the COARE3.6 air-sea fluxes?
4. What are the main sources of error in the ECUME and ECUME6 parameterizations?

To address the research questions, a comparative analysis is conducted, involving multiple direct flux observations, COARE bulk results, and model results employing the ECUME and ECUME6 parameterizations. This analysis aims to enhance the understanding of the effectiveness of different parameterizations in accurately simulating air-sea fluxes. The in-situ observations are obtained through field measurements during the EURECA4A campaign. The performance of the parameterizations is assessed using the surface flux diagnostic introduced by Hsu et al. (2022). To ensure the reliability of the direct measurements utilized for the assessment, a comprehensive cross-comparison between in-situ measurements is conducted. Additionally, the reliability of the direct measurements is assessed by comparing them with COARE bulk results. Cross-comparisons between the ECUME and ECUME6 parameterizations are conducted to further identify their strengths and weaknesses. To identify the main source of error in the parameterizations, an offline model is constructed for both ECUME and COARE3.6. This enables a comparative analysis of the iteratively obtained parameters.

This research is a collaborative effort between the KNMI and the Delft University of Technology (TU Delft) as a component of the master's degree program in Civil Engineering. The project was initiated by the Research and Development of Weather and Climate models (RDWK) department at KNMI.

1.3. Report Outline

The initial chapter of this thesis establishes a theoretical framework in Chapter 2, aiming to enhance understanding of the operational principles of parameterizations and the diverse approaches used in their formulation. Chapter 3 outlines the data and methodology employed to compare the parameterizations with in-situ observations, including the necessary procedures for data correction. The subsequent chapter, Chapter 4, presents the results obtained from the comparison analysis. This is followed by an in-depth discussion in Chapter 5, highlighting the associated implications and interpretations. Finally, Chapter 6 concludes the thesis by summarizing the key findings and providing recommendations based on the study outcomes.

2

Theoretical background

Bulk flux parameterizations are widely employed in estimating air-sea fluxes, which entail the transfer of heat, moisture, and momentum between the ocean and atmosphere. These parameterizations model the interplay between the thin surface layer of the air and the sea. There are several different formulations of bulk parameterization that differ in their stability functions and roughness length formulations, among other factors. The choice of transfer coefficient formulation used in the bulk parameterization introduces uncertainty in the estimation of air-sea fluxes. Additionally, the estimation of air-sea fluxes is complicated by the treatment of state variables. In-situ measurements of oceanic near-surface state variables are typically below the ocean skin and need to be extrapolated to the air-sea interface, which may lead to errors in flux estimation (Cronin et al., 2019). To reduce these errors, efforts are being made to improve the accuracy of in-situ measurements of near-surface state variables and to develop more sophisticated models that can better capture the complex dynamics of the air-sea interface. This improvements could lead to an enhanced comprehension of the Earth's climate system, and hence, facilitate more accurate predictions of its future behavior (Yu Xiangze Jin Robert Weller, 2008).

2.1. Air-Sea Fluxes

Solar radiation absorbed by the ocean's surface causing the evaporation of seawater. The produced warm water vapor exhibits positive buoyancy due to its lower density compared to the surrounding air. This positive buoyancy drives the upward movement of the warm vapor, initiating atmospheric convection. Convection, in turn, sets air masses in motion, impacting the formation, movement, and characteristics of clouds, precipitation, and other weather phenomena. Consequently, atmospheric convection plays a crucial role in controlling weather patterns and the overall dynamics of the atmosphere-ocean system (Cronin et al., 2019).

To develop accurate weather and climate models and deepen our understanding of the physical processes occurring in the atmosphere and ocean, it is essential to consider the coupling that occurs at the air-sea interface. By accounting for the interactions and exchanges happening at the air-sea interface, the representation of convection in models can be refined, leading to improved predictions of weather patterns and climate behavior (Drennan, 2006). The net heat flux at the air-sea interface encompasses various components, including radiative and turbulent terms. It consists of the net shortwave (Q_{SW}) and net longwave (Q_{LW}) terms, along with the latent heat flux (LHF) and sensible heat flux (SHF):

$$Q_{\text{net}} = Q_{SW} - Q_{LW} - LHF - SHF \tag{2.1}$$

The majority of solar energy is absorbed by the Earth's oceans. This energy can only contribute to atmospheric circulation through turbulent fluxes of momentum, latent heat and sensible heat. Latent heat flux is produced when seawater evaporates and the extracted heat is released to the atmosphere, leading to cloud formation as the released heat condenses. Sensible heat flux arises due to the thermal gradient between the air and the ocean, leading to the transfer of heat from the ocean to the atmosphere. In addition to the sensible and latent heat fluxes, the surface momentum (also known as wind stress) imposes surface boundary conditions for turbulent flux profiles in the lower atmosphere and upper ocean (Cronin et al., 2019). Momentum fluxes arising from the interactions between the atmosphere and the ocean create drag on atmospheric motions, which subsequently generates the wind-driven component of ocean currents

(Lykossov, 2009). The surface turbulent fluxes of momentum, latent heat, and sensible heat are of critical importance in determining the energy exchange at the ocean surface. The surface layer, defined as the lowest 10% of the boundary layer, located in close proximity to the ocean, is the region where the surface fluxes are determined (Siebesma et al., 2020). These fluxes can be assessed directly using the eddy covariance method or through the utilization of bulk flux parameterizations. The latter approach connects turbulent fluxes to mean air-sea velocity, temperature, and humidity gradients using transfer coefficients. Further explanations of these methods are provided in subsequent chapters (Chapter 2.2 and 2.3).

2.2. Eddy Covariance

The underlying principle of flux measurement involves the quantification of the number of molecules moving in upward and downward directions over a specified period, as well as the speed at which they travel. The most straightforward approach to determine surface turbulent fluxes involves the use of the eddy covariance (EC) method. This method measures the direct covariance between the fluctuating vertical velocity (i.e., the up and down movements) that drives the exchange, and the fluctuating quantity of interest (Burba & Anderson, 2010). In order to capture all scales contributing to the flux, it is imperative to sample turbulent signals at a sufficiently high frequency and for a long enough duration. For typical measurement heights and wind speeds, sampling frequency and time series length of orders 10 Hz and 20 min are recommended (Drennan, 2006). Vertical flux in turbulent flow can be expressed using the equation:

$$F = \overline{\rho_{\mathrm{a}}}\,\overline{w'x'} \tag{2.2}$$

Here, F represents the turbulent flux density of a substance, where the quantity of interest is described by its atmospheric density (ρ_a), wind speed in the direction of interest (w), and the mixing ratio of the substance (x). The Reynolds decomposition method is employed to separate the three turbulent parameters into their respective mean steady state (represented by the overbar) and turbulent deviation (represented by the prime) from the mean state. The resulting expression can be written as in Eq. 2.3:

$$\begin{aligned} F &= \overline{\left(\overline{\rho_a} + \rho_a'\right)\left(\bar{w} + w'\right)\left(\bar{x} + x'\right)} \\ &= \overline{\left(\overline{\rho_a}\bar{w}\bar{x} + \overline{\rho_a}\bar{w}x' + \overline{\rho_a}w'\bar{x} + \overline{\rho_a}w'x' + \rho_a'\bar{w}\bar{x} + \rho_a'\bar{w}x' + \rho_a'w'\bar{x} + \rho_a'w'x'\right)}. \end{aligned} \tag{2.3}$$

In this equation, the average of a deviation equals zero. With the assumptions of the EC method, which include neglecting air density fluctuations and assuming negligible mean vertical flow, Eq. 2.3 is simplified to the classical equation for eddy flux, as presented below:

$$F = \overline{\rho_{\mathrm{a}}}\,\overline{w'x'} \tag{2.4}$$

The classical equation for eddy flux is utilized to calculate the zonal ($|\tau_x|$) and meridional ($|\tau_y|$) momentum flux, sensible heat flux (SHF), and latent heat flux (LHF) for air-sea fluxes.

$$\begin{aligned} |\tau_x| &= \rho_a \left(\overline{w'u'}\right)_s \\ |\tau_y| &= \rho_a \left(\overline{w'v'}\right)_s \\ SHF &= \rho_a c_{p_a} \left(\overline{w'\theta'}\right)_s \\ LHF &= \rho_a \mathcal{L}_v \left(\overline{w'q'}\right)_s \end{aligned} \tag{2.5}$$

where ρ_a is the density of air; c_{p_a} is the specific heat capacity of air at constant pressure, equal to 1004.70 J/kg·K); $\mathcal{L}_v$ is the latent heat of vaporization; u is the zonal wind velocity; v is the meridional wind velocity; θ is the potential temperature; w represents the vertical wind velocity and q the specific humidity. The s index stands for sea surface variables whereas the a index stands for atmospheric variables at the measurement's height (Le Moigne, 2018). The measurement of fluxes over the ocean is challenging and expensive, especially when considering the necessary time and spatial scales required for model input. In addition, difficulties such as flow distortion and platform motion contamination can impact the accuracy of direct measurements of turbulent fluxes at sea. Consequently, accurate motion correction is necessary for accurate EC measurements. Due to these difficulties, air-sea fluxes have historically been parameterized based on available state variables and bulk transfer coefficients. The pursuit of precise flux parameterizations has been a longstanding objective in the field of air-sea interaction research. By assessing bulk fluxes with direct EC measurements, these parameterizations have undergone updates, moving away from earlier attempts that relied on constant bulk transfer coefficients (Drennan, 2006).

2.3. Bulk Flux Parameterizations

Bulk flux parameterizations are frequently employed to estimate air-sea fluxes. In these parameterizations, vertical gradients of wind, potential temperature, and specific humidity are linked to the air-sea fluxes using empirically generated bulk transfer coefficients. The vertical profile gradients are determined by comparing the mean state variables measured (or modeled) at the sea surface with those measured at a specific height within the surface layer. The bulk air-sea fluxes are then derived from:

$$\tau_x = \rho_a C_D U \Delta u, \quad \tau_y = \rho_a C_D U \Delta v, \tag{2.6}$$

$$SHF = \rho_a c_{p_a} C_H U \Delta\theta \tag{2.7}$$

$$LHF = \rho_a \mathcal{L}_v C_E U \Delta q \tag{2.8}$$

where C_D, C_H and C_E are the transfer coefficients for momentum, sensible heat and latent heat, refed to as the drag, temperature and moist transfer coefficients; U is the scalar wind speed relative to the ocean surface; and Δu, Δv, Δq and $\Delta\theta$ are the zonal wind, meridional wind, humidity and potential temperature mean meteorological gradients (Cronin et al., 2019). In the field of boundary layer meteorology, the parameterized expressions of transfer coefficients are derived using the principles of Monin-Obukhov Similarity Theory (MOST). This widely utilized theory assumes constant air-sea fluxes in the surface layer and establishes a relationship between the vertical profiles of mean meteorological variables and the turbulent fluxes present within the surface layer. MOST can be viewed as an extension of the concept of wall scaling for turbulent shear flows, accounting for unstable or stable thermal stratification, where buoyancy influences the production or dissipation of turbulent kinetic energy and modifies the mean velocity profile in the atmospheric surface layer (Salesky, 2014).

The central hypothesis of MOST is that the statistical behavior of turbulence in the surface layer is dominated by characteristic scales, commonly known as scaling parameters, which are associated with shear. These scales are characterized by the friction velocity (u_*), which quantifies the magnitude of turbulent wind fluctuations (Eq. 2.9), the characteristic temperature scale (θ_*), which represents the magnitude of turbulent fluctuations in moisture content (Eq. 2.10), and the characteristic humidity scale (q_*), which signifies the magnitude of turbulent fluctuations in temperature (Eq. 2.11) (C. W. Fairall et al., 1996).

$$u_*^2 = -\left(\overline{w'u'}\right)_s \tag{2.9}$$

$$\theta_* = -\frac{\left(\overline{w'\theta'}\right)_s}{u_*} \tag{2.10}$$

$$q_* = -\frac{\left(\overline{w'q'}\right)_s}{u_*} \tag{2.11}$$

2.3.1. Turbulent Transfer in the Surface Layer: Neutral Atmospheric Conditions

According to the central hypothesis of MOST, which assumes that scales related to the mean shear govern the characteristics of turbulence in the surface layer, the theory is applicable under two specific conditions. Firstly, it is valid in the region near the surface, where the turbulent processes are directly influenced by the immediate surface conditions. Secondly, it is applicable in the region where the shear production of turbulent kinetic energy outweighs the buoyant production, indicating that shear-driven processes dominate the turbulence dynamics in that region and buoyancy forces are negligible (Salesky, 2014). This represents the simplest form of turbulent transfer in the surface layer, observed under neutral conditions, where the upward and downward motions of air parcels are in balance. In this scenario, turbulence is solely driven by shear production, characterized by the friction velocity (u_*) and height above the surface (z) (Siebesma et al., 2020). As a consequence, the non-dimensional equation governing turbulence kinetic energy (TKE) can be simplified to the wind flux-gradient relation:

$$\frac{\partial U}{\partial z} = \frac{u_*}{\kappa z} \tag{2.12}$$

where the κ is the von-Karman constant for which a measured value of approximately 0.4 has been found. By integrating Equation 2.12 from the roughness length (z_0) to the reference height (z) and solving for a general level z and wind speed u, the logarithmic wind speed profile can be obtained:

$$U = \frac{u_*}{\kappa} \ln\left(\frac{z}{z_0}\right) \tag{2.13}$$

The roughness length (z_0), is defined as the height above ground for which the wind speed equals zero (Venora, 2009). By following a similar approach as for wind, flux-gradient expressions for the gradients of potential temperature ($\Delta\theta$) and humidity (Δq) can be derived. These expressions are shown in Equation 2.14 and Equation 2.15 respectively. Under neutral conditions, both temperature and humidity exhibit logarithmic profiles. The roughness lengths, denoted as z_{0_t} and z_{0_q} are defined as the height at which the extrapolation of the logarithmic portion of the respective profile intersects the surface value, similar to z_0. These roughness lengths characterize the influence of surface roughness on the potential temperature and humidity profiles (C. W. Fairall et al., 1996).

$$\theta_a - \theta_s = \frac{\theta_*}{\kappa} \ln\left(\frac{z}{z_{0_t}}\right) \tag{2.14}$$

$$q_a - q_s = \frac{q_*}{\kappa} \ln\left(\frac{z}{z_{0_q}}\right) \tag{2.15}$$

By rearranging the logarithmic profile equations, the formulation for the neutral transfer coefficients can be obtained:

$$C_{D_n} = \frac{\kappa^2}{\left[\ln\left(\frac{z}{z_0}\right)\right]^2} \tag{2.16}$$

$$C_{H_n} = \frac{\kappa^2}{\ln\left(\frac{z}{z_0}\right)\ln\left(\frac{z}{z_{0_t}}\right)} \tag{2.17}$$

$$C_{E_n} = \frac{\kappa^2}{\ln\left(\frac{z}{z_0}\right)\ln\left(\frac{z}{z_{0q}}\right)} \tag{2.18}$$

where C_{D_n} is the neutral drag coefficient, C_{H_n} is the neutral temperature transfer coefficient and C_{E_n} represents the neutral moist transfer coefficient. The formulation of these coefficients has been derived assuming neutral conditions.

2.3.2. Turbulent Transfer in the Surface Layer: Unstable and Stable Conditions

In the presence of stable or unstable atmospheric conditions, the flux-gradient relationship (Eq. 2.12) is influenced by the surface buoyancy flux. Monin-Obukhov Similarity Theory proposes that the dimensionless gradients of velocity, temperature and humidity within the surface layer can be described by universal gradient functions (ϕ) that are functions of a dimensionless scaling parameter (ζ). This scaling parameter only depends on the friction velocity (u_*), height (z), and the buoyancy flux. u_*, z and the buoyancy flux can be represented by a single parameter (L), known as the Obukhov length scale. The Obukhov length scale, given in Eq. 2.19, represents the height above the surface at which buoyancy production becomes dominant over shear production.

$$L = \frac{-u_*^3}{\kappa \frac{g}{\theta_v}\left(\overline{w'\theta_v'}\right)_s} \tag{2.19}$$

In Eq 2.19, θ_v and $\overline{w'\theta_v'}$ are the virtual potential temperature and near-surface buoyancy flux, respectively and g is the gravitational acceleration. L is positive for stable conditions, negative for convective conditions, and infinite for neutral conditions (Siebesma et al., 2020). By employing Eq. 2.20 and 2.21, the Obukhov length scale can be formulated as a function of the characteristic scales, air temperature (T_a) and air specific humidity (q_a) (Le Moigne, 2018):

$$\theta_v = \theta_a\left(1.0 + 0.61 q_a\right) \tag{2.20}$$

$$\theta_{v*} = -\frac{\left(\overline{w'\theta_v'}\right)_s}{u_*} = \theta_*\left(1.0 + 0.61 q_a\right) + 0.61\left(\theta_a q_*\right) \tag{2.21}$$

$$L \approx \left(\frac{u_*^2}{\kappa . g}\right)\left[\frac{T_a\left(1.0 + 0.61 q_a\right)}{\theta_*\left(1.0 + 0.61 q_a\right) + 0.61\left(T_a q_*\right)}\right] \tag{2.22}$$

The scaling parameter (ζ) is defined as $\zeta = z/L$, and it is commonly referred to as a stability parameter, providing information about the stability of the atmosphere at height z within the surface layer. Using

MOST, the flux-gradient relationships derived for neutral conditions can be extended to diverse atmospheric conditions by incorporating universal gradient functions, ϕ_m, ϕ_h and ϕ_q, as unique functions of ζ, to account for the stratification of the atmosphere (Siebesma et al., 2020). As result, gradients of the profiles of wind velocity (u), potential temperature (θ), and humidity (q) within the surface layer can be expressed by the following equations:

$$\frac{\partial U}{\partial z}\frac{\kappa z}{u_*} = \phi_m\left(\frac{z}{L}\right) \tag{2.23}$$

$$\frac{\partial \theta}{\partial z}\frac{\kappa z}{\theta_*} = \phi_h\left(\frac{z}{L}\right) \tag{2.24}$$

$$\frac{\partial q}{\partial z}\frac{\kappa z}{q_*} = \phi_q\left(\frac{z}{L}\right) \tag{2.25}$$

The profile relations can be derived by integrating equations 2.23 to 2.25, resulting in the following expressions:

$$U = \frac{u_*}{\kappa}\left[\ln\left(\frac{z}{z_0}\right) - \psi_m\left(\frac{z}{L}\right)\right] \tag{2.26}$$

$$\theta_a - \theta_s = \frac{\theta_*}{\kappa}\left[\ln\left(\frac{z}{z_{0_t}}\right) - \psi_h\left(\frac{z}{L}\right)\right] \tag{2.27}$$

$$q_a - q_s = \frac{q_*}{\kappa}\left[\ln\left(\frac{z}{z_{0q}}\right) - \psi_q\left(\frac{z}{L}\right)\right] \tag{2.28}$$

Where, ψ_m, ψ_h and ψ_q are stability functions, related through the gradient functions through $\phi = 1 - \zeta(\partial\psi/\partial\zeta)$. As a result, $\psi > 0$ for unstable conditions and $\psi < 0$ for stable conditions. In non-neutral situations, deviations from the logarithmic wind profile can be observed. In stable boundary layers, the turbulence is insufficient to fully mix the surface layer, causing decoupling between the winds above the surface layer and the drag at the ground. This decoupling results in a slightly concave downward shape of the wind profile when plotted on a semi-logarithmic scale. Conversely, in unstable boundary layers, the presence of intense turbulence under unstable conditions leads to a more rapid increase in wind speed with height. This generates a concave upward shape of the wind profile, as illustrated in Figure 2.1 (Stull, 1988). These deviations from the logarithmic profile indicate the influence of stability functions on the vertical distribution of wind within the boundary layer. Numerous semi-empirical stability functions have been developed based on the investigation of flux-gradient relationships in experiments. The prevailing forms typically combine the Businger-Dyer formulae along with a formulation that conforms to the theoretical scaling limit (Edson et al., 2004). It is commonly assumed that the flux-gradient relationships for moisture are equivalent to those for heat, resulting in $\psi_h = \psi_q$. This assumption implies that the vertical gradients of moisture and heat within the boundary layer follow the same pattern and can be described by the same universal functions.

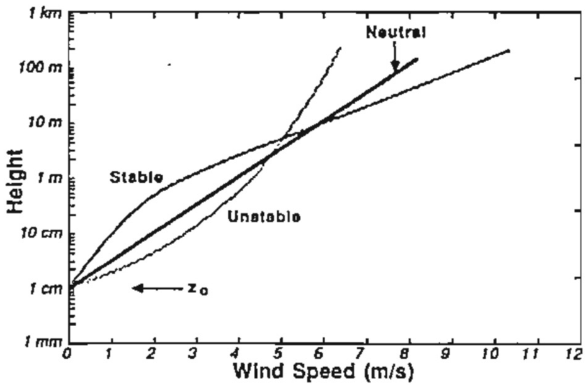

Figure 2.1: Typical wind speed profiles vs. statistic stability in the surface layer Stull (1988)

Now, the transfer coefficients can be parameterized as function of atmospheric stability and surface roughness as:

$$C_D = \frac{\kappa^2}{\left[\ln\left(z/z_0\right) - \psi_\mathrm{m}(\xi)\right]^2} \tag{2.29}$$

$$C_H = \frac{\kappa^2}{\left[\ln\left(z/z_0\right) - \psi_{\mathsf{m}}(\xi)\right]\left[\ln\left(z/z_{0_t}\right) - \psi_{\mathsf{h}}(\xi)\right]} \tag{2.30}$$

$$C_E = \frac{\kappa^2}{\left[\ln\left(z/z_0\right) - \psi_{\mathsf{m}}(\xi)\right]\left[\ln\left(z/z_{0_q}\right) - \psi_{\mathsf{q}}(\xi)\right]} \tag{2.31}$$

Using Eq. 2.26 to 2.3.2, the transfer coefficients can be expressed as functions of the characteristic scales (Le Moigne, 2018):

$$C_D = \left(\frac{u_*}{U}\right)^2 \tag{2.32}$$

$$C_H = \frac{u_*\theta_*}{U\left(\theta_a - \theta_s\right)} \tag{2.33}$$

$$C_E = \frac{u_* q_*}{U\left(q_a - q_s\right)} \tag{2.34}$$

Figure 2.2 depicts the wind speed-dependent variations of the drag coefficient (C_D), temperature coefficient (C_H), and moisture coefficient (C_E) at a measurement height of 10 m over ocean surfaces, where the surface temperature exceeds the atmospheric temperature. As the wind speed surpasses 5 m/s, both C_H and C_E exhibit a gradual decline, while C_D experiences an increase. In oceanic environments, higher wind speeds correspond to increased drag. Conversely, higher wind speeds are associated with less unstable atmospheric conditions, leading to a reduction in heat and moisture transfer. For very low wind speeds, the vertical turbulent transport between the ocean surface and the air is primarily governed by convective thermals rather than the wind speed itself (Wallace & Hobbs, 2006).

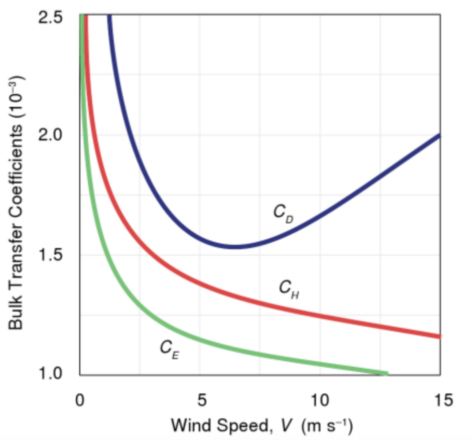

Figure 2.2: Variation of bulk transfer coefficients for drag (C_D), temperature (C_H) and moist (C_E) with wind speed, adopted from Wallace and Hobbs (2006)

As shown in this Chapter, the transfer coefficients are parameterized to account for the effects of the two primary sources of turbulence, namely atmospheric stability and ocean surface roughness. The existing bulk parameterizations vary in their definitions of stability functions and how they parameterize roughness lengths (z_0, z_{0_t} and z_{0_q}) and eventually determine the transfer coefficients (C_D, C_H and C_E). Additional variations entail whether the impact of seawater salinity is taken into account, whether convective turbulence is considered during low wind velocities, and whether the diurnal effects of the cool skin and warm layer are accounted for. All of these factors collectively contribute to the variations observed in the fluxes calculated by the different parameterizations. Significant efforts have been made in the past decades to determine accurate bulk parameterizations. To further verify and enhance existing parameterizations, direct covariance flux observations must be utilized (Brunke et al., 2003).

2.3.3. The COARE Parameterization

In 1996, version 2.5 of the Coupled Ocean-Atmosphere Response Experiment (COARE) bulk parameterization was published, which has since become one of the most widely used parameterizations in the air-sea interaction community C. W. Fairall et al. (2003). The COARE parameterization (often referred to as

COARE bulk algorithm) was initially developed during the Tropical Ocean and Global Atmosphere (TOGA) experiment. The TOGA-COARE campaign aimed to investigate the influence of warm-pool regions in the tropics on the average and transitional state of the tropical ocean-atmosphere system. This field campaign was conducted in the western Pacific warm-pool region, spanning from 20°N to 20°S and bordered by Indonesia to the west and the International Date Line to the east (NCAR, 2023). Since the inception of COARE2.5, the parameterization has undergone progressive enhancements driven by the utilization of data from the ETL1999 database, as presented in Table B.1 in Appendix B. These improvements have resulted in the development of the latest version, COARE3.6.

The COARE parameterization employs the standard Monin-Obukhov Similarity (MOST) approach for near-surface meteorological measurements, as described in Chapter 2.3, but incorporates separate models for the ocean's cool skin and the diurnal warm layer. These models are utilized to estimate the true skin temperature based on the bulk temperature measurements obtained at some depth near the surface (C. W. Fairall et al., 1996). Since the establishment of the COARE parameterization, various enhancements have been incorporated into the parameterization. These include corrections for gustiness, a 2% reduction in water vapor pressure over seawater and improvements to stability functions. Furthermore, wave parameterization techniques have been incorporated into the calculation of surface roughness, taking into account the effects of waves on the airflow close to the surface. This integration allows for the inclusion of wave-induced changes in surface roughness, which in turn affects turbulent processes. However, the evaluation of this approach has been limited due to the lack of extensive availability of detailed wave data. Notwithstanding, the COARE3.6 parameterization has achieved significant improvements, yielding an accuracy of within 5% for wind speeds ranging from 0 to 10 m/s and within 10% for wind speeds between 10 and 20 m/s, as reported by C. W. Fairall et al. (2003).

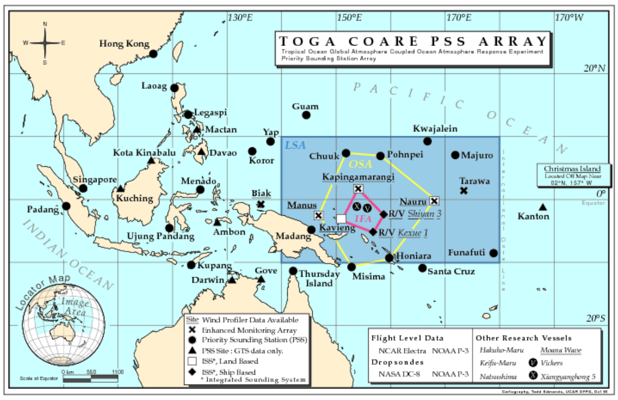

Figure 2.3: Composite structure of the TOGA-COARE campaign, adopted from NCAR (2023)

The COARE parameterization incorporates the parameterization of surface roughness (z_0). To accurately parameterize z_0, direct measurements are utilized. The following steps are undertaken to formulate the parameterized z_0: Initially, the characteristic scales are determined from the direct measurements of fluxes, utilizing Equations 2.9 to 2.11. These characteristic scales are then used to calculate the Monin-Obukhov length, which is subsequently used to compute the stability parameter $\zeta = z/L$. Then, the stability parameter is employed in the stability functions. As discussed in Chapter 2.3, semi-empirical stability functions have been derived through experimental investigations of flux-gradient relationships. Initially, the COARE2.5 parameterization incorporated the Kansas stable profile functions (Businger et al., 1971). However, in the more recent COARE3.6 version, these functions have been replaced with those developed by Beljaars and Holtslag (Godfrey & Beljaars, 1991), which are based on new profile data fitting. In COARE3.6, the unstable profile functions still incorporate the Kansas and free convection forms. However, compared to the original COARE2.5 parameterization, the empirical constants in these functions have been modified (C. W. Fairall et al., 2003). The stability functions used in COARE3.6 are presented in Table D.1 in Appendix D.

From the direct measurements of fluxes, the transfer coefficients can be determined using the expression:

$$C_X = \frac{-\overline{w'x'}}{U\Delta x} \tag{2.35}$$

where x represents the quantity of interest. By combining the direct measurements of fluxes with the stability-corrected wind speeds, the neutral transfer coefficients can be obtained. The neutral drag coefficient (C_{D_n}) is then defined as:

$$C_{D_n}(z/z_0) = \frac{-\overline{uw}}{U_n^2} = \left[\frac{\kappa}{\ln(z/z_0)}\right]^2 \tag{2.36}$$

where the subscript n indicates neutral atmospheric stratification. Subsequently, the obtained neutral drag coefficients can be employed to develop parameterizations of flux in terms of the roughness length (z_0). In COARE, the obtained parameterization of z_0 involves the Charnock relation, plus a smooth flow limit (Edson et al., 2013):

$$z_0 = \alpha\left(\frac{u_*^2}{g}\right) + \beta\left(\frac{\nu}{u_*}\right) \tag{2.37}$$

Where α is the Charnock coefficient, accounting for a diverse range of physical phenomena that affect the interaction between wind and waves, β is the roughness Reynolds number for smooth flow, and ν is the air kinematic viscosity, computed as a function of the air temperature T_a: $\nu = 1.31810^{-5} + 9.28210^{-8}T_a$. Experimental studies have determined β to be equal to 0.11. The Charnock coefficient (α) was initially known as the Charnock constant, with a fixed value of 0.011. However, further research has shown that the Charnock coefficient is not constant but instead varies depending on factors such as wind speed, wave age, and sea state. Therefore, a wind-dependent formulation is introduced for the Charnock coefficient, as follows (Le Moigne, 2018):

$$\begin{array}{ll} \alpha = 0.011 & \text{if } 0\ \mathrm{m.s^{-1}} \le U \le 10\ \mathrm{m \cdot s^{-1}} \\ \alpha = 0.011 + (0.018 - 0.011)\left(\frac{U-10}{18-10}\right) & \text{if } 10\ \mathrm{m.s^{-1}} < U \le 18\ \mathrm{m \cdot s^{-1}} \\ \alpha = 0.018 & \text{if } 18\ \mathrm{m.s^{-1}} < U \end{array} \tag{2.38}$$

The roughness lengths for temperature and humidity, z_{0_t} and z_{0_q}, are directly derived from z_0 using:

$$z_{0_t} = z_{0_q} = MIN\left(1.1510^{-4}, 5.510^{-5}\left(\frac{\nu}{z_0 u_*}\right)^{0.6}\right) \tag{2.39}$$

The COARE3.6 parameterization follows a series of steps for its execution. Initially, the required variables are initialized. This involves defining the vertical gradients and obtaining an initial estimate of the parameterized roughness length (Eq. 2.37) based on an initial estimation of u_*. The stability parameter is then set using a first guess derived from the bulk Richardson number (Ri_b), providing a robust estimate of stability. With this initial guess, the first estimates for the characteristic scales can be obtained by rearranging Eq. 2.26 to 2.3.2. The parameterization proceeds with an iterative procedure. In each iteration, the roughness lengths are updated, followed by the calculation of the Monin-Obukhov length using Eq. 2.22. Using the obtained value of L, the stability parameter is updated, and subsequently, the characteristic scales are updated using the stability functions. This iterative process continues for a total of 10 iterations. The iteratively determined characteristic scales are used to calculate the transfer coefficients (Eq. 2.32 to 2.34). Finally, these transfer coefficients are utilized to compute the fluxes (Eq. 2.6 to 2.8) (Bariteau, 2023). The process of initializing all the necessary variables, iteratively determining the variables, and calculating the air-sea fluxes is outlined in Appendix A of this study. The flow-chart provides a visual representation of the sequential steps involved in the COARE3.6 parameterization. However, it is important to note that the flow-chart does not include any possible corrections that may be applied during the process.

2.3.4. The ECUME and ECUME6 Parameterization

The ECUME (Exchange Coefficients from Unified Multi-campaigns Estimates) parameterization is an iterative parameterization developed at the Centre National de Recherches Météorologiques (CNRM) to optimize parameterization that can cover a wide range of atmospheric and oceanic conditions. Similar to COARE, the Monin-Obukhov Similarity (MOST) approach is employed (Le Moigne, 2018). Within the SURFEX scheme, there are two iterative parameterization versions available: ECUME and its updated version, ECUME6. SURFEX is a surface modeling platform developed by Météo-France in collaboration with the scientific community. It consists of multiple physical models that represent different types of surfaces such as natural land surface, urbanized areas, lakes, and oceans. In addition to surface modeling, SURFEX also incorporates processes related to chemistry and aerosols, and it can be utilized for assimilating surface and near-surface variables (CNRM, 2023). The ECUME parameterization, employed in SURFEX, is based on an extensive database called ALBATROS, which encompasses 10 years of research spanning from the early 1990s to 2001. The database includes data collected from five dedicated experiments focused on air-sea fluxes, namely SEMAPHORE, CATCH, FETCH, EQUALANT99, and POMME. These experiments were conducted in the Atlantic Ocean (from the Northern to the equatorial regions) and the Mediterranean Sea (Belamari, 2005). A synthesis paper by Weill et al. (2003) provides a comprehensive overview of these experiments.

From the measurement campaigns, the drag coefficients, which is obtained from the directly measured fluxes, and the measured wind speed are both adjusted to a height of 10 m and neutral stratification using:

$$C_{D_{10n}} = \frac{-\overline{uw}}{\Delta u_{10n}^2} \tag{2.40}$$

$$C_{H_{10n}} = \frac{-\overline{u\theta}}{\Delta u_{10n} \cdot (T_s - T_{a,10m})} \tag{2.41}$$

$$C_{E_{10n}} = \frac{-\overline{uq}}{\Delta u_{10n} \cdot (q_s - q_{a,10m})} \tag{2.42}$$

Here, Δu_{10n} represents the 10 m neutral wind speed, $C_{D_{10n}}$, $C_{H_{10n}}$ and $C_{E_{10n}}$ represent the 10 m neutral drag, temperature, and moist transfer coefficients, respectively, and T_s represents the sea surface temperature (Weill et al., 2003). This approach is similar to the method used in COARE, as described in Chapter 2.3.3, where the neutral drag coefficient is obtained from measurements to eventually parameterize the roughness length, using Eq. 2.36. However, in ECUME, the obtained neutral transfer coefficients are not used for the explicit parameterization of the roughness length. Instead, the mean transfer coefficients and their associated standard deviations are computed for specific 10 m wind speed intervals (with a bin size of 2 m/s). Through calibration, polynomial functions are derived to characterize the relationship between the neutral transfer coefficients and the vertical wind gradient from the sea surface to the 10 m height (Belamari, 2005). Consequently, the neutral transfer coefficients in the ECUME scheme are defined as functions of the neutral vertical wind gradient between the sea surface and the 10 m height:

$$C_{D_{10n}} = f_u\left(\Delta u_{10n}\right) \tag{2.43}$$

$$C_{H_{10n}} = f_\theta\left(\Delta u_{10n}\right) \tag{2.44}$$

$$C_{E_{10n}} = f_q\left(\Delta u_{10n}\right) \tag{2.45}$$

These polynomial functions, denoted as f_x, exhibit a maximum value above a specific wind threshold. The resulting formulations for the neutral transfer coefficients used in ECUME can be found in Table 2.1. By adopting this methodology, ECUME does not explicitly parameterize or calculate the roughness length as an independent variable. Instead, it relies on the assumption that the roughness length (z_0) can be deduced from the 10-meter wind measurements.

ECUME6, being the updated version of ECUME, uses empirical functions g_u of the 10 m wind speed under neutral conditions to compute three intermediate parameters $P_{u_{10n}}$, $P_{\theta_{10n}}$ and $P_{q_{10n}}$, which are related to the neutral transfer coefficients, as shown in Eq. 2.46 to 2.48 (Roehrig et al., 2020).

$$P_{u_{10n}} = g_u\left(\Delta u_{10n}\right) = \sqrt{C_{D_{10n}}}\Delta u_{10n} = u_* \tag{2.46}$$

$$P_{\theta_{10n}} = g_\theta\left(\Delta u_{10n}\right) = \frac{C_{H_{10n}}}{\sqrt{C_{D_{10n}}}}\Delta u_{10n} = \theta_* \frac{\Delta u_{10n}}{\Delta \theta_{10n}} \tag{2.47}$$

$$P_{q_{10n}} = g_q\left(\Delta u_{10n}\right) = \frac{C_{E_{10n}}}{\sqrt{C_{D_{10n}}}}\Delta u_{10n} = q_* \frac{\Delta u_{10n}}{\Delta q_{10n}} \tag{2.48}$$

The intermediate parameters are calibrated using the observations collected during four field campaigns, namely EQUALANT99, FETCH, POMME (Weill et al., 2003) and EGEE (Bourras et al., 2009). In contrast to the establishment of ECUME, the EGEE campaign is incorporated for the calibration of ECUME6. However, the SEMAPHORE and CATCH campaigns are excluded from the calibration process. By using the intermediate parameters, the obtained neutral transfer coefficients slightly differ from these obtained in ECUME, as shown in Figure 2.4a. The polynomial functions used in the functional relationships in ECUME6 are given in Table 2.2. According to Roehrig et al. (2020), the more recent formulations are favored over the older ones because they exhibit reduced measurement spread, resulting in more robust fitted functions, which is shown in Figure 2.4b.

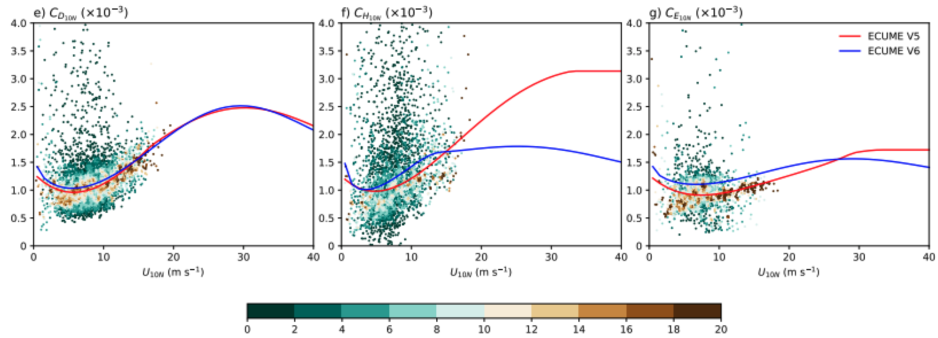

(a) Neutral transfer coefficients of ECUME and ECUME6 as a function of the neutral wind speed

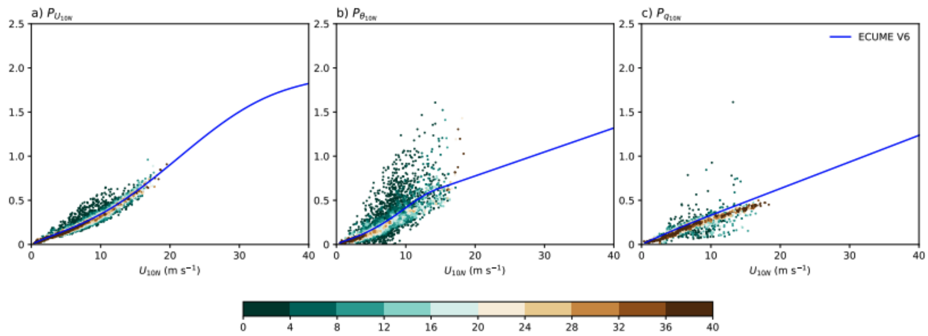

(b) Neutral transfer parameters of ECUME6 as function of the neutral wind speed

Figure 2.4: The colored dots represent the field campaign measurements, with the color scale indicating the density in measurements in the two-dimensional space (in %). Figures obtained from Roehrig et al. (2020)

Table 2.1: Multi-campaigns calibration numerical formulations for the neutral transfer coefficients at 10 m. Obtained from Lebeaupin (2023a)

$C_{D_{10n}} \cdot 1000$	$\Delta u_{10n} \leq 16.8$	$1.3013 - 0.12719\Delta u_{10n} + 0.013067\Delta u_{10n}^2 - 2.2261 \cdot 10^{-4}\Delta u_{10n}^3$
	$16.8 < \Delta u_{10n} \leq 50$	$1.3633 - 0.13056\Delta u_{10n} + 1.6212 \cdot 10^{-2}\Delta u_{10n}^2 - 4.8208 \cdot 10^{-4}\Delta u_{10n}^3 + 4.2684 \cdot 10^{-6}\Delta u_{10n}^4$
	$\Delta u_{10n} > 50$	1.7828
$C_{H_{10n}} \cdot 1000$	$\Delta u_{10n} \leq 33$	$1.2536 - 0.12455\Delta u_{10n} + 0.016038\Delta u_{10n}^2 - 4.3701 \cdot 10^{-3}\Delta u_{10n}^3 + 3.4517 \cdot 10^{-6}\Delta u_{10n}^4 + 3.5763 \cdot 10^{-9}\Delta u_{10n}^5$
	$\Delta u_{10n} > 33$	3.1374
$C_{E_{10n}} \cdot 1000$	$\Delta u_{10n} \leq 29$	$1.2687 - 0.11384\Delta u_{10n} + 1.1467 \cdot 10^{-2}\Delta u_{10n}^2 - 3.9144 \cdot 10^{-4}\Delta u_{10n}^3 + 5.0864 \cdot 10^{-6}\Delta u_{10n}^4$
	$29 < \Delta u_{10n} \leq 33$	$-1.3526 + 1.8229 \cdot 10^{-1}\Delta u_{10n} - 2.6995 \cdot 10^{-3}\Delta u_{10n}^2$
	$\Delta u_{10n} > 33$	1.7232

Table 2.2: Multi-campaigns calibration numerical formulations for the neutral polynomial coefficients at 10 m. Obtained from Lebeaupin (2023b)

$P_{d_{10n}}$	$\Delta u_{10n} \leq 40$	$10^{-3} + 3.66 \cdot 10^{-2}\Delta u_{10n} - 1.92 \cdot 10^{-3}\Delta u_{10n}^2 - 2.32 \cdot 10^{-4}\Delta u_{10n}^3 - 7.02 \cdot 10^{-6}\Delta u_{10n}^4 + 6.4 \cdot 10^{-8}\Delta u_{10n}^5$
	$\Delta u_{10n} > 40$	$0.01868 \cdot (\Delta u_{10n} - 40) + 1.8234$
$P_{h_{10n}}$	$\Delta u_{10n} \leq 14.4$	$5.36 \cdot 10^{-3} + 2.9 \cdot 10^{-2}\Delta u_{10n} - 1.24 \cdot 10^{-3}\Delta u_{10n}^2 - 4.5 \cdot 10^{-4}\Delta u_{10n}^3 - 2.06 \cdot 10^{-5}\Delta u_{10n}^4$
	$\Delta u_{10n} > 14.4$	$0.0271789 \cdot (\Delta u_{10n} - 14.4) + 0.62376$
$P_{e_{10n}}$	$\Delta u_{10n} \leq 10$	$10^{-3} + 3.59 \cdot 10^{-2}\Delta u_{10n} - 2.87 \cdot 10^{-4}\Delta u_{10n}^2$
	$\Delta u_{10n} > 10$	$0.03016 \cdot (\Delta u_{10n} - 10) + 0.3313$

In addition to the newly defined functions, the ECUME6 parameterization incorporates a convergence criterion, whereas the ECUME parameterization uses a fixed number of 10 iterations. The iterative loop in ECUME6 is terminated when the difference between the scale parameters of two consecutive iterations falls below a specified threshold.

The ECUME and ECUME6 parameterizations involve a series of sequential steps for execution. As the primary emphasis of this study is on the ECUME parameterization, which serves as the fundamental basis for ECUME6, the ECUME parameterization will be elaborated upon. Initially, the required variables are initialized, assuming that the 10 m neutral vertical gradients of wind (Δu_{10n}), potential temperature ($\Delta\theta_{10n}$), and humidity (Δq_{10n}) are equal to the vertical gradients. The parameterization proceeds with an iterative procedure. The first step is to obtain the neutral transfer coefficients from the 10 m neutral wind speed using the calibrated functions (Eq. 2.43 to 2.45). The obtained transfer coefficients are then used to calculate the characteristic scales by rearranging Eq. 2.46 to 2.48. The Monin-Obukhov length is computed using Eq. 2.22. The stability parameter is updated based on the calculated Monin-Obukhov length, and subsequently, the neutral vertical gradients (Δu_{10n}, $\Delta\theta_{10n}$, and Δq_{10n}) are updated using the stability functions. This process is described by Eq. 2.49 to 2.51, which result from combining the formulations for the profile relationships (Eq. 2.26 to 2.3.2) with the logarithmic profile relationships, adjusted for a height of 10 m. The stability functions used in ECUME include the stable and unstable profile functions from Kansas (Businger et al., 1971), as well as the free convection forms. However, it is worth noting that the numerical values employed in the unstable functions differ slightly from those used in COARE3.6. The stability functions used in ECUME are presented in Table D.1 in Appendix D. ECUME6 employs the same stability functions as ECUME.

$$\Delta u_{10n} = \Delta u - \frac{u_*}{\kappa}\left[\ln\left(\frac{z}{10}\right) - \psi_m(\zeta)\right] \tag{2.49}$$

$$\Delta\theta_{10n} = \Delta\theta - \frac{\theta_*}{\kappa}\left[\ln\left(\frac{z}{10}\right) - \psi_h(\zeta)\right] \tag{2.50}$$

$$\Delta q_{10n} = \Delta q - \frac{q_*}{\kappa}\left[\ln\left(\frac{z}{10}\right) - \psi_q(\zeta)\right] \tag{2.51}$$

The iteration is performed for a total of 10 times, after which the final values of the characteristic scales and Δu_{10n}, $\Delta\theta_{10n}$, and Δq_{10n} are obtained. These iteratively determined characteristic scales are used to calculate the transfer coefficients (Eq. 2.32 to 2.34), which are subsequently utilized to compute the fluxes (Equations 2.6 to 2.8). Finally, the roughness length z_0 is computed using Eq. 2.52, in which α is the wind-dependent Charnock parameter, defined by Eq 2.38. The parameter β is set to $\beta = 10^{-5}$ (Le Moigne, 2018).

$$z_0 = \alpha\left(\frac{u_*^2}{g}\right) + \beta\left(\frac{C_D}{C_{D_n}}\right) \tag{2.52}$$

The procedure for initializing the required variables, iteratively determining the variables, and calculating the air-sea fluxes is detailed in Appendix C of this study. The accompanying flowchart visually illustrates the sequential steps involved in the ECUME parameterization. It is worth noting that the flowchart does not encompass any potential corrections that might be applied during the process.

3
Data & Methods

To assess the performance of the ECUME and ECUME6 parameterizations, the analysis utilizes the numerical weather prediction (NWP) HARMONIE-AROME model output from cycle 43h22tg3, which incorporates these parameterizations. This analysis is based on comparisons with eddy covariance observations collected during the EUREC4A campaign. Additionally, as eddy covariance observations are prone to flow distortion, a second analysis is performed using the bulk flux observations obtained via the COARE3.6 parameterization. For the analysis, a surface flux diagnostic is developed based on the method proposed by Hsu et al. (2022). This chapter provides details on the data sources utilized and the methodology employed in this study. The analysis involves the processing of both observed data and model results. This includes applying appropriate data processing techniques and methodologies to ensure the accuracy and consistency of the data. Subsequently, a comparison is made between the observed data and the simulated results using the developed surface flux diagnostics. Furthermore, a comparison is made between the simulated results obtained using the COARE3.6, ECUME and ECUME6 methods. Additionally, an offline model is developed for both the COARE3.6 and ECUME methods to evaluate the iteratively obtained coefficients utilized in the computation of the fluxes. This assessment aims to evaluate the effectiveness and reliability of the parameterizations in accurately capturing the turbulent fluxes.

3.1. Data Sources

Each source of data is provided in the NetCDF-4 format. To establish the surface flux diagnostic, both model data and observational data are required. The latent heat flux (LHF) diagnostic requires the surface wind speed ($|U|$) and the vertical gradient of near-surface specific humidity ($\Delta q = q_s - q_a$). The sensible heat flux (SHF) diagnostic requires the surface wind speed ($|U|$) and the vertical gradient of near-surface potential temperature ($\Delta\theta = \theta_s - \theta_a$). Finally, for the momentum flux diagnostic, the momentum flux (τ), the surface wind speed ($|U|$), and the zonal (τ_z) and meridional (τ_y) components of wind stress are considered. To ensure accurate comparisons between model and observational data, the variables must be obtained at the same atmospheric levels. For the wind speed, the atmospheric level is set to 10 m. For the specific humidity and potential temperature, the atmospheric level is set to 2 m. These atmospheric levels are most commonly used in bulk flux parameterizations. In cases where the available EC data lacks the required atmospheric levels, the Monin-Obukhov Similarity Theory (MOST) is utilized to estimate the values of U_{10m}, $q_{a,2m}$, and $\theta_{a,2m}$. In this estimation process, the stability functions used in COARE3.6 are employed.

3.1.1. Observations: EUREC4A Campaign

The present study utilized in-situ observations obtained during the Circulation Coupling in Climate (EUREC4A) campaign through field measurements. The EUREC4A campaign was conducted in January and February 2020 in the winter trades of the North Atlantic near Barbados. The main objective of this campaign was to enhance the understanding of clouds and convection in the trade wind region, which are not yet accurately represented in climate models. The campaign utilized diverse measurement platforms in two operational areas, namely the "Tradewind Alley" and the "Boulevard des Tourbillons." Among the measurement platforms used during the EUREC4A campaign were four research vessels (Stevens et al., 2021). The trajectories of these vessels are illustrated in Figure 3.1. In this study, the field observations obtained from two of these research vessels, namely R/V Ron Brown and R/V Meteor, are utilized. From the observations both the EC fluxes and bulk fluxes are calculated. For the calculation of the bulk fluxes, the COARE3.6 parameterization is employed, being the most commonly used bulk flux parameterizations (C. W. Fairall et al., 2003). A comprehensive explanation of the COARE procedure can be found in Chapter 2.3.3.

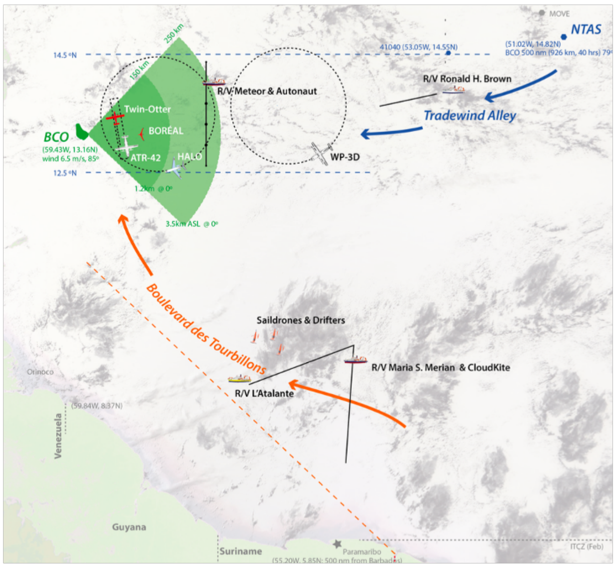

Figure 3.1: Trajectory vessels EUREC4A campaign (Schirmacher, 2021)

R/V Ronald H. Brown

The dataset obtained by R/V Ronald H. Brown (hereafter referred to as R/V Ron Brown) has been quality controlled and is publicly available at National Oceanic and Atmospheric Administration's (NOAA) National Centers for Environmental Information (NCEI) data archive. R/V Ron Brown was part of Atlantic the Tradewind Ocean Atmosphere Mesoscale Interaction Campaign (ATOMIC), the United States' complement to the EUREC4A campaign. The R/V Ron Brown conducted in-situ and remote sensing measurements of oceanic and atmospheric properties from 9 January to 13 February 2020, in the region between 57 and 51°W east of Barbados and between 13 and 16°N. The data has been collected from two sources, namely the NOAA Physical Sciences Lab (PSL) system and the permanently installed instruments on the R/V Ron Brown. In this study, only the PSL data are used, as the ship data are not considered better or always comparable to the PSL data. The available data set includes both direct measurements and model outputs using the COARE3.6 parameterization. COARE3.6 was executed using the water-relative wind, which is essentially the wind adjusted for the ocean's surface flow. Hence, all COARE3.6 outputs specified in the file are relative to water and account for the ocean current (Quinn et al., 2021). The bulk fluxes are typically usable in a -130/+130° window. The direct EC measurements are more prone to flow distortion and measurements outside the -90/+90° window should be excluded. Therefore, quality flags have been established to exclude flux values outside of these windows. The averaging period of the data is 10 minutes.

R/V Meteor

The data The R/V Meteor started its cruise M161 with an installation cruise around Barbados from 13 January to 17 January, then headed eastward to its designated area of operations. The core working area of the cruise was centered around 57°14.7'W and between ∼12°N and ∼14°30'N east of Barbados. The cruise ended on March 2 at the end of the evening in the port of Ponta Delgada (Mohr et al., 2020). Measurements were taken two different heights on the vessel: at the bow, at 10 m height of the vessel, and at the mast, at 34.7 m height of the vessel (Parker Maritime, 2011). The instruments at the top were operational from 15 January to 2 March, while the instruments at the bow were only operating from 15 January until 25 February (Mohr et al., 2020). In this study, only the mast data is used due to the poor accuracy of the bow data caused by disturbances. The available data consists of turbulence data obtained from the EC measurements. The data sets used are the 20 Hz data obtained from the 3D ultrasonic anemometer Metek USA-2 (USAT2), including the analogue input from an open-path gas analyzer LI-7500 (LI-COR) and an acceleration sensor (ADXL327). Additionally, the ship's internal measurement system called DSHIP (SEAPATH) is used for the processing, calculation, and analysis of fluxes. However, this data has a temporal resolution of 10 Hz. As the automatic clock correction was turned off during the campaign, the data has to be time-shifted to obtain consistent time series for USAT2 and SEAPATH.

In comparison to the data collected by the R/V Ron Brown, the data collected by the R/V Meteor has not undergone correction for the motion of the ship. Ship motion affects the wind stress and momentum flux, therefore, motion correction is required after despiking the data. In addition, processing of the EC data requires correction for various factors such as waste incineration, sensor cleaning, rain, sea spray, steady state, and the island effect. To address these corrections, Schirmacher (2021) created masks to flag the data. After masking the data, the determined LHF must be corrected using the Webb, Pearmann and Leuning (WPL) correction and SHF for buoyancy effects to obtain the final corrected fluxes. For the computation of the bulk fluxes, the COARE3.6 bulk flux parameterization is used. To create an accurate bulk flux data set, the motion corrected data along with the masks provided by Schirmacher (2021) are used. In contrast to the EC fluxes, the corrections are applied after the flux calculation.

3.1.2. Model Results

The HARMONIE-AROME (referred to as HARMONIE) numerical weather prediction model is used by The Royal Dutch Meteorological Institute, in Dutch; Koninklijk Nederlands Meteorologisch Instituut (KNMI). The HARMONIE model is one of the atmospheric models used in the ALADIN-HIRLAM NWP system, being a collaborative effort between the ALADIN (Aire Limitée Adaptation dynamique Développement InterNational) and HIRLAM (High Resolution Limited Area Model) consortia (Bengtsson et al., 2017). The model is developed specifically for short-term weather forecasts (KNMI, 2023). In this study, the model results are obtained from the HARMONIE model cycle 43h22tg3, using both ECUME and ECUME6 parameterizations.

The temporal resolution of the data equals 1 hour. The instantaneous variables used from the dataset include: surface pressure (P_s), sea surface temperature (T_s), 2 m air temperature ($T_{a,2m}$), 2 m specific humidity ($q_{a,2m}$), 10 m eastward wind (u_{10m}), 10 m northward wind (v_{10m}). The air-sea fluxes (τ, SHF and LHF) are given as accumulated variables, which are transformed into average fluxes through interpolation (see Chapter 3.3.1). The additional data required includes the specific humidity (q_a), air pressure (P_a) and air temperature (T_a). Only the lowest model level variables are used.

3.2. Eddy Covariance Data Processing

The eddy covariance (EC) method is considered the most direct approach for measuring turbulent fluxes of heat, moisture, and momentum over the ocean's surface. The calculation of these fluxes is defined by the equations given in 2.5. In this study, the used R/V Ron Brown data has already been processed and corrected to remove any errors or inconsistencies. Raw data collected at high frequencies often contain impulse noise, such as spikes, dropouts, constant values, and other types of noise. Conversely, the data collected from the R/V Meteor required further processing, including time shifting and motion correction, to accurately process the raw data.

3.2.1. Time Shifting

To ensure the correct comparison of data for further analysis, a time-shift is necessary for the 20 Hz USAT data and the 10 Hz SEAPATH data. This entails aligning the data sets in time so that corresponding values from each data set are being compared. To determine the correct time-shift, a comparison between the vertical wind velocity (WZ) data of USAT and the heave data of SEAPATH is performed. The USAT data is originally defined using a left-handed coordinate system, where the x-axis points towards the stern, the y-axis towards the portside, and the z-axis upwards. However, for the purpose of further analysis in this study, a NED (North-East-Down), right-handed coordinate system is adopted. Consequently, a transformation from the original left-handed system to the adopted right-handed system is performed on the USAT data. Then, the 20 Hz USAT data is resampled to 10 Hz data by taking the average of two adjacent values. The heave data is transformed to velocity (W_{heave}) by taking the derivative as $(dheave/dt)$, where $dt = 20\ Hz$. From the vertical acceleration data, the vertical velocity (W_{AZ}) is obtained by first subtracting the mean value of AZ, to remove the earth's acceleration included in the value AZ. Finally, the integral is calculated, i.e., the running sum, to obtain W_{AZ}. To determine the maximum correlation between W_{heave} and W_{AZ}, a time-shift is introduced to the ship SEAPATH data, which initially lags behind the USAT data. The time shift is systematically varied with a dt of 10 Hz. The time shifts that correspond to the maximum correlation for each 10-min period are then applied to the 10-min interval SEAPATH data. Initially, the time-shift has a negative value, indicating that the SEAPATH data lags behind the USAT data. At 02/02/2020 13:10, the time-shift becomes positive, indicating that the USAT data lags behind the SEAPATH data.

3.2.2. Spike Removal

Raw data with a temporal resolution of 10 Hz are known to contain physically unreasonable spikes, which can introduce errors and inaccuracies in subsequent analyses. To address this issue, a running mean over a 5-minute interval is calculated for the variables AX, AY, AZ, CC, CH, T_{son}, X, Y, and Z. Any data points that fall below a global minimum or exceed a global maximum value within the averaging interval are detected as spikes and replaced with the running mean value. Similarly, values deviating from the running mean by more than a certain threshold are also identified as spikes and replaced accordingly. The minimum, maximum, and threshold values are set individually for each variable, and are selected based on the standard deviation (σ) over each interval. The thresholds used in this study were obtained from Schirmacher (2021), and were selected. It is important to note that only extreme spikes are removed, as the natural variability of eddies must be preserved. A summary of the minimum, maximum, and threshold values applied in this study is presented in Table 3.1.

Table 3.1: Despiking criteria employed for spike removal of the raw data collected onboard the R/V Meteor

variable	threshold	minimum	maximum
AX	5σ	-9.81 m s^{-2}	9.81 m s^{-2}
AY	5σ	-9.81 m s^{-2}	9.81 m s^{-2}
AZ	5σ	0 m s^{-2}	19.63 m s^{-2}
X	12σ	-20 m s^{-1}	20 m s^{-1}
Y	12σ	-20 m s^{-1}	20 m s^{-1}
Z	8σ	-10 m s^{-1}	10 m s^{-1}
CC	1000σ	8 mmol m^{-3}	32 mmol m^{-3}
CH	1000σ	0 mmol m^{-3}	1200 mmol m^{-3}
T_{son}	8σ	$10°$C	$40°$C

3.2.3. Motion Correction

The use of the EC method to estimate fluxes from a moving platform encounters a significant challenge: a portion of the fluctuating velocity measured is caused by the motion of the platform itself. Therefore, prior to computing the fluxes, it is necessary to eliminate this motion contamination. This contamination originates from three sources: 1) instantaneous tilt of the anemometer due to the pitch, roll and heading variations of the platform; 2) angular velocities at the anemometer resulting from the rotation of the platform about its local coordinate system axes; and 3) translational velocities of the platform in relation to a fixed frame of reference (Edson et al., 1998). Various procedures have been developed to remove the effects of ship motion from the observed relative wind velocity (Pedreros et al., 2003) (Edson et al., 1998) (François Anctil et al., 1994). Following the work of François Anctil et al. (1994), the uncontaminated wind vector can be expressed by the basic equation:

$$\mathbf{V}_c = \mathbf{T}\mathbf{V}_o + \Omega \cdot \mathbf{T}\mathbf{R} + \mathbf{V}_{sh} \tag{3.1}$$

Where $\mathbf{V}_c = (u_c, v_c, w_c)$ is the corrected wind relative to the reference frame (x_b, y_b, z_b), being fixed relative to the surface of the earth. $\mathbf{V}_o = (u_o, v_o, w_o)$ are the wind observations made in the ship coordinate system (x_n, y_n, z_n), which moves with the ship from one instant to the next. $\mathbf{T}$ is the coordinate transformation matrix for a rotation of the ship coordinate system (x_n, y_n, z_n) to the reference system (x_b, y_b, z_b). Ω is the angular velocity vector of the ship coordinate system and $\mathbf{R} = (R_x, R_y, R_z)$ is the position vector of the anemometer with respect to the ship's internal measurement system. The $\mathbf{V}_{sh} = (u_{sh}, v_{sh}, w_{sh})$ refers to the velocity of the ship recorded by the ship's navigation system (Edson et al., 1998). This study uses a right-handed coordinate system, as shown in Figure 3.2, the x-axis points to the bow, the y-axis points to the starboard side, and the z-axis points downwards. The ship's orientation relative to a reference frame is measured by the attitude angles ϕ (roll), θ (pitch), and ψ (yaw), referred to as Euler angles. ϕ is defined positive when the starboard side is down, θ is positive when the bow is up, and ψ is positive in a clockwise direction when viewed from above (Parker Maritime, 2011). Thus, the angles described herein are in accordance with a right-handed convention, given that the rotations are in the clockwise direction when viewed from the positive directions of the respective axes. They can be used directly in the rotational coordinate transformation matrix, which describes the transformation resulting from three distinct rotations of the ship coordinate system about the three when viewed from axes of the reference frame. In guidance, navigation, and control applications, the zyx-convention is commonly used. This convention involves a first rotation of the yaw angle ψ around the z-axis, followed by a rotation of the pitch angle θ around the y-axis, and finally a rotation of the roll angle ϕ around the x-axis. This yields the body-fixed reference system (Thor I. Fossen, 2002). The transformation matrix, used in this study, is defined as follows:

$$\begin{aligned}
&\mathbf{T}(\phi,\theta,\psi)\\
&= A(\psi)A(\theta)A(\phi)\\
&= \begin{bmatrix} \cos(\psi) & -\sin(\psi) & 0 \\ \sin(\psi) & \cos(\psi) & 0 \\ 0 & 0 & 1 \end{bmatrix} \begin{bmatrix} \cos(\theta) & 0 & \sin(\theta) \\ 0 & 1 & 0 \\ -\sin(\theta) & 0 & \cos(\theta) \end{bmatrix} \begin{bmatrix} 1 & 0 & 0 \\ 0 & \cos(\phi) & -\sin(\phi) \\ 0 & \sin(\phi) & \cos(\phi) \end{bmatrix}\\
&= \begin{bmatrix} \cos(\theta)\cos(\psi) & \sin(\theta)\sin(\phi)\cos(\psi)-\cos(\phi)\sin(\psi) & \cos(\phi)\sin(\theta)\cos(\psi)+\sin(\phi)\sin(\psi) \\ \cos(\theta)\sin(\psi) & \sin(\phi)\sin(\theta)\sin(\psi)+\cos(\phi)\cos(\psi) & \cos(\phi)\sin(\theta)\sin(\psi)-\sin(\phi)\cos(\psi) \\ -\sin(\theta) & \sin(\phi)\cos(\theta) & \cos(\phi)\cos(\theta) \end{bmatrix}
\end{aligned} \tag{3.2}$$

The sign of convection in the transformation matrix is based on the right-handed coordinate system using the defined positive directions of the Euler angles.The angular velocity vector (Ω) is defined in the right-hand coordinate system by:

$$\Omega = \begin{bmatrix} -\dot{\theta}\sin(\psi)+\dot{\phi}\cos(\theta)\cos(\psi) \\ \dot{\theta}\cos(\psi)+\dot{\phi}\cos(\theta)\sin(\psi) \\ \dot{\psi}-\dot{\phi}\sin(\theta) \end{bmatrix} \tag{3.3}$$

where over dot represents the time derivative of the Euler angles (Pedreros et al., 2003). The position vector $\mathbf{R} = (-2.61; -2.55; 34.70)$, determined from the locations of the anemometer and the ship's internal measurement system.

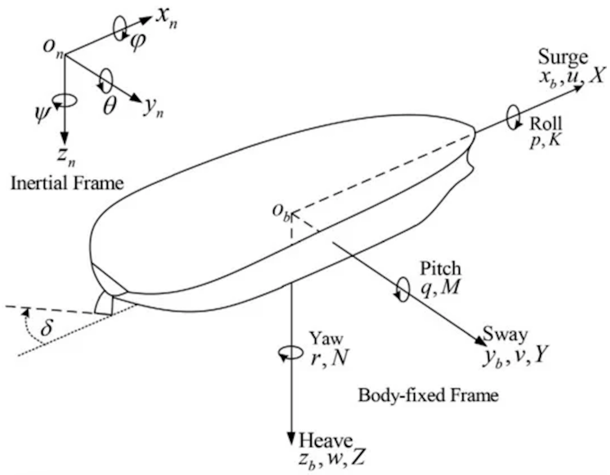

Figure 3.2: NED (North-East-Down), right-handed coordinate system used for ship modeling (Songtao & Peng, 2021)

Euler Angles

During the Meteor operation, the Euler angles have mean values of 0.27°, -0.19°, and 98.40° for roll, pitch, and yaw represented by ϕ, θ, and ψ, respectively. The corresponding standard deviations are 1.12°, 0.80°, and 79.60°. Figures 3.3a to 3.3d show the variation of ϕ, θ, ψ, and heave during the period of 2020-01-27 00:32:00 to 00:50:00. In order to obtain a more comprehensive understanding of the changes in the ship's movements over time, the Euler angles are averaged over 10-minute intervals. The resulting values are then presented in Figures E.1a, E.1b and E.1c in Appendix E.0.1. The yaw angle displays a significant amount of variation over time, whereas roll shows very little variation. The average value of heave is -3.10E-05 with a standard deviation of 0.47, and its 10-minute average is displayed in Figure E.1d in Appendix E.0.1.

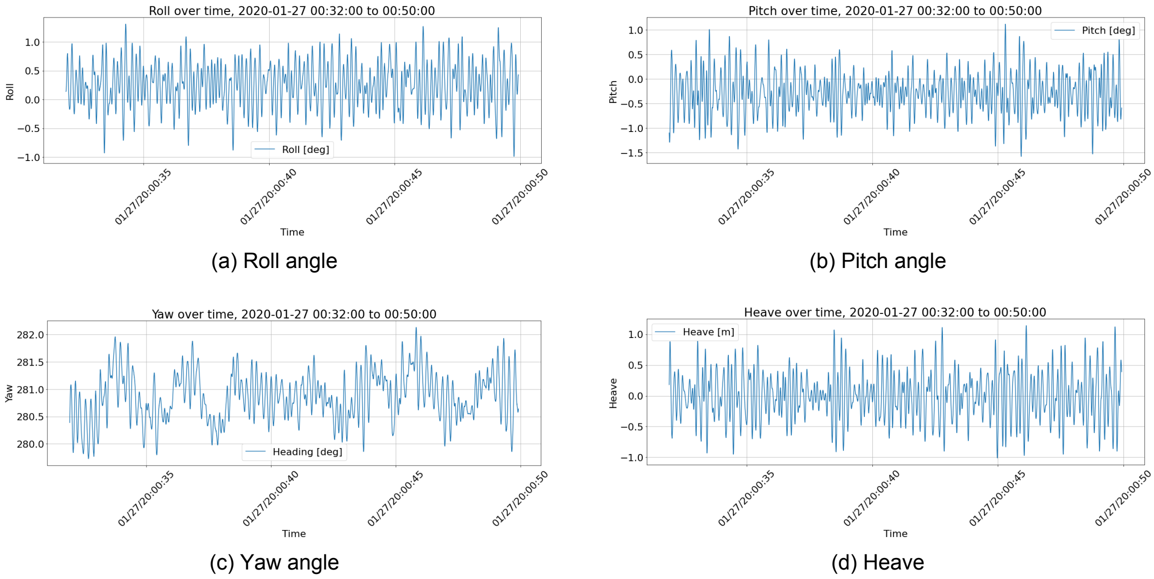

(a) Roll angle (b) Pitch angle

(c) Yaw angle (d) Heave

Figure 3.3: R/V Meteor motions for time period: 2020-01-27 00:32:00 to 00:50:00

3.2.4. Data Masking

The study by Schirmacher (2021) published masks that were specifically generated for the R/V Meteor. These masks can be accessed through the following URL: https://observations.ipsl.fr/thredds/catalog/EUREC4A/SHIPS/RV-METEOR/surface_fluxes/catalog.html. The masks established for the EC measurements account for various factors, including waste incineration (mask_chimney), sensor cleaning (mask_before_cleaning), rain (mask_rain and mask_DWD_rain), data availability (mask_data_availability) and sea spray (mask_sea_spray). The masks indicate a flagging of the corresponding flux for at least one time during the averaging period by NaN. One (1) implies no flagged value.

3.2.5. Webb, Peraman and Leuning Correction

The data from R/V Meteor's 20 Hz SAT2, LI-COR, and ADXL327, as well as the 10 Hz data from DSHIP, are utilized in this study. The LI-COR gas analyzer records concentration of water vapor (CH) in $mmol/m^3$, necessitating a transformation of the latent heat flux (LHF) equation in 2.5 using the molar mass of water vapor, equal to 18.013 g/mol (M_{H2O}).

$$LHF = \mathcal{L}_v \overline{w' \left(CH \cdot M_{\mathrm{H_2O}} \cdot 10^6\right)'} \tag{3.4}$$

The Webb, Pearman, and Leuning (WPL) correction is essential for LHF, as described by E. K. Webb et al. (1980). The correction is necessary due to the dependence of an air parcel's volume and density on changes in temperature and moisture. According to the ideal gas equation, the volume of an air parcel with constant mass increases when either the temperature (T_a) or specific humidity (q_a) rises, under constant pressure. Even minor changes in T_a and q_a can impact the LI-COR observed concentrations, although the mixing ratios remain constant. If the volume of an air parcel expands, the concentration of water vapor (CH) decreases, resulting in a negative flux and a sink in water vapor near the surface, even if the mixing ratio remains unchanged. The correction for density effects due to changes in Ta and gas concentrations for EC fluxes using the LI-COR measurements can be formulated as follows (Schirmacher, 2021):

$$LHF = \mathcal{L}_v \overline{w' \left(CH \cdot M_{\mathrm{H_2O}} \cdot 10^6\right)'} + \left\{ \overline{q_a} \frac{SHF}{c_p \overline{T_a}} \left[1 + 1.61 \frac{c_p \overline{T_a}}{\mathcal{L}_v} \left(1 - 0.61 \overline{q_a}\right) \frac{1}{Bo} \right] \right\} \mathcal{L}_v \tag{3.5}$$

with the Bowen ratio (Bo) being equal to SHF divided by LHF and the specific concentration q_c (Foken, 2017).

3.2.6. Sonic Temperature Correction

To calculate the sensible heat flux (SHF), the temperature measured by the ultrasonic anemometer is utilized. The anemometer measures the speed of sound, which is influenced by the air temperature and to a lesser extent by the water vapor content of the air. However, this measurement is not a direct measure of temperature. Therefore, to obtain the actual temperature from the sonic temperature measured by the anemometer, it is necessary to correct for the effect of humidity using the following formula (Mikrometeorologie et al., 2004):

$$SHF = \rho_a c_{p_a} \left(\overline{w' T_s'} - 0.51 \cdot \overline{T} \cdot \overline{w' q'} \right) \tag{3.6}$$

3.3. Model Data Processing

The processing of model data involves several key steps to ensure accurate and consistent results. One of the primary steps is transforming air-sea fluxes into average values and synchronizing them with other variables through averaging. Additionally, missing variables required for diagnostic purposes are reconstructed, including sea surface saturation specific humidity and surface and 2m potential temperature. Moreover, the output variables obtained from the model are used to reconstruct the intermediate variables that are computed through the parameterization process, including the characteristic length scales and transfer coefficients. Finally, to improve the efficiency of data processing, the temporal domain of the corresponding research vessel is utilized for normalization of the model data.

3.3.1. Model Data Synchronization Across Time Steps

The model data provides output variables as instantaneous values, with a temporal resolution of 1 hour, except for the air-sea fluxes, which are given as accumulated variables. To obtain average fluxes, a transformation is performed using linear interpolation:

$$x = \frac{x_{t+1} - x_t}{\Delta t} \tag{3.7}$$

Where x represents the flux considered. Δt equals 1 hour, the temporal resolution of the model data. However, this calculation produces flux values at interpolated time steps. On the other hand, other variables in the dataset such as P_s and T_s are instantaneous values given at discrete time points. To synchronize all data across time steps, the instantaneous variables are averaged, resulting in variables at the interpolated time step. This ensures that all data are consistent across the entire time range.

3.3.2. Variable Reconstruction from the Model Data

Initially, the missing variables required for the matrix flux diagnostic are acquired. These variables are the sea surface saturation specific humidity (q_s), the surface and 2 m potential temperature (θ_s and θ_{2m}) and the 10 m wind speed ($|U|$). The SURFEX schemes are utilized to compute these variables. To determine q_s, the saturation vapor pressure (e_s) is calculated in SURFEX using the Clausius-Clapeyron equation, which is expressed as (Roland Stull, 1995):

$$e_s \approx e_o \cdot \exp\left[\frac{\mathcal{L}_v}{\mathcal{R}_v} \cdot \left(\frac{1}{T_o} - \frac{1}{T_s} \right) \right] \tag{3.8}$$

Here, e_o denotes the vapor pressure at standard temperature and pressure conditions, $\mathcal{L}v$ represents the latent heat of vaporization, $\mathcal{R}_v$ stands for the gas constant for water vapor, T_s denotes the sea surface temperature, and T_o represents the standard temperature. The constants set in the SURFEX surface scheme are used, namely $e_o = 0.611\ kPa$, $\mathcal{R}_v = 461.525\ J/kg \cdot K$, and $T_o = 273.16\ K$. The latent heat of vaporization is calculated from the sea surface temperature using: $\mathcal{L}_v = 2.5008 \times 10^6 + (4 \cdot R_d - 4.218 \times 10^3) \cdot (T_s - T_o)$, in which $\mathcal{R}_d = 287.0597\ J/kgK$ represents a specific gas constant for dry air. In SURFEX, no cool skin correction is applied to obtain the actual sea surface skin temperature. Finally, q_s is obtained using the following expression:

$$q_s = \frac{\varepsilon \cdot e_s}{P_s + \varepsilon \cdot e_s} \cdot 0.98 \tag{3.9}$$

Where ε represents the ratio of the gas constant for dry air to that for water vapor ($\varepsilon = \mathcal{R}_d/\mathcal{R}_v$), which equals $e_o \approx 0.622\ g/kg$. The expression for q_s incorporates a multiplication factor of 0.98, to account for the reduction of q_s by salinity.

Next, the θ_s and θ_{2m} are calculated using the Exner function given by equation 3.10. $P_0 = 1013.25 \times 10^2$ is the constant reference pressure, $\kappa = \mathcal{R}_d/c_{p_a}$.

$$\theta = T\left(\frac{P_0}{P}\right)^{\kappa} \tag{3.10}$$

Finally, the absolute 10 m wind speed $|U_{10m}|$ (referred to as U_{10m}), is calculated from the 10 m eastward wind (u_{10m}), 10 m northward wind (v_{10m}), as $|U| = \sqrt{u^2 + v^2}$. In addition to computing the necessary variables for matrix flux diagnostics, the output variables generated by the model are utilized to reconstruct the intermediate variables that result from the parameterization process. These intermediate variables are essential for a more comprehensive analysis of the parameterization. First, the computation of the 2 m atmospheric density ($\rho_{a,2m}$) is necessary for subsequent investigation. The geopotential height is calculated from the lowest model level. Then, through interpolation of the pressure between the surface (P_s) and the lowest level (P_a), the 2 m air pressure ($P_{a,2m}$) is obtained. Subsequently, $\rho_{a,2m}$ is computed using the ideal gas law for moist air, as given by equation 3.11. Here, T_v represents the virtual temperature, which is defined by equation 3.12 (J. Marshall & R. Alan Plumb, 1959).

$$\rho_a = \frac{P}{\mathcal{R}_d T_v} \tag{3.11}$$

$$T_v = T_a(1 - q_a + q_a/\varepsilon) \tag{3.12}$$

3.3.3. Normalization of Model Data to Observational Data

The data output of cycle 43h22tg3 is available for the time period between 2020-01-01 and 2020-03-01. To improve data processing efficiency, the temporal domain of the research vessel is used for normalization of the data output. Specifically, for the R/V Ron Brown, the data is transformed to the time period between 2020-01-09 and 2020-02-13, while for the R/V Meteor, the data is transformed to the time period between 2020-01-27 and 2020-02-26. Additionally, the analysis of the data utilizes the spatial domains of the respective research vessels. The latitudinal range for the R/V Ron Brown is from 12.79 to 15.85, and the longitudinal range is from -59.00 to -50.93. For the R/V Meteor, the latitudinal range is from 11.59 to 28.04, and the longitudinal range is from -59.64 to -43.91.

3.4. Surface Flux Diagnostic

The performance of the ECUME and ECUME6 parameterizations is assessed by utilizing the surface flux diagnostic proposed by (Hsu et al., 2022), which is shown in Figure 3.4. As given in equations 2.6 to 2.8, model fluxes are parameterized using transfer coefficients, and based on multiple other input variables. By applying the surface flux diagnostic technique, the relationship between the input variables and flux is visualized, allowing for a separation of the input variables from the transfer coefficients. Consequently, this technique proves to be very valuable in detecting errors that may exist in the transfer coefficients.

The diagnostic method is applied to both observational data and model data, by averaging the fluxes based on established bin widths for each input variable. The bin widths used are $1\ m/s$ for wind speed (U), $1\ g/kg$ for specific humidity (Δq), $1\ N/m^2$ for surface stress (τ), and $1\ K$ for temperature difference ($\Delta\theta$). Subsequently, the observations are subtracted from the model output. The differences in shading are indicative of parameterization differences, while the contour differences indicate discrepancies between the input variables. To detect outliers and enable accurate comparisons, the frequency of occurrence is calculated for each bin in the diagnostic. In Figure 3.4, the white thick contour line represents the probability of occurrence of 1 %.

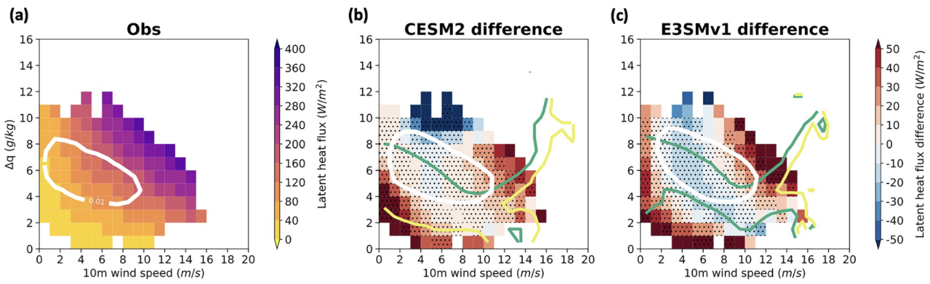

Figure 3.4: Latent heat flux diagnostic developed by (Hsu et al., 2022). Left figure (a) is showing the latent heat flux diagnostic of the observations whereas the other figures (b and c) are showing latent heat flux diagnostic of the observation subtracted from the model output.

The EC and bulk methods are two extensively employed techniques for quantifying the turbulent fluxes of heat, moisture, and momentum over the surface of the ocean. While both methods have their advantages and disadvantages, the accuracy of their results is critical for understanding the exchange of energy between the ocean and atmosphere. Therefore, a comparative analysis between these two methods is necessary to determine which technique produces more accurate results and under what conditions. In order to employ a comprehensive assessment, the ECUME and ECUME parameterization is assessed using both EC observations, as the COARE3.6 bulk parameterization. To ensure the reliability of the direct measurements used for the assessment, a thorough cross-comparison between in-situ measurements is conducted. Furthermore, the reliability of the direct measurements is assessed by comparing them with COARE bulk results. In addition, cross-comparisons between the ECUME and ECUME6 parameterizations are performed to gain further insights into their respective strengths and weaknesses.

This necessitates the determination of EC/bulk flux ratios and the establishment of surface flux diagnostics. Subsequently, the ECUME and ECUME6 results are compared and evaluated using data acquired through both the EC and bulk methods aboard the R/V Meteor and R/V Ron Brown.

3.5. Offline Model for COARE3.6 and ECUME

The ECUME parameterization and the COARE bulk parameterization employ different approaches to estimate momentum, heat, and moisture exchange between the Earth's surface and the atmosphere. In the ECUME parameterization, the drag coefficient is computed based on the 10 meter neutral wind speed value, while the COARE parameterization utilizes the roughness length to determine the drag coefficient. Detailed explanations of the COARE and ECUME procedures can be found in Chapters 2.3.3 and 2.3.4 respectively. Furthermore, visual representations of the sequential steps involved in the ECUME parameterization and the COARE parameterization are provided in the flow charts presented in Appendix C and A. To enable a comparative analysis of the iteratively obtained coefficients using the ECUME and COARE approaches, separate offline models are constructed for each method. The COARE3.6 model used in this study is obtained from the NOAA-PSL COARE-algorithm repository Bariteau, 2023. For the offline ECUME model, the SURFEX-NWP/src/SURFEX/ecume_flux.F90 code, developed by Lebeaupin (2023a), is transformed into a Python-based offline model. The raw dataset collected from the R/V Ron Brown is used as input for COARE3.6, and the HARMONIE cycle 43h22tg3 dataset is used as input for ECUME. By evaluating and comparing the parameters derived, this comparative study seeks to enhance our understanding of the similarities and differences between the two parameterization approaches. Furthermore, the sensitivity of the determined air-sea fluxes to variations in the neutral transfer coefficients and the employed stability functions is examined. Ultimately, the goal is to gain insights into the implications of these approaches for accurately simulating surface-atmosphere interactions.

4
Results

4.1. Comparative Analysis of Eddy-Covariance and COARE3.6 COARE3.6 Methods for Determining Air-Sea Fluxes

In this study, we present a comparative analysis of the EC and COARE3.6 COARE3.6 methods for measuring the latent heat flux (LHF), sensible heat flux (SHF) and momentum flux (tau) using data collected from two research vessels, R/V Ron Brown and R/V Meteor. The analysis includes the calculation of the average ratio of EC fluxes to COARE3.6 fluxes, a comparison of the fluxes obtained through both methods and the evaluation of their accuracy. Furthermore, the flux matrix diagnostics are developed for the SHF and LHF. The findings of this study provide valuable insights into the limitations and applicability of each method for measuring turbulent fluxes over the ocean's surface.

4.1.1. Eddy-Covariance and COARE3.6 Results for R/V Ron Brown

Figures G.1a to G.1c in Appendix G.1 exhibit the Latent Heat Flux (LHF), Sensible Heat Flux (SHF), and momentum flux obtained from COARE3.6 and EC methods at a 10-minute frequency over time. The EC method produces more scattered outcomes compared to the COARE3.6 method for LHF, SHF, and momentum flux. To compare the fluxes obtained by these methods, the average ratio of EC fluxes to COARE3.6 fluxes is calculated for each wind speed bin of 1 m/s. These results are plotted against the 10 m neutral wind speed (Δu_{10n}), which is commonly denoted as u_{10n}, as the wind at the surface equals 0.

Initially, the results without the application of flags are examined, as depicted in Figure 4.1a. For $\Delta u_{10n} > 7.5$ m/s, the EC method yields a higher average LHF than the COARE3.6 method, with an average increase of 6%. The EC SHF shows greater variability, with an average 24% higher than the SHF obtained using COARE3.6. The momentum flux exhibits the highest flux ratio, with an average 32% higher momentum flux for EC results compared to COARE3.6 results. Considering that the COARE3.6 bulk flux parameterization claims a 5% accuracy for wind speeds ranging from 0 to 10 m/s, the substantial differences in SHF and momentum flux between the EC results and COARE3.6 method can be considered significant. However, the measured EC fluxes are contaminated due to motion and flow distortion, necessitating proper corrections (Butterworth & Miller, 2016).

To eliminate anomalies and enhance the accuracy of both COARE3.6 and EC results, flags are applied. Specifically, the COARE3.6 results are limited to a range of -130 to +130 degrees, while the EC results are restricted to a range of -90 to +90 degrees, as recommended in the description of the R/V Ron Brown dataset. The application of flags primarily affects the SHF (from 1.24 to 1.22) and momentum flux (from 1.32 to 1.25) ratios, as evident in Figure 4.1b. Moreover, applying flags results in the exclusion of observations with high wind speeds for both LHF and SHF. However, upon applying the flags, the EC results continue to exhibit substantially higher values for SHF and momentum flux at lower wind speeds. In Figure 4.2, the Monin-Obukhov length (L) is provided as a function of the 10 m wind speed. The negative sign indicates unstable conditions. It is observed that the Monin-Obukhov length is reduced for lower wind speeds. As indicated in Table 4.1, a lower value of L signifies more unstable conditions. Thus, lower winds are associated with more unstable conditions, where it might be challenging for the COARE3.6 method to adequately capture the dynamic fluctuations, leading to higher EC/COARE3.6 flux ratios. For further analysis, the flagged data is examined.

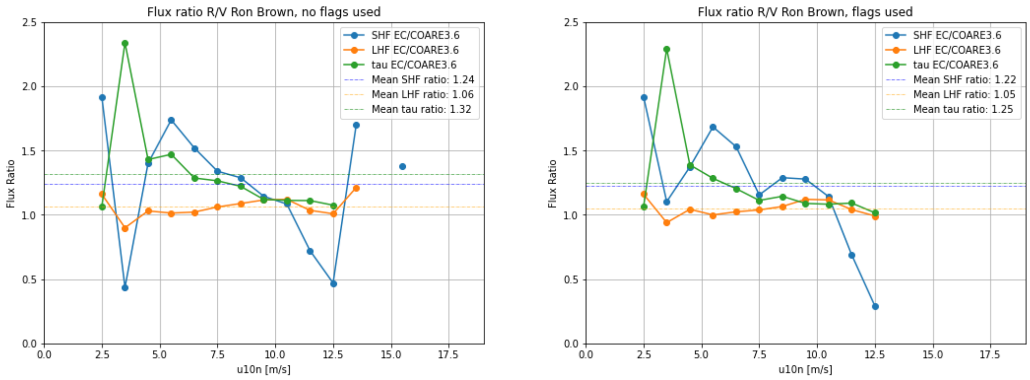

(a) Mean flux ratio R/V Ron Brown, no flags used

(b) Mean flux ratio R/V Ron Brown, flags used

Figure 4.1: Mean SHF and LHF ratio for R/V Ron Brown

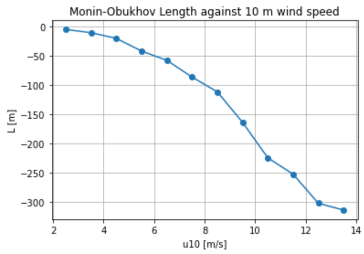

Figure 4.2: Monin-Obukhov Length as a function of the wind speed for R/V Ron Brown

Table 4.1: Stability classification based on Monin-Obukhov length

Stability class	Range of L
Very stable	$0 \leq L < 200$
Stable	$200 \leq L < 1000$
Near neutral	$1000 \leq \|L\|$
Unstable	$-1000 < L \leq -200$
Very unstable	$-200 < L \leq 0$

Latent Heat Flux Diagnostic for R/V Ron Brown

The results obtained for the LHF, the 10 m wind speed (U_{10m}) and the vertical gradient of near-surface specific humidity ($\Delta q = q_s - q_{a,2m}$), from the EC and the COARE3.6 method are illustrated in Figure 4.3a and Figure 4.3b, respectively. Subtracting the diagnostic results highlights the discrepancies in LHF between the two methods, as depicted in Figure 4.4. The results exhibit a fluctuating pattern without a clear trend, which can be attributed to the considerable variability observed in the EC measurements, shown in Figure 4.3a. To further assess the accuracy of the observations, the probability of occurrence of the EC measurements is considered. The gray contour line, representing a 1% probability of occurrence, serves to filter out random fluctuations. Within the contour line, the observed fluctuations are less pronounced compared to areas outside the contour line. Based on the observed trend inside the contour line, it can be inferred that the EC LHF results tend to be higher for elevated wind speeds compared to the COARE3.6 LHF results. This observation aligns with the mean flux ratio of 1.05, illustrated in Figure 4.1b. However, the average difference between the EC and COARE3.6 LHF results is only $4.98\ W/m^2$.

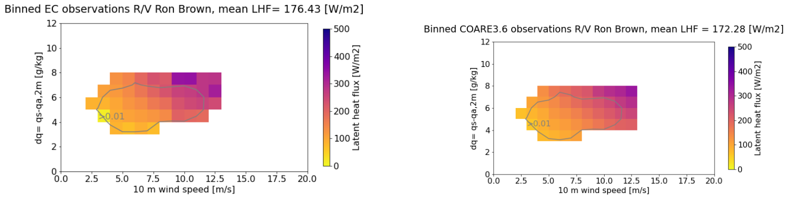

(a) LHF diagnostic EC

(b) LHF diagnostic COARE3.6

Figure 4.3: EC and COARE3.6 LHF diagnostics for R/V Ron Brown

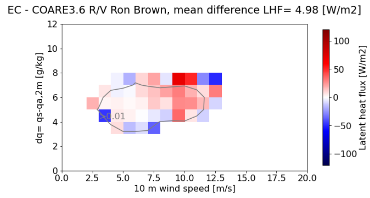

Figure 4.4: LHF diagnostic comparing EC and COARE3.6 results obtained from R/V Ron Brown

Sensible Heat Flux Diagnostic for R/V Ron Brown

Appendix H.1 presents the SHF diagnostics obtained from the EC and COARE3.6 methods. The divergence in SHF values between the two methods is illustrated in Figure 4.5. On average, the EC SHF results exhibit higher values compared to the COARE3.6 results, with a mean difference of $1.12\ W/m^2$. This finding is consistent with the observed flux ratio displayed in Figure 4.1b. Analyzing Figure 4.5, it is evident that for smaller potential temperature gradients, the EC method tends to yield higher SHF values compared to the COARE3.6 method, without any noticeable trend observed for increasing wind speeds. However, for higher potential temperature gradients, the pattern becomes more fluctuating. This suggests that the fluctuations in the SHF flux ratio, as shown in Figure 4.1b, can be attributed to the presence of elevated potential temperature gradients. In situations characterized by intense vertical gradients and turbulent processes, particularly in convective conditions with significant potential temperature gradients, the COARE3.6 method may not adequately capture the intricate dynamics and fluctuations. In contrast, EC measurements directly measure turbulent fluxes and are therefore more responsive to localized variations, potentially providing a more accurate representation of the actual fluxes.

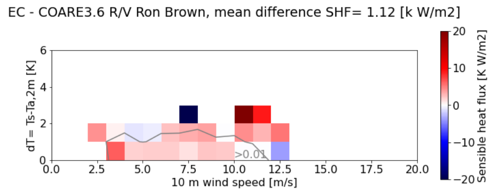

Figure 4.5: SHF diagnostic comparing EC and COARE3.6 results obtained from R/V Ron Brown

4.1.2. Eddy-Covariance and COARE3.6 Results for R/V Meteor

In addition to analyzing the R/V Ron Brown dataset, a comparison is conducted between the EC and COARE3.6 methods using data obtained from the R/V Meteor. Appendix G.2 presents a series of figures (Figures G.2a to G.2c) depicting the time series of LHF, SHF, and momentum flux acquired from both methods with a 30-minute data frequency. These results are obtained following data processing and correction steps, including the application of masks developed by Schirmacher (2021). These masks are specifically designed for 30-minute data. Consequently, the available data points for analysis are significantly reduced compared to the R/V Ron Brown dataset, which has a 10-minute frequency. To evaluate the fluxes obtained from these methods, mean flux ratios, computed after applying the masks, are plotted against the 10 m neutral wind speed (Δu_{10n}) in Figure 4.6b. The COARE3.6 method yields higher LHF than the EC method when $\Delta u_{10n} > 6$ m/s, with an average 27% higher LHF for the COARE3.6

method. This finding is in contrast to the observations from the R/V Ron Brown dataset. Conversely, the EC method exhibits higher SHF values compared to the COARE3.6 method, with an average increase of 90%. This aligns with the results obtained from the R/V Ron Brown dataset. Both SHF flux ratios exhibit significant variability across the 10-meter neutral wind speed range. Notably, the SHF flux ratio is considerably larger for the R/V Meteor dataset compared to the R/V Ron Brown dataset. Similar to the R/V Ron Brown results, lower wind speeds demonstrate a greater SHF flux ratio, indicating more unstable conditions. This is consistent with the reduced Monin-Obukhov Length shown to approach zero with decreasing wind speed, as depicted in Figure 4.7. The EC method also shows higher momentum flux results compared to COARE3.6, with an average flux ratio of 2.17. This significant difference raises concerns about the reliability of the EC momentum flux determination. Despite the application of masks and motion correction, the observed discrepancy suggests potential contamination in the measurements. Uncertainties in estimating momentum flux arise from various factors, including the non-linear relationship between flux and turbulence, the choice of sampling height, and the uncertainty associated with motion correction. Additionally, accurately assessing the influence of distortion effects on turbulent components poses challenges, as current numerical models do not fully account for these effects. These factors have a significant impact on the accuracy of the calculated momentum flux, primarily due to the cross talk between velocity components. Consequently, the momentum flux is particularly vulnerable to motion correction and flow distortion, making it highly susceptible to inaccuracies (Drennan, 2006).

The flux ratios obtained without applying the generated masks are presented in Figure 4.6a. Comparing these results to those obtained with the application of masks, the differences between the COARE3.6 and EC methods are reduced without the masks. This contrasts with the results from the R/V Ron Brown dataset, where the application of flags slightly diminished the differences between the two methods. In Appendix F, the uncertainty associated with the applied masks is examined. By normalizing the data and calculating the standard error for both masked and unmasked datasets, the impact of mask application can be assessed. If the standard error is lower for the masked data compared to the unmasked data, it indicates that the masks have reduced variability and uncertainty in the measurements. For the air-sea fluxes obtained using the EC method, applying masks leads to a reduction in the standard error compared to not using masks. Additionally, for wind speeds exceeding 5 m/s, the fluxes are diminished, while they show a slight increase for lower wind speeds. In the case of COARE3.6 air-sea fluxes, the standard error remains relatively consistent. Overall, the SHF is reduced across the entire range of wind speeds. These findings contribute to the slightly increased disparity between the results obtained with and without mask application.

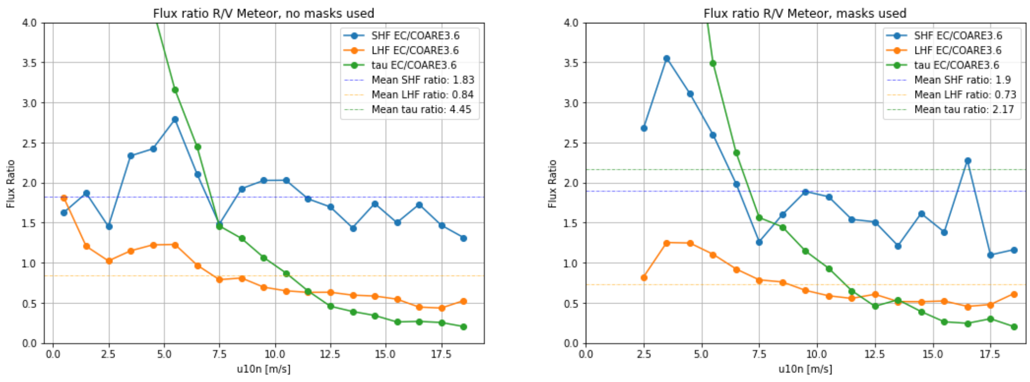

(a) Mean flux ratio R/V Meteor, no masks used

(b) Mean flux ratio R/V Meteor, masks used

Figure 4.6: Mean SHF and LHF ratio for R/V Meteor

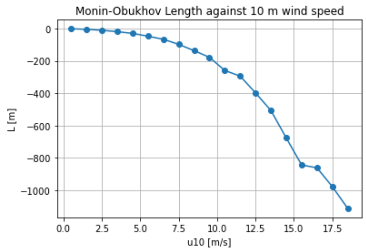

Figure 4.7: Monin-Obukhov Length as a function of the wind speed for R/V Meteor

Latent Heat Flux Diagnostic for R/V Meteor

Figures 4.8a and 4.9 present the diagnostic results for LHF obtained from the EC and COARE3.6 methods. Figure 4.9 highlights the discrepancies in LHF between the two methods. It is observed that wind speeds below $6\ m/s$ are slightly underestimated by the COARE3.6 method, while high wind speeds show a significant overestimation in COARE3.6 LHF compared to EC LHF. These findings align with the conclusions reported by Schirmacher et al. (2021) and the decreasing mean flux ratio across the 10-meter neutral wind speed range as depicted in Figure 4.6b. However, it should be noted that the significant overestimation results lie outside the grey contour line, indicating a probability of occurrence below 1% for the EC observations. Hence, these results are considered inaccurate. Nevertheless, a discernible pattern persists, indicating higher COARE3.6 LHF values for elevated wind speeds compared to EC LHF, with an average disparity of $-69.93\ W/m^2$. This contrasts with the result obtained from R/V Ron Brown, where the average disparity is $4.98\ W/m^2$. The difference in the observed disparities could be attributed to inaccuracies in the EC method, the COARE3.6 method, or a combination of both. As mentioned, the EC results may be contaminated, leading to more fluctuating outcomes as shown in Figures 4.8a and 4.3a. Alternatively, it is possible that the COARE3.6 method fails to adequately capture the complex dynamics and fluctuations.

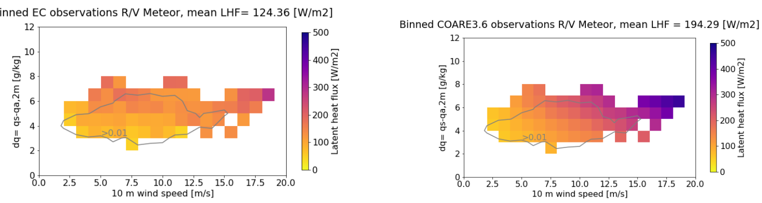

(a) LHF diagnostic EC

(b) LHF diagnostic COARE3.6

Figure 4.8: EC and COARE3.6 LHF diagnostics for R/V Meteor

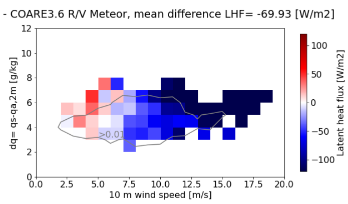

Figure 4.9: LHF diagnostic comparing EC and COARE3.6 results obtained from R/V Meteor

Sensible Heat Flux Diagnostic for R/V Meteor

The discrepancy in SHF values between the EC and COARE3.6 methods is illustrated in Figure 4.10. On average, the EC method yields higher SHF values compared to the COARE3.6 method, with a mean difference of $1.50\ W/m^2$. This observation aligns with the observed flux ratio displayed in Figure 4.6b. When excluding values outside the contour line representing a probability of occurrence above 1%, it can be inferred that the EC method tends to yield higher SHF values compared to the COARE3.6 method. These results pertain to scenarios characterized by small potential temperature gradients. No discernible trend is observed for increased wind speeds. However, as potential temperature gradients increase, the pattern becomes more fluctuating. This indicates that the fluctuations in the SHF flux ratio, as depicted in Figure 4.6b, can be attributed to the presence of elevated potential temperature gradients. These observations are in line with the results obtained from the R/V Ron Brown dataset, indicating that the COARE3.6 method may inadequately capture the complex dynamics and fluctuations in such conditions.

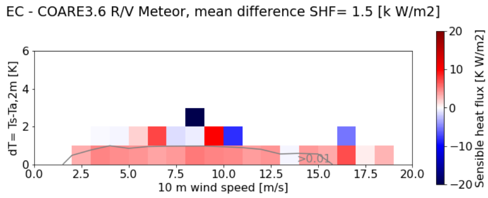

Figure 4.10: SHF diagnostic comparing EC and COARE3.6 results obtained from R/V Meteor

4.2. Comparing and Evaluating the ECUME and ECUME6 Air-Sea Fluxes

The present study compares the diagnostics of the ECUME and ECUME6 parameterizations and subsequently evaluates their performances using direct covariance flux observations obtained from R/V Ron Brown and R/V Meteor. Chapter 4.1 highlights the significant variability observed in the EC results due to measurement challenges. To address this issue, the ECUME and ECUME6 diagnostics are also appraised using the COARE3.6 flux diagnostic, enabling a more comprehensive evaluation.

4.2.1. Latent Heat Flux Diagnostic

ECUME and ECUME6

The initial LHF diagnostic for the ECUME and ECUME6 parameterizations is constructed using the temporal and spatial domain of R/V Ron Brown. Figure 4.11a displays the result for ECUME, while Figure 4.11b shows the result for ECUME6. The contour difference between the two figures indicates that using the ECUME parameterization results in higher values for Δq, whereas the ECUME6 parameterization produces higher values for U_{10m}. Similar results were obtained when constructing the LHF diagnostic using the temporal and spatial domain of the R/V Meteor. This is evident from Figures 4.13a and 4.13b. Comparison of the results obtained using the two domains suggests that during the R/V Meteor campaign, there was a slightly smaller difference in humidity (Δq) and slightly lower magnitudes of the 10 m wind speed (U_{10m}) were observed.

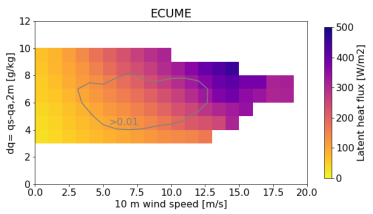

(a) LHF diagnostic ECUME

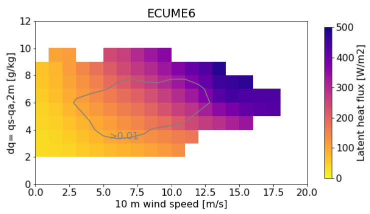

(b) LHF diagnostic ECUME6

Figure 4.11: LHF diagnostics for ECUME and ECUME6 using the R/V Ron Brown domain

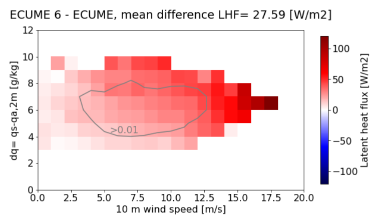

Figure 4.12: LHF diagnostic comparing ECUME and ECUME6 using the R/V Ron Brown domain

By subtracting the LHF diagnostic of ECUME from the ECUME6 diagnostic, discrepancies in LHF resulting from the use of different transfer coefficients in the parameterizations are revealed. Figure 4.12 shows that the most significant differences are observed at extreme values of the 10 m wind speed (U_{10m}) and the near-surface specific humidity vertical gradient (Δq), indicating greater discrepancies in transfer coefficients in these regions. The positive discrepancies in LHF obtained by subtracting the ECUME diagnostic from the ECUME6 diagnostic indicate that the ECUME6 parameterization produces higher values for LHF. Similar results to those obtained in the R/V Ron Brown domain are also observed when analyzing the R/V Meteor domain, as shown in Figure 4.14.

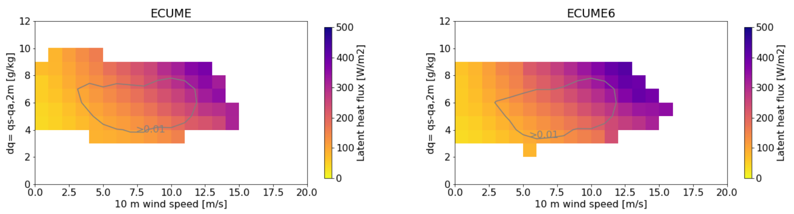

(a) LHF diagnostic ECUME (b) LHF diagnostic ECUME6

Figure 4.13: LHF diagnostics for ECUME and ECUME6 using the R/V Meteor domain

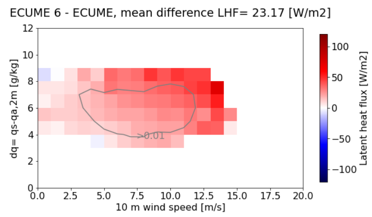

Figure 4.14: LHF diagnostic comparing ECUME and ECUME6 using the R/V Meteor domain

ECUME compared to EC observations

The LHF diagnostic specifically designed for the EC measurements conducted on R/V Ron Brown is subtracted from the ECUME diagnostic, as shown in Figure 4.15a. The figure illustrates that positive discrepancies in LHF are observed at high wind speeds (approximately 12 m/s), while negative LHF discrepancies are observed at lower wind speeds. Consequently, an average LHF discrepancy of only $-0.84\ W/m^2$ is obtained. It is crucial to consider the frequency of occurrence of these results, as higher frequency measurements contribute to the robustness of the findings, while results with lower frequency may not be reliable due to potential measurement inaccuracies or stochastic fluctuations. Notably, the $[3-4\ m/s]$ to $[4-5\ g/kg]$ and the $[6-7\ m/s]$ to $[3-4\ g/kg]$ $U_{10m}-\Delta_q$ bins exhibit anomalous overestimation of LHF compared to the overall pattern displayed in Figure 4.15a. However, the accuracy of these outcomes is debatable, as the probability of occurrence is below 1%.

Figure 4.15b illustrates the discrepancies in LHF between ECUME and EC measurements from R/V Meteor. At lower wind speeds, the ECUME shows and underestimation in LHF compared the the EC LHF results. However, for wind speeds exceeding 6 m/s, ECUME demonstrates an overestimation of LHF compared to the EC results. The most significant overestimations occur outside the contour line, indicating a probability of occurrence below 1%. On average, the overestimation amounts to $54.65\ W/m^2$, which deviates significantly from the average discrepancy obtained from R/V Ron Brown of $-0.84\ W/m^2$. It is noteworthy that the wind speed range covered by R/V Ron Brown is slightly narrower compared to that of R/V Meteor. Specifically, the highest wind speeds recorded for R/V Ron Brown are within the wind speed bin of 13 m/s, while the wind speed range of R/V Meteor extends up to the wind speed bin of 16 m/s. This difference in wind speed coverage between the two datasets may have a significant impact on the average discrepancy calculated. In particular, it is observed in both Figure 4.15a and 4.15b, that higher wind speeds correspond to an overestimation of the LHF calculated ECUME compared to EC results.

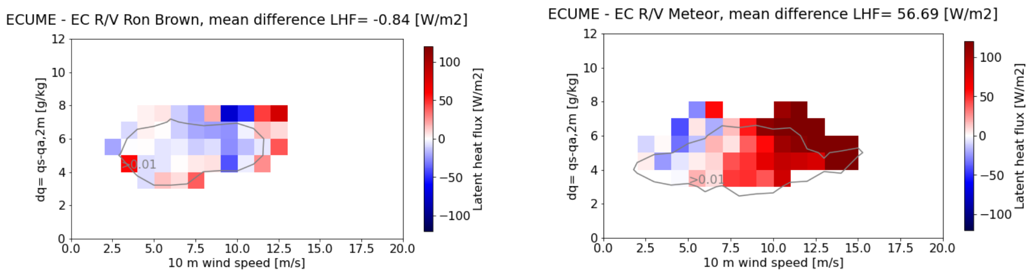

(a) R/V Ron Brown (b) R/V Meteor

Figure 4.15: LHF diagnostic comparing ECUME to EC

ECUME6 compared to EC observations

The LHF diagnostic developed for EC measurements conducted on R/V Ron Brown is subtracted from the ECUME6 diagnostic, and the outcome is depicted in Figure 4.16a. The figure illustrates that the ECUME6 LHF results exhibit overestimation in comparison to the EC LHF results. This overestimation becomes more pronounced at higher wind speeds, resulting in a mean discrepancy of $23.95\ W/m^2$. The observed overestimation trend is consistently supported by only considering observations within the contour line.

Figure 4.16b presents the discrepancies in LHF between the EC LHF measurements conducted on R/V Meteor and the ECUME6 LHF results. The figure reveals that the ECUME6 method produces notably higher LHF values than the EC method when wind speeds exceed 5 m/s. Below 5 m/s, a more variable pattern is observed, indicating both overestimations and underestimations of the LHF. The average difference in LHF amounts to $84.68\ W/m^2$, which is considerably larger than the average difference obtained when comparing the ECUME6 with the EC results from R/V Ron Brown. However, it is important to consider that the difference in wind speed coverage between the R/V Ron Brown and R/V Meteor datasets may significantly influence the calculated average discrepancy.

The observed pattern of increased overestimation of LHF for higher wind speeds is consistent across both the ECUME and ECUME6 comparisons with the EC results. However, for ECUME6, the overestimations in LHF are considerably larger than those observed for ECUME in both the comparisons with EC results from R/V Ron Brown and R/V Meteor.

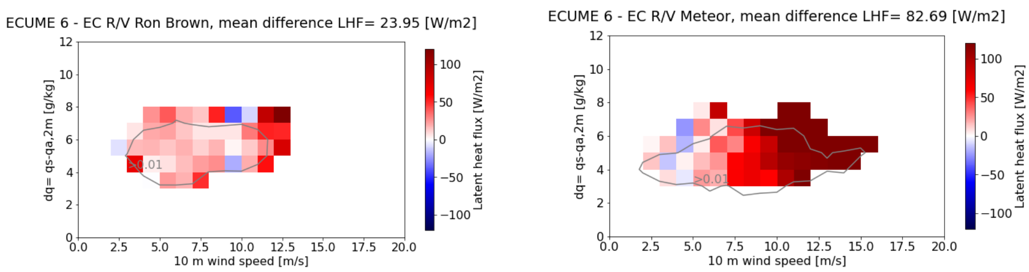

(a) R/V Ron Brown (b) R/V Meteor

Figure 4.16: LHF diagnostic comparing ECUME6 to EC

ECUME compared to COARE3.6

Figure 4.17a illustrates the evaluation of the ECUME diagnostic using the results obtained with the COARE3.6 parameterization for the measurements taken from R/V Ron Brown. The findings reveal slight positive discrepancies in the LHF for high magnitudes of wind speed (U_{10m}) at approximately 11 m/s. This suggests that the ECUME diagnostic overestimates the LHF compared to the COARE3.6 flux parameterization under high wind speed conditions. The observed LHF discrepancies exhibit less dependence on the specific humidity difference (Δq), as no distinct longitudinal pattern is discernible. Below a wind speed of 11 m/s, the LHF values obtained from the ECUME and COARE3.6 methods are very similar, resulting in a mean LHF discrepancy of only $4.54\ W/m^2$.

Figure 4.17b presents the evaluation of the ECUME diagnostic using the COARE3.6 LHF results obtained from the R/V Meteor measurements. A slight overestimation is observed for higher wind speeds, starting at approximately 9 m/s, resulting in an average overestimation of $5.26\ W/m^2$. This observation is consistent with the findings derived from the COARE3.6 results obtained from R/V Ron Brown, which also indicate an overestimation for higher wind speeds. The slightly greater overestimation observed for R/V Meteor compared to the results from R/V Ron Brown is attributed to the difference in wind speed coverage between the two datasets.

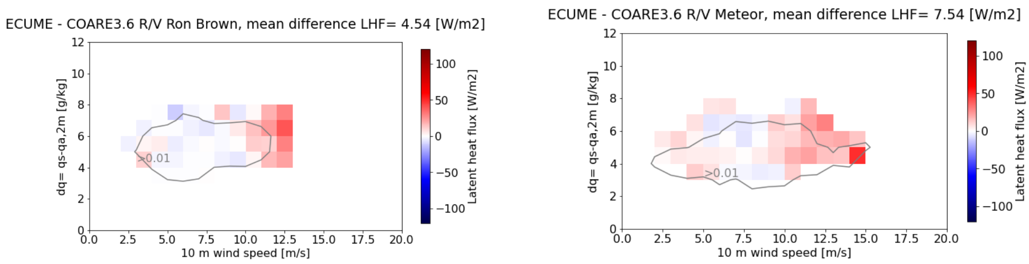

(a) R/V Ron Brown (b) R/V Meteor

Figure 4.17: LHF diagnostic comparing ECUME to COARE3.6

ECUME6 compared to COARE3.6

Figure 4.18a depicts the evaluation of the ECUME6 LHF diagnostic using the COARE3.6 diagnostic derived from measurements taken by R/V Ron Brown. The analysis reveals an overall overestimation of LHF by ECUME6 compared to COARE3.6 LHF. Furthermore, a distinct pattern emerges, indicating an increase in LHF overestimation as wind speed rises. On average, the discrepancy in LHF amounts to $29.59\ W/m^2$. This average closely aligns with the average overestimation in LHF observed when comparing with the EC LHF of R/V Ron Brown, as depicted in Figure 4.16a.

Figure 4.18b illustrates the assessment of the ECUME6 LHF diagnostic using the COARE3.6 LHF derived from measurements conducted by R.V. Meteor. The results indicate an overestimation of LHF by the ECUME6 diagnostic, with the magnitude of overestimation becoming more pronounced at higher wind speeds. On average, the difference in LHF amounts to $29.00\ W/m^2$, which is consistent with the findings obtained from the comparison with the COARE3.6 R/V Ron Brown LHF.

In the evaluations of ECUME and ECUME6 LHF against the COARE3.6 LHF results, a consistent pattern emerges, revealing a positive correlation between overestimation and wind speed. This trend is also evident when comparing ECUME and ECUME6 with the EC results. However, ECUME6 demonstrates larger overestimations compared to ECUME, exhibiting overestimation across the entire range of wind speeds and humidity gradients in the assessment with the COARE3.6 results. In contrast, ECUME shows no overestimations and even underestimations for lower wind speeds.

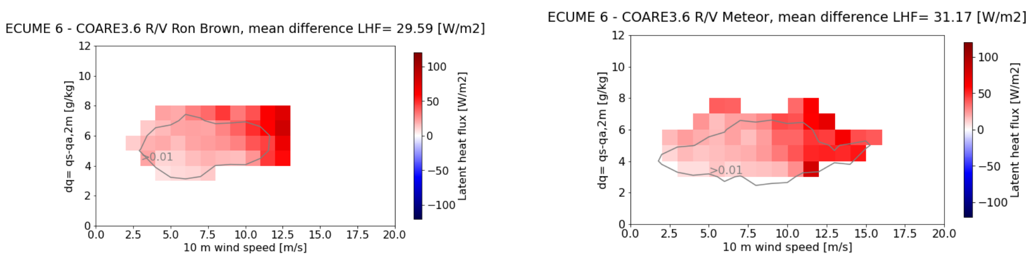

(a) R/V Ron Brown (b) R/V Meteor

Figure 4.18: LHF diagnostic comparing ECUME6 to COARE3.6

4.2.2. Sensible Heat Flux Diagnostic

ECUME and ECUME6

The initial SHF diagnostic for the ECUME and ECUME6 parameterizations is derived using the temporal and spatial data from R/V Ron Brown. The results are presented in Appendix H.1. Figure 4.19 demonstrates that notable differences are observed at higher values of the 10-meter wind speed (U_{10m}) and a significant potential temperature gradient ($\Delta\theta$), indicating larger variations in the transfer coefficients within these regions. The positive differences in SHF, obtained by subtracting the ECUME diagnostic from the ECUME6 diagnostic, suggest that the ECUME6 parameterization produces higher SHF values. However, substantial positive differences are only evident for potential temperature gradients greater than 2 K and wind speeds above 7 m/s, resulting in an average difference of $3.22\ KW/m^2$. For the SHF diagnostic using the temporal and spatial data from R/V Meteor, a similar pattern is observed, as depicted in Figure 4.20. However, the average difference amounts to $-0.73\ KW/m^2$. The disparity in wind speed coverage and potential temperature gradient coverage between the two datasets may impact the calculated average discrepancy. Notably, greater overestimations of SHF for ECUME6 compared to ECUME are observed at high wind speeds and significant potential temperature gradients, which are less covered by the range of R/V Meteor measurements, as shown by comparing the Figures H.3 to H.4 in Appendix H.1.

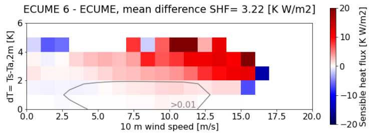

Figure 4.19: SHF diagnostic comparing ECUME and ECUME6 using the R/V Ron Brown domain

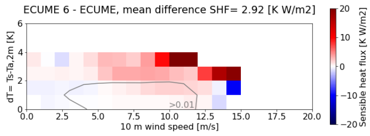

Figure 4.20: SHF diagnostic comparing ECUME and ECUME6 using the R/V Meteor domain

ECUME compared to EC observations

The SHF diagnostic obtained from EC measurements conducted on R/V Ron Brown is subtracted from the ECUME SHF diagnostic, as shown in Figure 4.21a. The figure illustrates a fluctuating pattern, with the exclusion of extreme outliers when considering results within the 1% probability of occurrence contour line. This pattern indicates an overestimation of SHF at higher wind speeds (approximately above 9 m/s) within the contour line. The average discrepancy in SHF amounts to $1.44\ KW/m^2$. Outside the contour line, more fluctuating results are observed, possibly due to elevated temperature gradients leading to unstable conditions that may not be accurately captured by the ECUME parameterization. This behavior is also evident in the comparison of SHF diagnostic results between EC and COARE3.6, as shown in Figure 4.5.

The ECUME diagnostic is compared to the SHF diagnostic obtained from the EC measurements conducted on R/V Meteor, as depicted in Figure 4.21b. The figure reveals a fluctuating pattern with a tendency to overestimate SHF at higher wind speeds and underestimate SHF at lower wind speeds, similar to the findings from the comparison with R/V Ron Brown. The average discrepancy in SHF is slightly lower compared to R/V Ron Brown, with a value of $0.91\ KW/m^2$. This may be attributed to the difference in wind speed coverage and potential temperature gradient coverage between the two datasets.

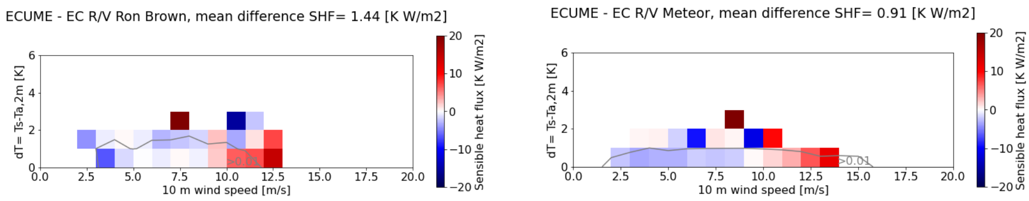

(a) R/V Ron Brown (b) R/V Meteor

Figure 4.21: SHF diagnostic comparing ECUME to EC

ECUME6 compared to EC observations
Figure 4.22a illustrates the comparison between the SHF obtained with ECUME6 and the SHF obtained with EC from measurements taken by R/V Ron Brown. The figure shows that at high wind speeds (approximately 9 m/s), the SHF calculated by ECUME6 is overestimated, while it is underestimated for lower wind speeds. The average discrepancy in SHF amounts to $2.32\ KW/m^2$.

A similar pattern is observed when comparing the SHF results of ECUME6 with the SHF results of EC obtained from measurements taken by R/V Meteor, as shown in Figure 4.22b. The average discrepancy in SHF is slightly lower compared to R/V Ron Brown, with a value of $1.37\ KW/m^2$, which may be attributed to differences in wind speed and potential temperature coverage.

The observed pattern of increased overestimation of SHF for higher wind speeds and underestimation for lower wind speeds is consistent in both the comparisons of ECUME and ECUME6 with the EC results. However, for ECUME6, the overestimations in SHF are slightly larger than those observed for ECUME in both comparisons with the EC results from R/V Ron Brown and R/V Meteor. Furthermore, Figures 4.19 and 4.20 indicate that the discrepancy between the SHF results obtained from ECUME and ECUME6 increases with higher wind speeds and larger potential temperature gradients. However, it should be noted that the limited coverage of potential temperature in the R/V Ron Brown and R/V Meteor datasets prevents a comprehensive assessment of the ECUME and ECUME6 results for larger temperature gradients.

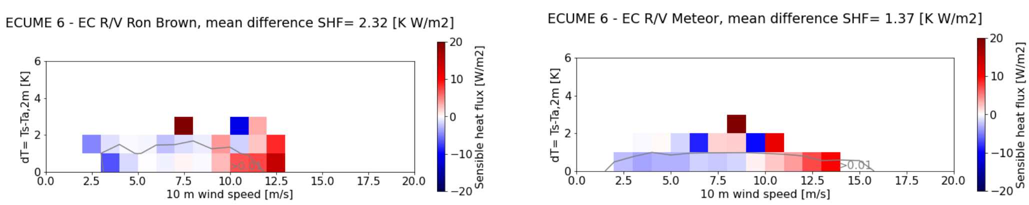

(a) R/V Ron Brown (b) R/V Meteor

Figure 4.22: SHF diagnostic comparing ECUME6 to EC

ECUME compared to COARE3.6
Upon comparing the SHF results obtained from ECUME to the COARE3.6 results derived from measurements taken on R/V Ron Brown, as depicted in Figure 4.17b, a clear pattern emerges. This pattern reveals that ECUME tends to overestimate the SHF in comparison to the COARE3.6 results, particularly as wind speed increases. The average discrepancy in SHF equals $2.09\ KW/m^2$.

A consistent pattern is observed when comparing the ECUME SHF results with the COARE3.6 SHF obtained from measurements taken on R/V Meteor, as depicted in Figure 4.17b. The comparison reveals that ECUME tends to overestimate the SHF in comparison to the COARE3.6 results, particularly at higher wind speeds and lower potential temperature gradients. Additionally, for potential temperature gradients above 1 K, a slight underestimation in SHF can be observed. However, it is worth noting that these observations fall outside the contour line, indicating less accuracy. On average, there is a difference of $2.25\ KW/m^2$ in SHF between the two datasets.

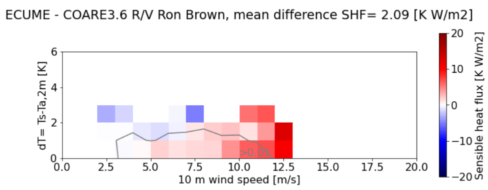

(a) R/V Ron Brown

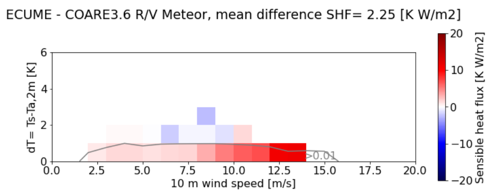

(b) R/V Meteor

Figure 4.23: SHF diagnostic comparing ECUME to COARE3.6

ECUME6 compared to COARE3.6

Figure 4.24a presents the assessment of the ECUME6 SHF diagnostic using the COARE3.6 diagnostic obtained from measurements taken on R/V Ron Brown. The figure demonstrates that ECUME6 tends to overestimate the SHF, particularly at wind speeds above 5 m/s. Furthermore, the degree of overestimation increases as the wind speed increases. On average, the observed overestimation in SHF is slightly higher for the ECUME6 comparison compared to ECUME, with an average value of $2.98\ KW/m^2$.

When comparing the ECUME6 SHF with the R/V Meteor COARE3.6 SHF, as shown in Figure 4.24a, predominantly overestimations are observed, particularly at higher wind speeds. This pattern is consistent with the observations made in the comparison with R/V Ron Brown. The average overestimation amounts to $2.71\ KW/m^2$, which is slightly higher than the overestimation obtained using ECUME.

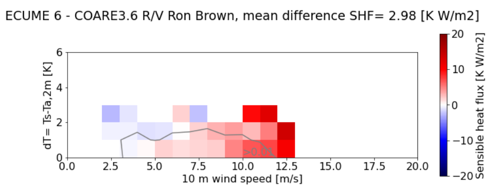

(a) R/V Ron Brown

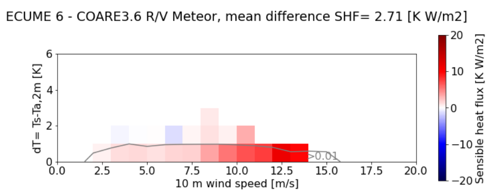

(b) R/V Meteor

Figure 4.24: SHF diagnostic comparing ECUME6 to COARE3.6

A comparable pattern emerges when comparing the SHF results obtained from ECUME6 to those obtained from EC and COARE3.6 measurements conducted on R/V Ron Brown and R/V Meteor. This similarity in the results can be attributed to the restricted observational domain provided by the dataset, which primarily covers a narrow range of potential temperature gradients. For both ECUME and ECUME6, an overestimation of SHF is observed for high wind speeds and low potential temperature gradients, while an underestimation is observed for lower wind speeds.

4.2.3. Momentum Flux

The momentum flux diagnostics, including the zonal (τ_x) and meridional (τ_y) components, are presented in Appendix I. The zonal component represents east-west flow, while the meridional component represents north-south flow (Milrad, 2018). To facilitate a more interpretable evaluation, the zonal and meridional components of the momentum flux are calculated for each wind speed interval of 1 m/s, instead of utilizing the momentum flux diagnostics.

First, a comparison is conducted between the EC results obtained from measurements on R/V Ron Brown and the corresponding components of momentum flux from ECUME and ECUME6. Figure 4.25a illustrates that the meridional component of momentum flux is similar for both ECUME and ECUME6, but lower for the EC observations. This suggests an overestimation of the meridional component in ECUME and ECUME6 compared to the EC results. Conversely, the zonal component is underestimated in both ECUME and ECUME6 when compared to the zonal component of momentum flux from EC. Additionally, the Figure reveals a sudden decrease in both the zonal and meridional components of the EC momentum flux for wind speeds exceeding 12 m/s, possibly attributable to convective gustiness. Barbados is situated in a region influenced by the prevailing North Atlantic Trade Winds, which typically blow from the northeast direction (Tout et al., 1968). However, during strong southerly gustiness events, rapid changes in wind direction and intensity can occur, leading to disruptions in the momentum flux components. The ECUME and ECUME6 parameterizations may struggle to accurately capture these complex and dynamic events. Figure 4.25b presents the total momentum flux results for ECUME, ECUME6, COARE3.6 and EC plotted against the 10 meter wind speed. The EC method exhibits the highest momentum flux, followed by the COARE3.6 method. Notably, ECUME demonstrates the greatest underestimation of momentum flux, with the discrepancy increasing at higher wind speeds. This underestimation in the zonal momentum flux and overestimation in the meridional momentum flux for both ECUME and ECUME6 result in a total momentum flux comparable to the total momentum flux obtained with the EC method.

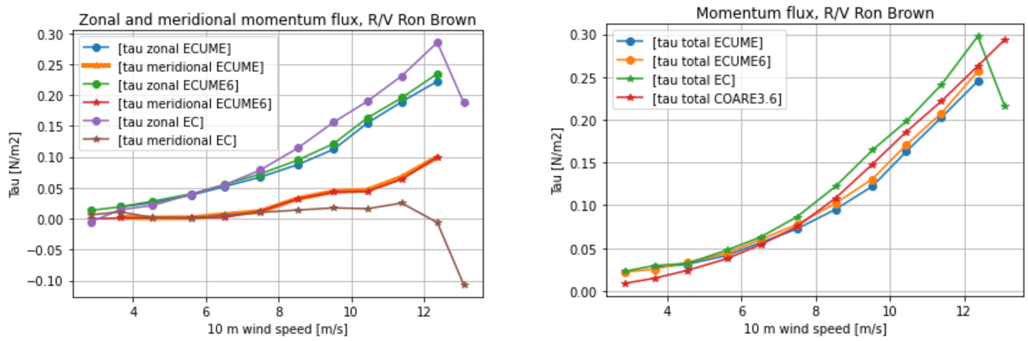

(a) Tau zonal and meridian components

(b) Tau total

Figure 4.25: Momentum flux against 10 m wind speed for R/V Ron Brown

Secondly, a comparison is made between the components of momentum flux from ECUME and ECUME6 with the EC results obtained from measurements conducted on R/V Meteor. The meridional and zonal components of the momentum flux are shown in Figure 4.26a. As mentioned previously in Chapter 4.1.2, the momentum flux derived from R/V Meteor appears to be unreliable due to significant random fluctuations. Typically, the momentum flux components are expected to increase with increasing wind speed (Lykossov, 2009). However, the observed patterns in the meridional and zonal wind components seem to be unreliable, potentially indicating significant contamination during the measurements. Despite the observed fluctuations and potential unreliability of the momentum flux derived from R/V Meteor, it is important to note that the EC results obtained from R/V Meteor are still considered for further analysis. While caution is exercised due to the significant random fluctuations, these measurements provide valuable data that contribute to a comprehensive understanding of the momentum flux dynamics in the study area. Figure 4.26b illustrates the total momentum flux results for ECUME, ECUME6, COARE3.6, and EC plotted against the 10 m wind speed. At higher wind speeds, above approximately 7 m/s, both ECUME and ECUME6 exhibit a slight overestimation in momentum flux compared to COARE3.6. The EC method, on the other hand, shows the highest momentum flux values up to a wind speed of 10 m/s.

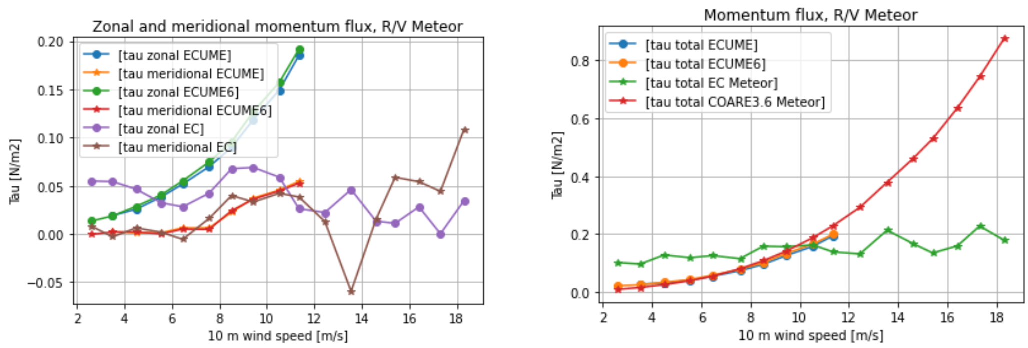

(a) Tau zonal and meridian components

(b) Tau total

Figure 4.26: Momentum flux against 10 m wind speed for R/V Meteor

4.3. Results Offline Model: ECUME Parameterization vs. COARE3.6 Parameterization

The results of the comparative analysis between the ECUME parameterization and the COARE3.6 parameterization for estimating momentum, heat, and moisture exchange are presented in this section. Based on the findings presented in Chapter 4.2, the ECUME parameterization is chosen over the ECUME6 parameterization. It is determined that the ECUME parameterization demonstrates a comparatively lower level of overestimation in comparison to the overestimation observed with the ECUME6 parameterization. This conclusion remains consistent when comparing ECUME and ECUME6 with COARE3.6 and EC fluxes. The offline ECUME and COARE3.6 models developed for each method are employed to assess and compare the coefficients obtained from the iterations of both methodologies. The COARE3.6 model, utilized in this study, is sourced from the NOAA-PSL COARE-algorithm repository Bariteau, 2023. To create the offline ECUME model, the SURFEX-NWP/src/SURFEX/ecume_flux.F90 code, developed by Lebeaupin (2023a), is converted into a Python-based offline model.

The raw dataset obtained from the R/V Ron Brown served as input for COARE3.6, while the HARMONIE cycle 43h22tg3 dataset is employed as input for ECUME. The primary focus of this study revolves around the neutral transfer coefficients, which are essential in accurately estimating the exchange of momentum, heat, and moisture between the Earth's surface and the atmosphere. Notably, the ECUME parameterization computes the neutral transfer coefficients based on the 10 meter neutral wind speed value, while the COARE parameterization employs the roughness length to estimate these coefficients. Following the comparison of the neutral transfer coefficients, the transfer coefficients themselves are assessed. Lastly, the resulting air-sea fluxes, calculated using the transfer coefficients, are compared.

4.3.1. Comparative Analysis of Neutral Transfer Coefficients

In the ECUME parameterization, the initial step of the iteration process involves determining the neutral transfer coefficients based on the 10 m neutral wind speeds (Δu_{10n}), which are initially assumed to be equal to the reference wind speed (u_z). After performing the iteration process for 10 times, the final values of the neutral transfer coefficients are obtained. A comprehensive explanation of the ECUME procedure can be found in Chapter 2.3.4. In contrast, the COARE3.6 bulk parameterization determines the neutral transfer coefficients as the final step, outside the iteration process, using the iterated roughness length. A detailed explanation of the COARE procedure can be found in Chapter 2.3.3.

The obtained final results for the neutral transfer coefficients from ECUME (denoted as _E_m, where m refers to the established model) and COARE3.6 (denoted as _C) are compared in Figures 4.27a to 4.27c, against the 10 m neutral wind speed. For the neutral drag coefficient (C_{D10n}) comparison shown in Figure 4.27a, the ECUME parameterization (represented by the orange line) yields higher values for wind speeds up to approximately 6.5 m/s. However, for higher wind speeds, the COARE3.6 parameterization (represented by the blue line) produces larger values. Regarding the neutral temperature transfer coefficient (C_{H10n}) comparison shown in Figure 4.27b, the results are similar for COARE3.6 and ECUME at a wind speed of 5 m/s. However, for higher wind speeds, the ECUME parameterization results in significantly higher values for the neutral temperature transfer coefficient. The difference in C_{H10n} between COARE3.6 and ECUME increases with an increase in Δu_{10n}. The comparison of the neutral moist transfer coefficient (C_{E10n}) shown in Figure 4.27c indicates that using the COARE3.6 parameterization results in considerably higher values compared to those obtained using the ECUME parameterization. The obtained values for C_{H10n} and C_{E10n} using COARE3.6 are found to be the same. In COARE3.6 it is assumed that the moist roughness length equals the heat roughness length ($z_{0_q} = z_{0_t}$), which is a commonly used assumption in parameterizations (Stull, 1988).

In order to corroborate the obtained results for the neutral transfer coefficients from ECUME, a comparison is made with Figure 2.4a in Chapter 2.3.4. The observed shape and values closely align with those depicted in the Figure obtained from Roehrig et al. (2020), providing confirmation of the obtained results.

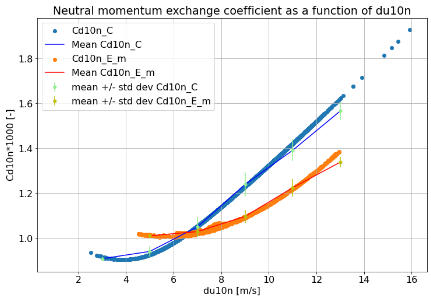

(a) Neutral drag coefficient

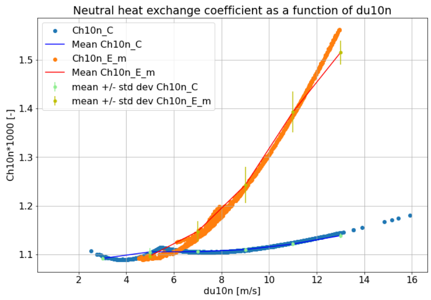

(b) neutral temperature transfer coefficient

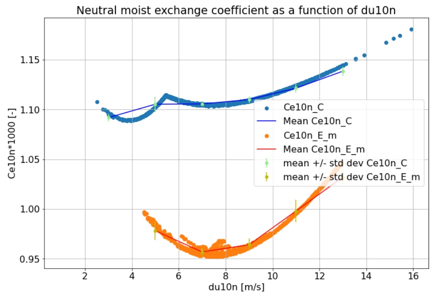

(c) neutral moist transfer coefficient

Figure 4.27: Comparing the neutral transfer coefficients determined using COARE3.6 and ECUME

4.3.2. Comparative Analysis of Transfer Coefficients

Drag Coefficient

Upon completion of the iterative procedure in ECUME, the transfer coefficients are derived based on the iteratively determined characteristic scales. The same procedure is also followed in COARE3.6. The obtained values of the transfer coefficients obtained from ECUME and COARE3.6 are compared in Figures 4.28a to 4.28c, against the 10 m wind speed. It can be observed that the drag coefficient (C_D) obtained from ECUME is overestimated for wind speeds up to about 9 m/s, after which similar results are obtained. Both ECUME and COARE3.6 exhibit an increasing trend in the drag coefficient with increasing wind speed. This trend indicates that higher wind speeds result in stronger drag forces, leading to increased momentum exchange between the atmosphere and the surface. As C_D varies with stability relative to its neutral value C_{D10n}, a similar trend is observed as in Figure 4.27a. However, the presence of unstable atmospheric conditions leads to elevated turbulence and enhanced drag forces, resulting in higher values of C_D compared to C_{D10n}.

Temperature Transfer Coefficient

For the temperature transfer coefficient (C_H) (Figure 4.28b), ECUME underestimates the coefficient for wind speeds up to about 7 m/s, and then overestimates it for higher wind speeds compared to the C_H obtained using COARE3.6. In ECUME, C_H increases with increasing wind speed, while COARE3.6 shows a decrease. The observed behavior in the COARE3.6 results aligns with the patterns depicted in Figure 2.2 of Chapter 2.3 (Wallace & Hobbs, 2006), indicating that for lower wind speeds associated with more unstable conditions, an increase in C_H is expected, while a decrease is anticipated for higher wind speeds. The variation of C_H with wind speed in COARE3.6 exhibits a similar trend and comparable values to the C_{H10n} values obtained in Figure 4.27b. However, it is evident that the inclusion of stability effects leads to an elevation of C_H compared to C_{H10n} for lower wind speeds, which correspond to more unstable conditions.

In contrast, ECUME shows a decrease C_H under unstable conditions, which aligns with the pattern observed for C_{H10n} shown in Figure 4.27b. The observed elevation of C_H compared to C_{H10n} for low wind speeds, attributed to stability effects, aligns with the phenomenon observed in COARE3.6.

Moist Transfer Coefficient

Regarding the moist transfer coefficient (C_E) (Figure 4.28c), the ECUME parameterization consistently underestimates the coefficient, with a slight reduction in underestimation for higher wind speeds. The observed trend for ECUME and COARE3.6 is similar, with an decrease in C_E as wind speed increases. This behavior aligns with the patterns depicted in Figure 2.2 of Chapter 2.3 (Wallace & Hobbs, 2006), indicating that for lower wind speeds associated with more unstable conditions, an increase in C_E is expected, while a decrease is anticipated for higher wind speeds.

The values of C_E obtained using COARE3.6 are nearly identical to the values of C_H obtained using COARE3.6. This similarity is expected because in COARE3.6 the same roughness lengths ($z_{0_q} = z_{0_t}$) and stability functions ($\psi_h = \psi_q$) are used for temperature and moist. The results of C_E for ECUME exhibit a similar trend and comparable values to the C_{E10n} values obtained in Figure 4.27c. However, the C_{E10n} values obtained for ECUME are significantly smaller compared to C_{E10n} obtained using COARE3.6. As a result, the ECUME parameterization consistently underestimates C_E when compared to the values obtained from COARE3.6.

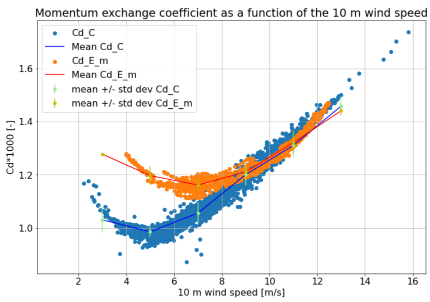

(a) Drag transfer coefficient

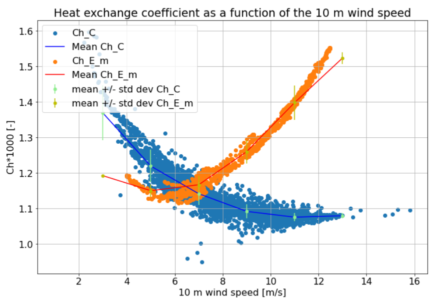

(b) Temperature transfer coefficient

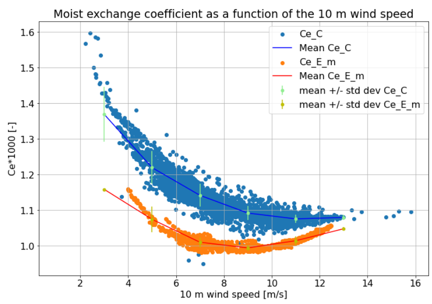

(c) Moist transfer coefficient

Figure 4.28: Comparing the transfer coefficients determined using COARE3.6 and ECUME against 10 m wind speed

4.3.3. Comparative Analysis of Air-Sea Fluxes

Using the transfer coefficients, the air-sea fluxes are determined. The results of air-sea fluxes for COARE3.6 and ECUME are compared in Figures 4.29a to 4.29c. The Figures show similar patterns as the above (Chapter 4.3.2) performed comparison using transfer coefficients. The ECUME momentum flux is first overestimated compared to the COARE3.6 determined momentum flux, up to a wind speed of 8 m/s. Thereafter, the momentum flux is slightly underestimated. The results obtained using the established ECUME and COARE3.6 models exhibit strong agreement with the findings presented in Figure 4.25b of Chapter 4.2.3.

For the SHF, shown in Figure 4.29b, first a slight underestimation for ECUME is shown, which turns into an overestimation around a wind speed of 8 m/s. This finding aligns with the observed temperature transfer coefficients (C_H), given in Figure 4.28b. However, it is important to note that this observed pattern is also influenced by the potential temperature gradient. Specifically, for higher potential temperature gradients, ECUME tends to underestimate the SHF compared to the results obtained by COARE3.6. On the other hand, for lower potential gradients, ECUME shows overestimations. When comparing the pattern displayed in Figure 4.29b to the results obtained in Figure 4.23a of Chapter 4.2.2, a strong agreement is observed. However, it should be noted that the application of established models for COARE3.6 and ECUME yields results over a wider domain, as no flags or restrictions have been applied to the raw R/V Ron Brown data.

Figure 4.29c displays the discrepancies in latent heat flux (LHF) between ECUME and COARE3.6. The results obtained from ECUME show an underestimation compared to COARE3.6. This underestimation becomes more pronounced with higher wind speeds and greater humidity gradients. This finding aligns with the observed lower moist transfer coefficient (C_E) obtained from ECUME, as illustrated in Figure 4.28c. However, this underestimation contradicts the results presented in Figure 4.17a of Chapter 4.2.1, where an overestimation of LHF in ECUME is observed compared to COARE3.6. The dataset used in Chapter 4.2.1, known as the cycle 43h22tg3 dataset, incorporates several coupled SURFEX schemes, including the ECUME parameterization. In contrast, the offline model used here only employs the ECUME parameterization. The discrepancy between the offline ECUME model and the cycle 43h22tg3 dataset suggests that the LHF estimation in ECUME may undergo further adjustments in the SURFEX schemes to obtain the final results. The LHF results obtained within the ECUME parameterization are divided by the latent heat of vaporization ($\mathcal{L}v$) and the atmospheric density (ρ_a). This division allows the LHF to represent the rate of energy transfer per unit area due to water evaporation from the Earth's surface. The obtained heat flux is then outputted and transferred to subsequent cycles in the SURFEX model. Further analysis of the subsequent cycles is still pending and requires further investigation.

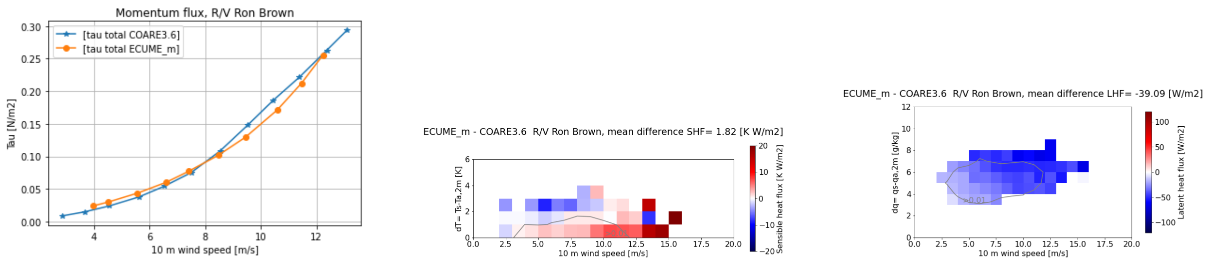

(a) Momentum flux (b) Sensible heat flux (c) Latent heat flux

Figure 4.29: Comparing the air-sea fluxes determined using COARE3.6 and ECUME

4.3.4. Comparative Analysis of the Roughness Length

As previously mentioned, the parameterization of the roughness length (z_0) in COARE3.6 follows Eq. 2.37, as described in Chapter 2.3. In ECUME, however, the determination of z_0 the occurs in the final step, outside the iterative procedure, utilizing Eq. 2.52. Both methods utilize the friction velocity (u_*) to compute z_0. Figure 4.30a displays the results of the u_*, representing the magnitude of wind speed fluctuations. Higher values of u_* indicate increased turbulence, which is associated with higher momentum fluxes. The depicted u_* values align with the momentum fluxes presented in Figure 4.29a against the 10 m wind speed (U_{10m}), demonstrating an overestimation in ECUME compared to COARE3.6 up to 8 m/s, followed by an underestimation. Figure 4.30b displays the calculated values of z_0 plotted against the 10 m wind speed. The observed pattern for z_0 shows a consistent trend of overestimation and underestimation as observed for u_*. The parameter z_0 represents the effective height of surface roughness elements that impede the airflow. Therefore, larger values of z_0 indicate a rougher surface with increased wind resistance.

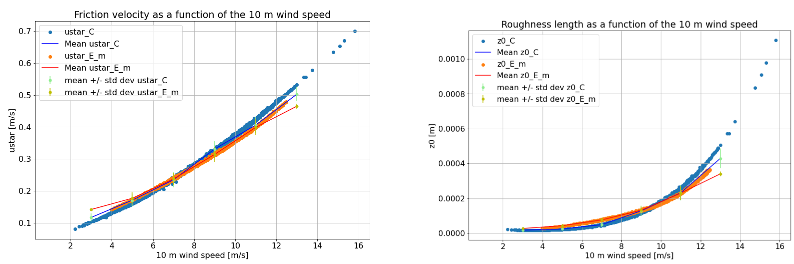

(a) Friction velocity (b) Roughness length

Figure 4.30: Comparing the friction velocity (u_*) and roughness length (z_0) determined using COARE3.6 and ECUME

In the case of low wind speeds, u_* obtained from ECUME is higher than that obtained from COARE3.6. Consequently, this would result in a wind profile with higher wind speeds for ECUME compared to COARE3.6. However, the shape of the wind profile is ultimately determined by the combined effects of u_* and z_0, as well as the influence of stability. The explicit determination of z_0, outside the iterative procedure of ECUME, is investigated in Chapter 4.4.3.

4.4. Understanding the Sensitivity of Air-Sea Fluxes: Exploring Neutral Transfer Coefficients and Stability Functions

The sensitivity analysis of air-sea fluxes to changes in neutral transfer coefficients and stability functions holds paramount importance in accurately modeling the exchange of momentum, heat, and moisture between the atmosphere and the ocean surface. First, this section delves into the investigation of the impact of different formulations for calculating the neutral transfer coefficients on air-sea fluxes. The ECUME and ECUME6 parameterizations, as noted in Chapter 2.3.4, employ distinct formulations for determining the neutral transfer coefficients. Comparing the neutral transfer coefficients and the resulting outcomes provides valuable insights into the sensitivity of these fluxes under varying formulations of neutral transfer coefficients. Alongside neutral transfer coefficients, stability functions play a pivotal role in establishing the relationship between turbulence-induced air-sea fluxes and profiles of wind velocity, potential temperature, and water vapor. The stability functions utilized in COARE3.6 are compared to those employed in ECUME. The findings offer valuable understanding regarding the sensitivity of air-sea fluxes to fluctuations in stability functions. Finally, the initially explicitly determined roughness length (z_0) in ECUME is integrated into the iterative procedure, allowing for its value to be explicitly determined.

4.4.1. Sensitivity of Air-Sea Fluxes to Changes in Neutral Transfer Coefficient

As demonstrated in Chapter 4.2.1, the utilization of the ECUME6 parameterization results in notably higher LHF results compared to ECUME. Conversely, in the case of SHF, ECUME6 only yields higher values for significant potential temperature gradients, as illustrated in Chapter 4.2.2. As described in Chapter 4.2.1, the primary distinction between ECUME and ECUME6 lies in the adoption of different formulations for calculating the neutral transfer coefficients. In order to assess the sensitivity of the outcomes to the formulation changes, the ECUME6 formulations for parameterizing the neutral coefficients are implemented in the ECUME parameterization. The specific formulations for ECUME can be found in Table 2.1, while the corresponding formulations for ECUME6 are provided in Table 2.2.

The figures depicting the 10 meter neutral transfer coefficient as a function of the 10 meter neutral wind, labeled as Figures 4.31a to 4.31c, illustrate that the drag, temperature, and moist neutral transfer coefficients are higher in ECUME6 (referred to as ECUME_m_6) compared to ECUME (referred to as ECUME_m) when the same neutral wind speed is employed. These results align with Figure 2.4a, adapted from Roehrig et al. (2020).

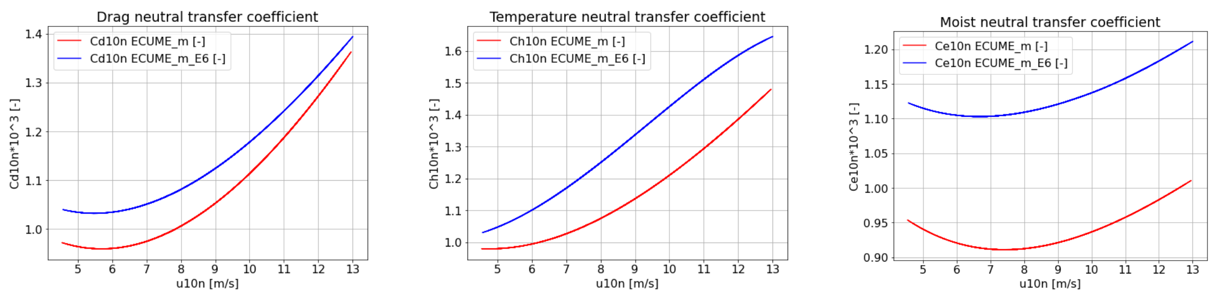

(a) Neutral drag coefficient

(b) neutral temperature transfer coefficient

(c) neutral moist transfer coefficient

Figure 4.31: Comparing polynomial functions ECUME and ECUME6

In order to assess the extent of influence resulting from changes in the formulations of the neutral transfer coefficient, the fluxes are calculated using the formulations employed in the ECUME6 parameterization and compared to the fluxes obtained with the ECUME formulations. The analysis is conducted by examining

Figure 4.32a, which indicates a slight average increase of 7.7% in momentum flux when the ECUME6 formulation for the neutral drag coefficient is applied. Furthermore, Figure 4.32b demonstrates an average increase of approximately 14.3% in SHF when employing the ECUME6 formulation for the neutral temperature transfer coefficient. Additionally, Figure 4.32c presents an average increase of around 18.1% in LHF when utilizing the ECUME6 formulation for the moist transfer coefficient. These increments align with the changes observed in Figures 4.31a to 4.31c, emphasizing that the formulation for the moist transfer coefficient undergoes the most significant alteration.

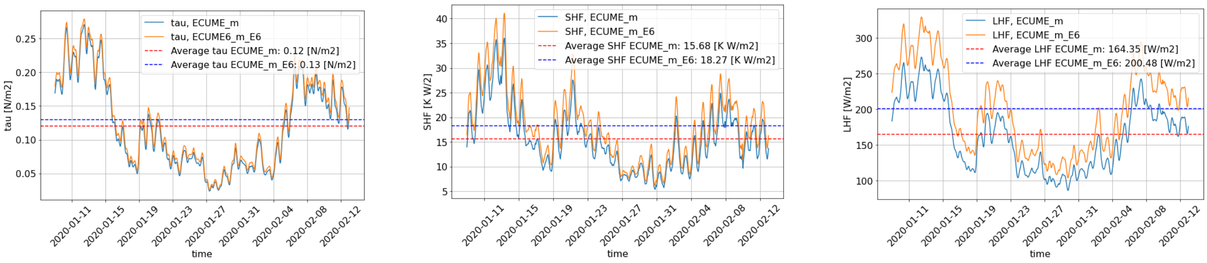

(a) Tau (b) SHF (c) LHF

Figure 4.32: Comparing fluxes determined using the polynomial functions used in ECUME and ECUME6

As depicted in Figures 4.32a to 4.32c, replacing the polynomial function used in ECUME with the polynomial functions from ECUME6 results in higher air-sea fluxes. To further evaluate the sensitivity, the SHF and LHF matrix flux diagnostics are compared. The results are shown in Figures 4.33b and 4.33c. The momentum flux is examined by plotting it as a function of the 10 m wind speed in Figure 4.33a. The results demonstrate that the momentum flux obtained from ECUME_m is consistently lower than that obtained from ECUME_m_E6, and this difference becomes more pronounced with increasing wind speed. In the case of the SHF diagnostic, as depicted in Figure 4.33b, no significant discrepancies are observed for low wind speeds. However, for moderate wind speeds, the SHF obtained from ECUME_m_E6 is higher compared to ECUME_m. Conversely, for winds speeds above 15 m/s, the opposite trend is observed, with higher SHF values obtained from ECUME_m. Figure 4.31b displays higher values of C_{H10n} when using ECUME_m_E6. However, it is important to note that the results in this figure are only provided for $\Delta u_{10n} = 13$ due to binning, while Figure 4.33b includes wind speeds up to 20 m/s. The overestimation of SHF obtained from ECUME_m for wind speeds greater than 15 m/s suggests that in this range, the C_{H10n} values obtained from ECUME_m will be higher compared to those obtained from ECUME_m_E6.

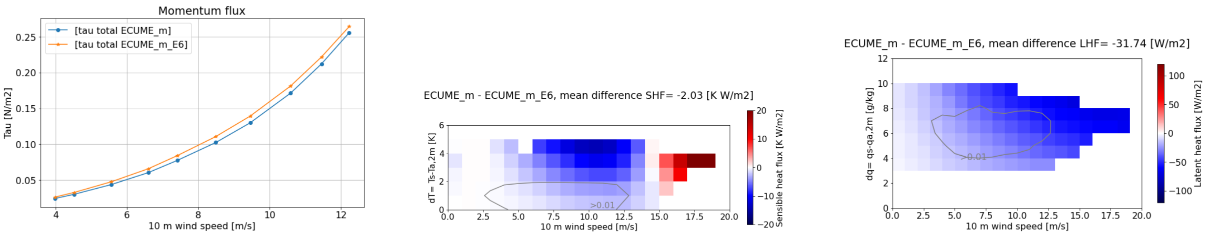

(a) Tau (b) SHF (c) LHF

Figure 4.33: Comparing flux diagnostics obtained using the polynomial functions used in ECUME and ECUME6

4.4.2. Sensitivity of Air-Sea Fluxes to Changes in Stability Functions

To relate the turbulence air-sea fluxes to their respective profiles of wind velocity, potential temperature and water vapor, parameterizations employ flux-profile relationships. As discussed in Chapter 2.3, the most commonly utilized relationships are derived from the Monin-Obukhov (MO) similarity theory, which posits that the non-dimensional gradients of velocity, temperature, and humidity are universal functions of atmospheric stability. Numerous semi-empirical stability functions have been developed based on these flux-profile relationships. The prevailing forms typically combine the Kansas-type formulae with a formulation that adheres to the theoretical scaling limit in highly convective conditions (Edson et al., 2004). The values of the constants used in the Businger-Dyer formulae are determined through various experiments. In the COARE3.6 parameterization, the constants derived from the Kansas experiment for stable profile functions, have been substituted with those proposed by Beljaars and Holtslag (C. W. Fairall et al., 2003), whereas ECUME employs the Kansas constants (Le Moigne, 2018).

To assess the sensitivity of the air-sea fluxes to the stability functions employed, the stability functions for wind and temperature are presented as functions of the dimensionless stability parameter z/L. As the analyzed conditions are characterized as unstable, with a z/L ratio less than 1, convection replaces shear as the primary source of turbulence. Consequently, the analysis focuses on investigating the dimensionless profile functions under these conditions. Figures 4.34a and 4.34b illustrate that, for the same z/L value, the COARE stability functions yield lower values compared to the ECUME stability functions. The higher value of the stability function in ECUME indicates a weaker stabilizing effect on the atmospheric variables, implying a relatively lesser suppression of turbulence and vertical mixing. Generally, this leads to increased turbulent transport and enhanced fluxes. This effect is likewise demonstrated in Figures 4.35a to 4.35c. Comparing these reductions to the findings in Chapter 4.4.1, which examined the sensitivity to the formulation of neutral transfer coefficients, it can be observed that the impact of changing the stability function on the SHF and LHF is relatively minor. However, the effect on the momentum flux is more pronounced.

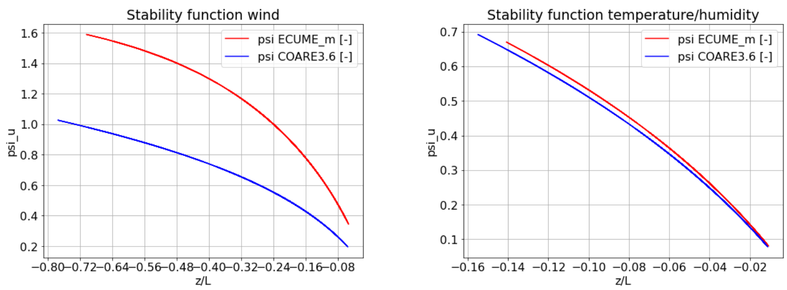

(a) Dimensionless shear functions (b) Dimensionless potential temperature functions

Figure 4.34: Comparing stability functions COARE3.6 and ECUME against dimensionless stability parameter z/L

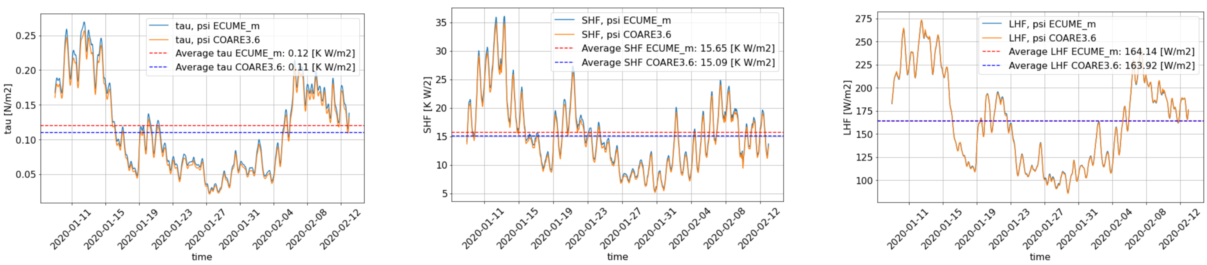

(a) Tau (b) SHF (c) LHF

Figure 4.35: Comparing fluxes determined using the stability functions used in COARE3.6 and ECUME

To further evaluate the sensitivity, the SHF and LHF matrix flux diagnostics are compared. The results are shown in Figures 4.36b and 4.36c. The momentum flux is examined by plotting it as a function of the 10 m wind speed in Figure 4.36a. The results demonstrate that the momentum flux obtained from ECUME_m_phi, representing outcomes using adjusted stability functions, is lower than that obtained from ECUME_m, with a slight increase in discrepancy for an increasing wind speed. In the case of SHF, as depicted in Figure 4.36b, the ECUME_m_phi parameterization exhibits lower SHF values for higher potential temperature gradients, while showing comparable results for lower potential temperature gradients. The impact of adjusting the stability functions on the LHF results is relatively minimal, as illustrated in Figure 4.36c.

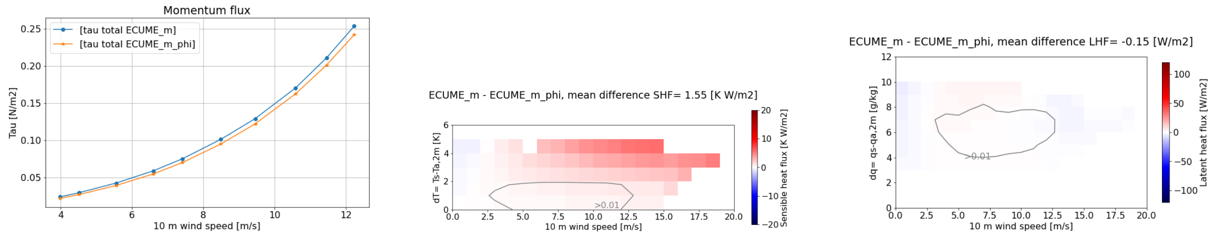

(a) Tau (b) SHF (c) LHF

Figure 4.36: Comparing flux diagnostics obtained using the stability functions used in ECUME and COARE3.6

4.4.3. Sensitivity of Air-Sea Fluxes to Implementing z_0 Inside Iterative Procedure

In ECUME, the determination of the roughness length (z_0) is explicitly performed outside the iterative procedure, while in COARE3.6, z_0 is implicitly determined. In COARE3.6, z_0 is utilized for calculating the characteristic scales, which represent the magnitude of fluctuations in the respective quantities. In ECUME, the characteristic scales are based on the determined Δu_{10n}, as described in Appendix C. The value of Δu_{10n} is iteratively determined using Eq. 2.49. By rewriting Eq. 2.49 in terms of z_0 and using Eq. 2.26, Δu_{10n} is determined using z_0. The result is shown in Eq. 4.1. By incorporating the rewritten expression for Δu_{10n}, as a function of z_0, and employing Eq. 2.37 to determine z_0 within the iterative procedure of ECUME, z_0 is now implicitly determined, similar to the COARE3.6 method.

$$\Delta u_{10n} \equiv \frac{u_*}{\kappa} \ln\left(\frac{10}{z_0}\right) \tag{4.1}$$

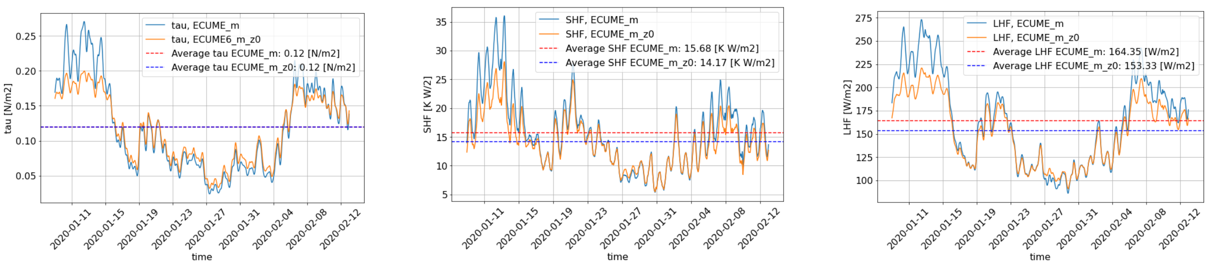

(a) Tau (b) SHF (c) LHF

Figure 4.37: Comparing fluxes determined by implicitly and explicitly including roughness length (z_0)

The fluxes obtained by implicitly including z_0 (referred to as ECUME_m_z_0) are compared to the fluxes obtained from explicitly determining z_0 (referred to as ECUME_m). The results are presented in Figures 4.37a to 4.37c, where ECUME_m represents the use of the ECUME model with explicitly determined z_0, and ECUME_m_z_0 represents the use of the ECUME model with implicitly determined z_0. Figure 4.37a illustrates the momentum flux, showing that the average value remains unchanged. However, the higher momentum fluxes are reduced when including z_0 in the parameterization, whereas the lower momentum fluxes are increased. For the SHF, as shown in Figure 4.37b, ECUME_m_z_0 yields, on average, a slightly smaller SHF compared to ECUME_m, with an average decrease of 10.7%. Similar to the momentum flux, lower fluxes are slightly increased, while higher fluxes are reduced. The fluxes within a moderate range exhibit similar values. Regarding the LHF, presented in Figure 4.37c, a similar pattern is observed. On average, ECUME_m_z_0 produces a slightly reduced LHF compared to ECUME_m, with a decrease of 7.2%.

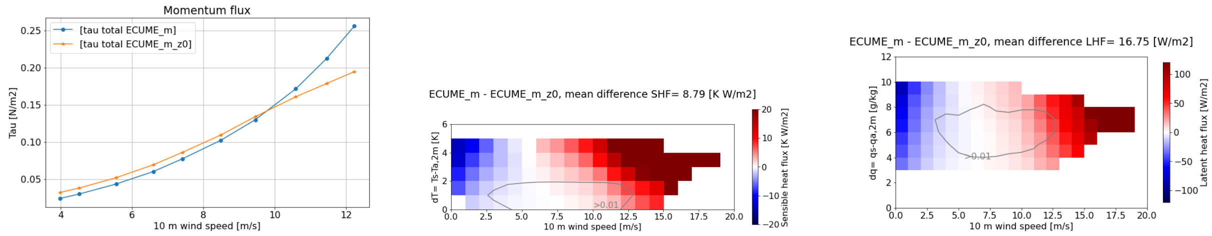

(a) Tau (b) SHF (c) LHF

Figure 4.38: Comparing flux diagnostics for implicitly and explicitly including roughness length (z_0)

As indicated from Figures 4.37a to 4.37c, by rewriting Δu_{10n} as a function of z_0, and thereby implicitly determining z_0, the higher fluxes are reduced, whereas the lower fluxes are increased. To further evaluate the sensitivity, the matrix flux diagnostics are compared for the SHF and LHF, as shown in Figures 4.38b and 4.38c. The momentum flux is examined by plotting it as a function of the 10 m wind speed in Figure 4.38a. The results indicate that for higher wind speeds, the momentum flux obtained from ECUME_m_z_0 is lower compared to ECUME_m, while the opposite trend is observed for wind speeds below 10 m/s. Similar patterns are observed in the flux diagnostics for SHF and LHF. Specifically, for higher wind speeds, the SHF and LHF fluxes obtained from ECUME_m are higher than those obtained from ECUME_m_z_0, whereas the reverse is observed for low wind speeds. Fluxes within a moderate range exhibit comparable values.

5
Discussion

5.1. Evaluation of Eddy Covariance Air-Sea Fluxes: Implications and Limitations

The surface flux diagnostic method proposed by (Hsu et al., 2022) captures a specific wind speed, potential temperature ($\Delta\theta$) and humidity gradient (Δq) range. By visualizing the relationship between input variables and flux using this technique, the errors in transfer coefficients can be determined. These results are applicable within the specified wind, $\Delta\theta$, and Δq range, assuming the observations used for the assessment are accurate. As a consequence, the accuracy of the assessment is heavily influenced by the quality and completeness of the observational data. Factors such as instrumental errors, sensor calibration, and data gaps can introduce variability in the flux results.

Efforts were made to improve the accuracy of the data by applying flags to the processed R/V Ron Brown data and using masks and correction techniques for the raw R/V Meteor data. However, unexpected discrepancies in the corrected R/V Meteor data suggest potential contamination in the measurements, particularly affecting the accuracy of the calculated momentum flux (as evidenced by Figure 4.26b in Chapter 4.2.3). This discrepancy may arise due to incomplete consideration of distortion effects on turbulent components in current numerical models (Drennan, 2006). Moreover, significant differences are observed in the EC latent heat flux (LHF) results obtained from the R/V Ron Brown and R/V Meteor datasets. The average LHF derived from the R/V Ron Brown dataset is $176.43\ W/m^2$, while the average LHF from the R/V Meteor dataset is $124.36\ W/m^2$. This discrepancy persists despite the fact that the wind speed range for the R/V Meteor dataset extends to higher wind speeds, which would typically result in higher LHF values. The disparity in LHF values may be attributed to potential contamination in the measurements, introducing inaccuracies.

Additionally, inaccurate results can be obtained by the application of imprecise masks. Contrary to expectations, applying masks increased the variability in the sensible heat flux (SHF) ratio when comparing EC results to COARE3.6 results, as demonstrated in Chapter 4.1.2. In Appendix F, it is shown that applying masks to the data leads to an increase in air-sea EC fluxes for wind speeds below 5 m/s, resulting in increased variability in the SHF ratio results. However, it is important to note that the use of masks also leads to a slight reduction in the standard error for the EC air-sea fluxes. To enhance the accuracy of the observational results, further investigation into accurate masking and motion correction techniques is required.

5.2. Evaluation of Air-Sea Fluxes Derived from COARE3.6 Parameterization: Implications and Considerations

Given the inherent limitations of the EC method, an additional assessment has been conducted using the COARE3.6 parameterization to evaluate the air-sea fluxes derived from the ECUME and ECUME6 parameterizations. However, it is important to acknowledge that the COARE3.6 parameterization, similar to ECUME and ECUME6, relies on various assumptions and parameterizations to estimate the fluxes. These parameterizations may encounter challenges in accurately estimating fluxes under complex dynamical conditions. Although C. W. Fairall et al. (2003) suggest that the COARE3.6 parameterization achieves an accuracy within 5% for wind speeds ranging from 0 to 10 m/s and within 10% for wind speeds between

10 and 20 m/s, significant disparities between the EC and COARE3.6 air-sea fluxes were observed in Chapter 4.1. The additional assessment utilizing the COARE3.6 parameterization yields valuable insights into the air-sea fluxes derived from the ECUME and ECUME6 parameterizations. However, it is essential to acknowledge the inherent limitations and uncertainties inherent in the COARE3.6 parameterization itself. Therefore, assessment against in situ observations remains essential in order to validate and improve the accuracy of the air-sea flux estimates.

5.3. Implications of Offline Model Comparisons on Air-Sea Flux Estimation

To enable a comparative analysis of the iteratively obtained coefficients using the ECUME and COARE3.6 approaches, separate offline models are constructed for each method. As discussed in Chapter 2.3, in the ECUME parameterization, the drag coefficient is computed based on the 10 meter neutral wind speed value (Δu_{10n}), while the COARE3.6 parameterization utilizes the roughness length (z_0) to determine the drag coefficient (C_D). The trend in the obtained results for both ECUME and COARE3.6 is shown to be highly correlated to the trend observed for the neutral drag coefficients, showing similar over and underestimation when comparing the coefficients for ECUME to COARE3.6. When comparing the air-sea fluxes obtained using the iteratively determined transfer coefficients in the offline model, as presented in Chapter 4.3.3, to the results obtained in Chapter 4.2.1 where the cycle 43h22tg3 dataset is used, similar outcomes are observed for both momentum flux and SHF. However, for LHF, the offline ECUME model underestimates the flux compared to the COARE3.6 model, while an overestimation of the flux is observed when comparing the cycle 43h22tg3 dataset to the COARE3.6 model. The cycle 43h22tg3 dataset utilized in Chapter 4.2.1 incorporates multiple coupled SURFEX schemes, including the incorporation of the ECUME parameterization, whereas the offline model utilized in this analysis exclusively employs the ECUME parameterization. The discrepancy between the offline ECUME model and the cycle 43h22tg3 dataset suggests that the LHF estimation in ECUME may undergo further adjustments in the SURFEX schemes to obtain the final results.

Comparative Analysis of Coefficient Estimation

The observed underestimation in LHF when comparing the LHF results of the offline ECUME model to the COARE3.6 model can be largely attributed to the underestimation in the neutral moist transfer coefficient. As discussed in Chapter 4.3.1, the neutral transfer coefficients (C_{E10N}) obtained from ECUME are significantly lower compared to those obtained from COARE3.6. These findings are consistent with the study conducted by Belamari (2005), which also compared the neutral transfer coefficients of ECUME to those of COARE. However, it is important to note that the study utilized an outdated version of COARE (COARE3.0).

As the neutral transfer coefficients results differ so significantly when comparing ECUME to COARE3.6, it is interesting to gather inside on the observations used for the establishment of the parameterizations. The ECUME parameterization is built upon the comprehensive ALBATROS database, containing about 5600 h of data, which encompasses a decade-long research period from the early 1990s to 2001. This database incorporates data obtained from five dedicated experiments focused on air-sea fluxes: SEMAPHORE, CATCH, FETCH, EQUALANT99, and POMME. These experiments were conducted in the Atlantic Ocean, ranging from the northern to the equatorial regions, as well as in the Mediterranean Sea (Belamari, 2005). In contrast, the COARE parameterization was developed during the TOGA-COARE campaign, which took place in the western Pacific warm-pool region. This region extends from 20°N to 20°S and is bounded by Indonesia to the west and the International Date Line to the east. The COARE parameterization has undergone updates using the extensive ETL1999 database, containing 7216 h of data, (see Appendix B), enabling it to capture a broader range of atmospheric conditions, particularly for higher wind speeds (C. W. Fairall et al., 2003).

The discrepancy in the obtained neutral transfer coefficients could be attributed to the different spatial coverage of the ALBATROS and ETL1999 databases. Consequently, different atmospheric conditions may have been considered in the development of the ECUME and COARE3.6 parameterizations. It is worth noting that for the establishment of ECUME, data from the SEMAPHORE and CATCH experiments were used without accounting for airflow distortion, as the necessary post-treatment of this data has not been achieved at present (Belamari, 2005). In contrast, during the development of COARE3.6, appropriate corrections were implemented to the data when required (C. W. Fairall et al., 2003) (C. W. Fairall et al., 1996).

Correction Effects

Additionally, variations exist in the inclusion of factors such as seawater salinity, gustiness, and the diurnal effects of the cool skin and warm layer, which contribute to the differences observed in the calculated fluxes by the different parameterizations. The ECUME parameterization does not include corrections for cool-skin and warm layer effects, while COARE3.6 does account for these effects. Cool-skin and warm layer effects play a significant role in triggering convection (Pradhan et al., 2022). In a study conducted by C. Fairall et al. (1996), it was found that including the cool skin correction increases the average atmospheric heat input by approximately $11\ W/m^2$, while the warm layer correction decreases it by approximately $5\ W/m^2$. Although gustiness can be included in the ECUME parameterization, the cycle 43h22tg3 dataset utilized in this analysis does not incorporate gustiness corrections. The inclusion of gustiness addresses the mathematical challenge of producing finite sensible and latent heat fluxes as the wind speed approaches zero, leading to more accurate estimations of sensible and latent heat fluxes under low wind speed conditions (C. W. Fairall et al., 2003).

6
Conclusion and Recommendations

The main research goal is to evaluate the accuracy of the ECUME and ECUME6 parameterizations in simulating air-sea fluxes, and to identify the predominant source of error in these parameterizations. This section present the main conclusions drawn from the results by answering the defined sub-questions and gives recommendations for future research.

6.1. Conclusions

Differences in the COARE3.6, ECUME and ECUME6 Parameterizations
The COARE 3.6, ECUME, and ECUME6 parameterizations utilize the Monin-Obukhov Similarity Theory (MOST) to describe the turbulent exchange processes between the atmosphere and the ocean's surface. The development of these parameterizations has relied on various databases, specifically the ETL1999 database for COARE3.6 and the ALBATROS database for ECUME. Additionally, a specific subset of the ALBATROS dataset has been utilized for the development of ECUME6. In COARE, the roughness length is parameterized using measurements of the neutral drag coefficient, whereas in ECUME, the neutral transfer coefficients are parameterized using polynomial functions, which are established through calibration. These polynomial functions relate the neutral transfer coefficients to the 10 m neutral wind speed. ECUME6 follows a similar approach but uses slightly different polynomial functions.

Moreover, the stability functions slightly differ between the models. COARE3.6 uses constants proposed by Beljaars and Holtslag for stable conditions instead of those derived from the Kansas experiment, while ECUME and ECUME6 employ the Kansas constants. For unstable conditions, all three models incorporate both the Kansas and free convection forms, but with slightly different numerical values. Furthermore, COARE incorporates separate models to account for the ocean's cool skin and diurnal warm layer, which are not utilized in ECUME and ECUME6.

Comparing the EC and COARE3.6 Method
For both results obtained from R/V Ron Brown and R/V Meteor, the EC method shows greater variability than the COARE3.6 method when estimating latent heat flux (LHF), sensible heat flux (SHF), and momentum flux. The average ratio of EC fluxes to COARE3.6 fluxes varies based on wind speed, with higher ratios observed for SHF and momentum flux at lower wind speeds. Notably, the COARE3.6 method encounters challenges in adequately capturing dynamic fluctuations, particularly under conditions of low wind speeds associated with unstable atmospheric conditions.

The comparison between the EC and COARE3.6 method, using the matrix flux diagnostics, reveals that the EC method tends to yield higher flux values for SHF. The fluctuation pattern intensifies with higher potential temperature gradients, indicating the COARE3.6 method's inability to capture dynamic fluctuations effectively. When analyzing LHF data from R/V Ron Brown, the EC method demonstrates higher values for elevated wind speeds compared to the COARE3.6 method. However, contrasting results are obtained when utilizing data from R/V Meteor, which can be attributed to incomplete considerations of distortion effects on turbulent components in existing numerical models. The presence of fluctuations and uncertainties in EC measurements emphasizes the need for proper corrections and further refinement of measurement techniques.

Assessment of the ECUME and ECUME6 parameterization
When comparing the ECUME and ECUME6 parameterizations, it is observed that ECUME generally produced higher values for the humidity difference (Δq), while ECUME6 produced higher values for the 10 m wind speed (U_{10m}). This pattern is consistently observed across different measurement domains (R/V Ron Brown and R/V Meteor). The positive differences in LHF and SHF obtained by subtracting the ECUME diagnostic from the ECUME6 diagnostic indicate that the ECUME6 parameterization yields higher values for both LHF and SHF.

By subtracting the EC LHF diagnostic from the ECUME LHF diagnostics, overestimations in LHF are observed at high wind speeds, while negative discrepancies in LHF are observed for low wind speeds. Using the EC data from R/V Ron Brown, a small average difference of -0.84 W/m^2 is found, indicating good agreement between the two. However, using EC data from R/V Meteor, the average overestimation amounts to 56.69 W/m^2. Assessing ECUME6, predominantly observations in LHF are observed. The overestimations are more pronounced at higher wind speeds. Using the EC data from R/V Ron Brown, an average overestimation of 23.95 W/m^2 is observed, whereas using data from R/V Meteor, an average overestimation of 82.69 W/m^2 is observed.

When evaluating ECUME against the COARE3.6 parameterization, a slight overestimation of LHF at high wind speeds is observed, while less dependence on humidity difference is observed. The average difference between ECUME and COARE3.6 equals 4.54 W/m^2 using R/V Ron Brown data and 7.54 W/m^2 using R/V Meteor data. For ECUME6, consistently overestimations in LHF are observed when compared to COARE3.6. The overestimation increases with higher wind speeds. The average difference between ECUME6 and COARE3.6 equals 29.59 W/m^2 using R/V Ron Brown data and 31.17 W/m^2 using R/V Meteor data.

For the SHF, the observed results for ECUME and ECUME6 are comparable when assessed to both EC observations and COARE3.6 results. By subtracting the EC SHF diagnostic from the ECUME and ECUME6 SHF diagnostics, the SHF is underestimated for low wind speeds, and overestimated for high wind speeds. When subtracting the COARE3.6 SHF from the ECUME and ECUME6 diagnostics, a similar pattern is observed, with slightly greater overestimations in SHF for higher wind speeds.

When comparing the momentum fluxes estimated by ECUME and ECUME6 with those obtained using the COARE3.6 parameterization and EC observations, both comparisons consistently reveal a slight underestimation of the momentum flux by ECUME and ECUME6. This underestimation increase as wind speed rises.

Sources of Error in ECUME and ECUME6
The differences obtained in air-sea fluxes between the developed offline ECUME model and offline COARE3.6 model, are highly related to the obtained neutral transfer coefficients. Using the offline developed ECUME model, it is observed that compared to COARE3.6, the ECUME parameterization exhibits a tendency to overestimate the neutral drag coefficients (C_{D10n}), particularly for neutral wind speeds up to approximately 6.5 m/s, after which an underestimation is observed. Regarding the neutral temperature transfer coefficient (C_{H10n}), the ECUME parameterization exhibits higher values compared to COARE3.6 for wind speeds above 5 m/s. Conversely, the ECUME parameterization consistently underestimates the neutral moist coefficient (C_{E10n}) when compared to COARE3.6. These disparities in the obtained neutral transfer coefficients can be attributed to use of the different databases, namely ALBATROS and ETL1999, for the development of ECUME and COARE3.6, resulting in the consideration of different atmospheric conditions.

The offline implementation of the the polynomial functions used in the ECUME and ECUME6 parameterizations highlights the sensitivity of air-sea fluxes to changes in the parameterization of neutral transfer coefficients. When utilizing the ECUME6 polynomial functions, significantly higher flux values are obtained compared to those obtained using the polynomial functions of the ECUME parameterization.

6.2. Recommendations

Based on results and conclusions in this study, this section describes the recommendations for future research.

In this research, the COARE, ECUME and ECUME6 parameterization are assessed using the EC observations obtained from R/V Ron Brown and R/V Meteor. As the accuracy of this assessment is highly dependent on the reliability of air-sea flux obtained using the EC method, future research should focus on the identification and addressing of potential sources of contamination. Comprehensive analyses should be conducted to understand the impact of environmental factors, such as seawater spray and ship-generated turbulence, on the accuracy of flux measurements. Improved correction algorithms and data filtering techniques should be developed to mitigate the effects of contamination and ensure more accurate flux estimates.

The COARE3.6, ECUME and ECUME6 parameterizations, have shown limitations in certain environmental conditions. Further research is needed to refine and expand existing parameterization schemes to encompass a wider range of atmospheric and oceanic conditions. This could involve incorporating additional physical processes, such as wave-induced effects, surface wave breaking, and sea spray generation, into the parameterization models. Additionally, efforts should be made to validate and calibrate the parameterization schemes using high-quality observational data from diverse marine environments.

The performance and applicability of parameterization schemes are strongly influenced by the choice of input datasets, which encompass meteorological and oceanographic variables. Therefore, the selection of appropriate datasets plays a crucial role in improving the performance and applicability of these schemes. To update the existing parameterizations, it is highly recommended to rigorously test the schemes using different datasets, allowing for necessary adjustments and refinements. By incorporating a diverse range of datasets, the accuracy and effectiveness of the parameterization schemes can be enhanced, leading to more reliable predictions and simulations in the field of meteorology and oceanography.

References

Zhou, X., Ray, P., Barrett, B. S., & Hsu, P. C. (2020). Understanding the bias in surface latent and sensible heat fluxes in contemporary AGCMs over tropical oceans. *Climate Dynamics*, *55*(11-12), 2957–2978. https://doi.org/10.1007/s00382-020-05431-y

Reeves Eyre, J. E., Zeng, X., & Zhang, K. (2021). Ocean Surface Flux Algorithm Effects on Earth System Model Energy and Water Cycles. *Frontiers in Marine Science*, *8*. https://doi.org/10.3389/fmars.2021.642804

Brunke, M. A., Fairall, C. W., Zeng, X., Eymard, L., & Curry, J. A. (2003). Which bulk aerodynamic algorithms are least problematic in computing ocean surface turbulent fluxes? *Journal of Climate*, *16*(4), 619–635. https://doi.org/10.1175/1520-0442(2003)016<0619:WBAAAL>2.0.CO;2

Hsu, C. W., DeMott, C. A., Branson, M. D., Reeves Eyre, J., & Zeng, X. (2022). Ocean Surface Flux Algorithm Effects on Tropical Indo-Pacific Intraseasonal Precipitation. *Geophysical Research Letters*, *49*(7). https://doi.org/10.1029/2021GL096968

Pradhan, M., Rao, S. A., Bhattacharya, A., & Balasubramanian, S. (2022). Improvements in diurnal cycle and its impact on seasonal mean by incorporating coare flux algorithm in cfs. *Frontiers in Climate*, *3*. https://doi.org/10.3389/fclim.2021.792980

Cronin, M. F., Gentemann, C. L., Edson, J. B., Ueki, I., Bourassa, M., Brown, S., Clayson, C. A., Fairall, C., T. Farrar, J., Gille, S. T., Gulev, S., Josey, S., Kato, S., Katsumata, M., Kent, E. C., Krug, M., Minnett, P. J., Parfitt, R., Pinker, R. T., … Zhang, D. (2019). Air-sea fluxes with a focus on heat and momentum. https://doi.org/10.3389/fmars.2019.00430

Yu Xiangze Jin Robert Weller, L. A. (2008). *Multidecade Global Flux Datasets from the Objectively Analyzed Air-sea Fluxes (OAFlux) Project: Latent and Sensible Heat Fluxes, Ocean Evaporation, and Related Surface Meteorological Variables* (tech. rep.). http://oaflux.whoi.edu/.

Drennan, W. (2006). On parameterizations of air–sea fluxes. In *Atmosphere-ocean interactions* (pp. 01–33). WIT Press. https://doi.org/10.2495/978-1-85312-929-2/01

Lykossov, V. N. (2009). Atmospheric and Oceanic Boundary Layer Physics. In *Wind stress over the ocean* (pp. 54–81). Cambridge University Press. https://doi.org/10.1017/cbo9780511552076.004

Siebesma, A., Bony, S., Jakob, C., & Stevens, B. (2020). Parameterising Clouds. In *Clouds and climate: Climate science's greatest challenge* (pp. 170–217). Cambridge University Press. https://doi.org/10.1017/9781107447738.007

Burba, G., & Anderson, D. (2010). *A Brief Practical Guide to Eddy Covariance Flux Measurements: Principles and Workflow Examples for Scientific and Industrial Applications*. https://doi.org/10.13140/RG.2.1.1626.4161

Le Moigne, P. (2018). *SURFEX SCIENTIFIC DOCUMENTATION* (tech. rep.).

Salesky, S. T. (2014). *Monin-obukhov similarity and convective organization in the unstable atmospheric boundary layer*. The Pennsylvania State University.

Fairall, C. W., Bradley, E. F., Rogers, D. P., Edson, J. B., & Young, G. S. (1996). Bulk parameterization of air-sea fluxes for tropical oceanglobal atmosphere coupled-ocean atmosphere response experiment. *Journal of Geophysical Research: Oceans*, *101*(C2), 3747–3764. https://doi.org/10.1029/95JC03205

Venora, A. (2009). *Monin-Obukhov Similarity Theory Applied to Offshore Wind Data Validation of Models to Estimate the Offshore Wind Speed Profile in the North Sea* (tech. rep.). Delft University of Technology.

Stull, R. B. (1988). *An introduction to boundary layer meteorology*. https://doi.org/10.1007/978-94-009-3027-8

Edson, J. B., Zappa, C. J., Ware, J. A., McGillis, W. R., & Hare, J. E. (2004). Scalar flux profile relationships over the open ocean. *Journal of Geophysical Research: Oceans*, *109*(8). https://doi.org/10.1029/2003JC001960

Wallace, J. M., & Hobbs, P. V. (2006). *Atmospheric science: An introductory survey*. Academic Press.

Fairall, C. W., Bradley, E. F., Hare, J. E., Grachev, A. A., & Edson, J. B. (2003). Bulk parameterization of air-sea fluxes: Updates and verification for the COARE algorithm. *Journal of Climate*, *16*(4), 571–591. https://doi.org/10.1175/1520-0442(2003)016<0571:BPOASF>2.0.CO;2

NCAR. (2023). *TOGA COARE*. https://www.eol.ucar.edu/field_projects/toga-coare

Businger, J. A., Wyngaard, J. C., Izumi, Y., & Bradley, E. F. (1971). Flux-profile relationships in the atmospheric surface layer. *Journal of Atmospheric Sciences*, *28*(2), 181–189. https://doi.org/10.1175/1520-0469(1971)028<0181:FPRITA>2.0.CO;2

Godfrey, J., & Beljaars, A. (1991). *On the turbulent fluxes of buoyancy, heat and moisture at the air-sea interface at low wind speeds*. https://books.google.nl/books?id=YgI3zwEACAAJ

Edson, J. B., Jampana, V., Weller, R. A., Bigorre, S. P., Plueddemann, A. J., Fairall, C. W., Miller, S. D., Mahrt, L., Vickers, D., & Hersbach, H. (2013). On the exchange of momentum over the open ocean. *Journal of Physical Oceanography*, *43*(8), 1589–1610. https://doi.org/10.1175/JPO-D-12-0173.1

Bariteau, L. (2023). Coare36vn_zrf_et.py. https://github.com/NOAA-PSL/COARE-algorithm/blob/master/Python/COARE3.6/coare36vn_zrf_et.py

CNRM. (2023). Surfex.

Belamari, S. (2005). Report on uncertainty estimates of an optimal bulk formulation for surface turbulent fluxes. *MERSEA IP Deliverable 412*, 1–29.

Weill, A., Eymard, L., Caniaux, G., Hauser, D., Planton, S., Dupuis, H., Brut, A., Guerin, C., Nacass, P., Butet, A., Cloché, S., Pedreros, R., Durand, P., Bourras, D., Giordani, H., Lachaud, G., & Bouhours, G. (2003). Toward a better determination of turbulent air–sea fluxes from several experiments. *Journal of Climate*, *16*(4), 600–618. https://doi.org/https://doi.org/10.1175/1520-0442(2003)016<0600:TABDOT>2.0.CO;2

Roehrig, R., Beau, I., Saint-Martin, D., Alias, A., Decharme, B., Guérémy, J. F., Voldoire, A., Abdel-Lathif, A. Y., Bazile, E., Belamari, S., Blein, S., Bouniol, D., Bouteloup, Y., Cattiaux, J., Chauvin, F., Chevallier, M., Colin, J., Douville, H., Marquet, P., … Sénési, S. (2020). The CNRM Global Atmosphere Model ARPEGE-Climat 6.3: Description and Evaluation. *Journal of Advances in Modeling Earth Systems*, *12*(7). https://doi.org/10.1029/2020MS002075

Bourras, D., Weill, A., Caniaux, G., Eymard, L., Bourlès, B., Letourneur, S., Legain, D., Key, E., Baudin, F., Piguet, B., Traulle, O., Bouhours, G., Sinardet, B., Barrié, J., Vinson, J., Boutet, F., Berthod, C., & Clémençon, A. (2009). Turbulent air-sea fluxes in the gulf of guinea during the amma experiment. *Journal of Geophysical Research: Oceans*, *114*, n/a–n/a. https://doi.org/10.1029/2008JC004951

Lebeaupin, C. (2023a). SURFEX-NWP ecume code.

Lebeaupin, C. (2023b). SURFEX-NWP ecume6 code.

Stevens, B., Bony, S., Farrell, D., Ament, F., Blyth, A., Fairall, C., Karstensen, J., Quinn, P. K., Speich, S., Acquistapace, C., Aemisegger, F., Albright, A. L., Bellenger, H., Bodenschatz, E., Caesar, K. A., Chewitt-Lucas, R., De Boer, G., Delanoë, J., Denby, L., … Zöger, M. (2021). EUREC4A. https://doi.org/10.5194/essd-13-4067-2021

Schirmacher, I. (2021). *Shipborne Measurements of Surface Heat Fluxes over the Tropical North Atlantic* (tech. rep.). Hamburg University.

Quinn, P. K., Thompson, E. J., Coffman, D. J., Baidar, S., Bariteau, L., Bates, T. S., Bigorre, S., Brewer, A., De Boer, G., De Szoeke, S. P., Drushka, K., Foltz, G. R., Intrieri, J., Iyer, S., Fairall, C. W., Gaston,

C. J., Jansen, F., Johnson, J. E., Krüger, O. O., … Zuidema, P. (2021). Measurements from the RV Ronald H. Brown and related platforms as part of the Atlantic Tradewind Ocean-Atmosphere Mesoscale Interaction Campaign (ATOMIC). *Earth System Science Data*, *13*(4), 1759–1790. https://doi.org/10.5194/essd-13-1759-2021

Mohr, W., Kinne, S., Baier, K., Baranowski, D., Chilinski, M., Gollop, J., de Groot, G., Grosz, R., Helfer, K., Ibáñez-Landeta, A., Kalesse, H., Kidane, A., Makuch, P., Meyer, M., Morfa-Avalos, Y., Neuberger, A., Nowak, J., Raeke, A., Rollo, C., … Kinne, S. (2020). *METEOR-Berichte EUREC 4 A Campaign Bridgetown (Barbados)-Ponta Delgada (Portugal) EUREC 4 A* ++ (tech. rep.).

Parker Maritime. (2011). *REPORT FS Meteor* (tech. rep.).

Bengtsson, L., Andrae, U., Aspelien, T., Batrak, Y., Calvo, J., de Rooy, W., Gleeson, E., Hansen-Sass, B., Homleid, M., Hortal, M., Ivarsson, K.-I., Lenderink, G., Niemelä, S., Nielsen, K. P., Onvlee, J., Rontu, L., Samuelsson, P., Muñoz, D. S., Subias, A., … Køltzow, M. Ø. (2017). The harmonie–arome model configuration in the aladin–hirlam nwp system. *Monthly Weather Review*, *145*(5), 1919–1935. https://doi.org/https://doi.org/10.1175/MWR-D-16-0417.1

KNMI. (2023). Weather and climate models.

Edson, J. B., Hinton, A. A., Prada, K. E., Hare, J. E., & Fairall, C. W. (1998). *Direct Covariance Flux Estimates from Mobile Platforms at Sea** (tech. rep.).

Pedreros, R., Dardier, G., Dupuis, H., Graber, H. C., Drennan, W. M., Weill, A., Guérin, C., & Nacass, P. (2003). Momentum and heat fluxes via the eddy correlation method on the R/V L'Atalante and an ASIS buoy. *Journal of Geophysical Research: Oceans*, *108*(11). https://doi.org/10.1029/2002jc001449

François Anctil, Mark A. Donelan, William M. Drennan, & Hans C. Graber. (1994). Eddy-Correlation Measurements of Air-Sea Fluxes from a Discus Buoy.

Thor I. Fossen. (2002). *Marine Control Systems: guidance, navigation and control of ships, rigs and underwater vehicles* (Vol. 28). Journal of Guidance Control; Dynamics - J GUID CONTROL DYNAM. http://www.marinecybemetics.com

Songtao, Z., & Peng, Z. (2021). L2-gain based adaptive robust heel/roll reduction control using fin stabilizer during ship turns. *Journal of Marine Science and Engineering*, *9*(1), 1–17. https://doi.org/10.3390/jmse9010089

E. K. Webb, G. I. Pearman, & R. Leuning. (1980). Correction of flux measurements for density effects due to heat and water vapour transfer. *Quarterly Journal of the Royal Meteorological Society*, *106*, 85–100.

Foken, T. (2017). *Micrometeorology: Second edition*. Springer-Verlag Berlin Heidelberg. https://doi.org/10.1007/978-3-642-25440-6

Mikrometeorologie, A., Mauder, M., & Foken, T. (2004). *UNIVERSITÄT BAYREUTH Documentation and Instruction Manual of the Eddy Covariance Software Package TK2* (tech. rep.). http://www.bayceer.uni-bayreuth.de/mm/

Roland Stull. (1995). *Meteorology for Scientists and Engineers* (3rd ed.).

J. Marshall & R. Alan Plumb. (1959). *Atmosphere, Ocean, and Climate Dynamics: An Introductory Text*.

Butterworth, B. J., & Miller, S. D. (2016). Automated underway eddy covariance system for air-sea momentum, heat, and CO2 fluxes in the Southern Ocean. *Journal of Atmospheric and Oceanic Technology*, *33*(4), 635–652. https://doi.org/10.1175/JTECH-D-15-0156.1

Milrad, S. (2018). Isopleths and Upper-Tropospheric Charts. In *Synoptic analysis and forecasting* (pp. 49–63). Elsevier. https://doi.org/10.1016/b978-0-12-809247-7.00005-3

Tout, D., Garnier, B., Randall, R., Oke, T. R., & Ohmura, A. (1968). *Climatological Bulletin* (tech. rep.). McGill University.

Fairall, C., Bradley, E., Godfrey, J., Wick, G., Edson, J., & Young, G. (1996). Cool-skin and warm-layer effects on sea surface temperature. *J. Geophys. Res.*, *101*, 1295–1308. https://doi.org/10.1029/95JC03190

A
COARE Parameterization

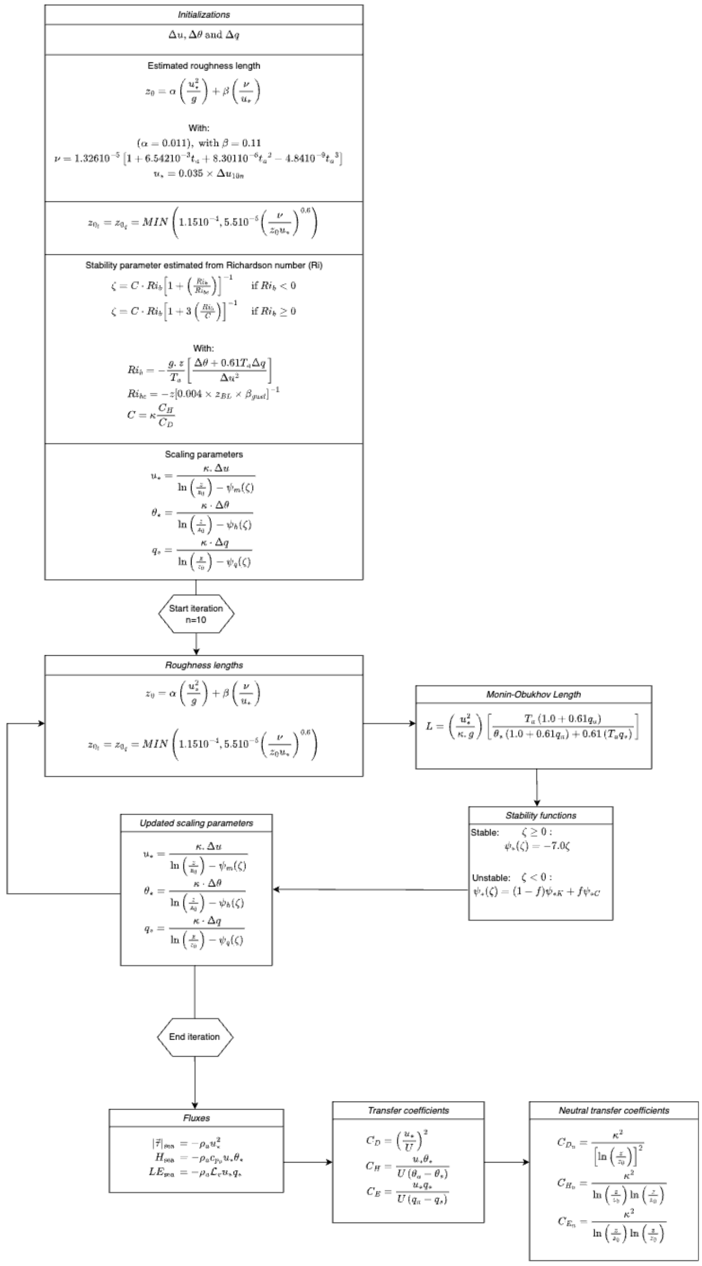

Figure A.1: Flow-chart of the COARE parameterization, corrections are not included

B

ETL1999 Database

The ETL1999 database was created based on cruises conducted by the National Oceanic and Atmospheric Administration (NOAA) Environmental Technology Laboratory (ETL). This database, ETL1999, serves as the foundation for developing the COARE3.6 parameterization.

Table B.1: Overview of ETL air–sea flux and bulk meteorological data cruises used for the development of COARE3.6, obtained from C. W. Fairall et al. (2003)

Cruise name	Dates	Hours	Vessel	Lat	Lon
TIWE	21 Nov-13 Dec 1991	460	Moana Wave	$0°$	$140°$W
ASTEX	6-28 Jun 1992	390	M. Baldrige	$30°$N	$25°$W
COARE-1	11 Nov-3 Dec 1992	589	Moana Wave	$2°$S	$156°$E
COARE-2	17 Dec 1992-11 Jan 1993	648	Moana Wave	$2°$S	$156°$E
COARE-3	28 Jan-16 Feb 1993	385	Moana Wave	$2°$S	$156°$E
SCOPE	17-28 Sep 1993	305	FLIP	$33°$N	$118°$W
FASTEX	23 Dec 1996-24 Jan 1997	730	Knorr	$45°$N	$10° - 60°$W
JASMINE	5-31 May 1999	654	Ron Brown	$8°$N	$89°$E
NAURU99	15 Jun-18 Jul 199	794	Ron Brown	$0.5°$S	$167°$E
KWAJEX	28 Jul-12 Sep 1999	875	Ron Brown	$8°$N	$167.5°$E
Moorings	14 Sep-21 Oct 1999	746	Ron Brown	$52°$N	$140°$W
PACSF99	11 Nov-2 Dec 1999	640	Ron Brown	$\pm 10°$N	$100°$W

C

ECUME Parametrization

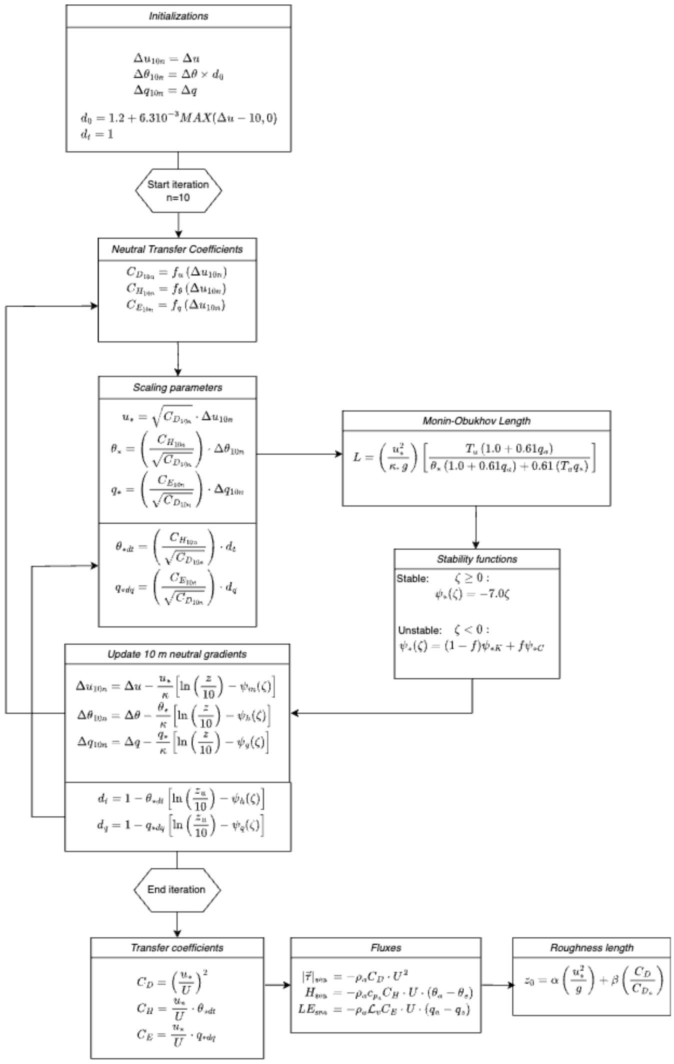

Figure C.1: Flow-chart of the ECUME Parameterization

D

Stability Functions

The stability functions ψ_m and ψ_h (which is equal to ψ_q) that are used in the COARE3.6 parameterization and ECUME parameterizations. ECUME(6) stand for ECUME and ECUME6, as the stability functions used in ECUME6 have not been adjusted compared to ECUME. ψ_m represents the stability function for wind and ψ_h for heat (here referred to as potential temperature).

Table D.1: Stability functions used in COARE and ECUME(6) Bariteau (2023) and Lebeaupin (2023a)

		Wind	Potential temperature
Stable: $(\zeta \geq 0)$	ECUME(6)	$\psi_m(\zeta) = -7.0\zeta$	$\psi_h(\zeta) = -7.0\zeta$
	COARE3.6	$\psi_m(\zeta) = -\left[1 + \zeta + \frac{3}{4}\left(\frac{\zeta - 14.28}{\exp(\Gamma)}\right) + \frac{3}{4} \cdot 8.525\right]$	$\psi_h(\zeta) = -\left[(1 + \frac{2}{3} \cdot \zeta)^{1.5} + \frac{2}{3}\left(\frac{\zeta - 14.28}{\exp(\Gamma)}\right) + 8.525\right]$
Unstable: $(\zeta < 0)$		$\psi_m(\zeta) = (1-f)\psi_{mK} + f\psi_{mC}$ with $f = \frac{\zeta^2}{1+\zeta^2}$	$\psi_h(\zeta) = (1-f)\psi_{hK} + f\psi_{hC}$ with $f = \frac{\zeta^2}{1+\zeta^2}$
Kansas		$\psi_{mK} = 2 \cdot \ln\left(\frac{1+x}{2}\right) + \ln\left(\frac{1+x^2}{2}\right) - 2 \cdot \arctan(x) + \frac{\pi}{2}$	$\psi_{hK} = 2 \cdot \ln\left(\frac{1+x^2}{2}\right)$
	ECUME(6)	$x = (1 - 16\zeta)^{\frac{1}{4}}$	$x = (1 - 16\zeta)^{\frac{1}{4}}$
	COARE3.6	$x = (1 - 15\zeta)^{\frac{1}{4}}$	$x = (1 - 15\zeta)^{\frac{1}{4}}$
Convective		$\psi_{mC} = \frac{3}{2}\ln\left(\frac{1+y+y^2}{3}\right) - \sqrt{3} \cdot \arctan\left(\frac{1+2y}{\sqrt{3}}\right) + \frac{\pi}{\sqrt{3}}$	$\psi_{hC} = \frac{3}{2}\ln\left(\frac{1+y+y^2}{3}\right) - \sqrt{3} \cdot \arctan\left(\frac{1+2y}{\sqrt{3}}\right) + \frac{\pi}{\sqrt{3}}$
	ECUME(6)	$y = (1 - 12.87\zeta)^{\frac{1}{3}}$	$y = (1 - 12.87\zeta)^{\frac{1}{3}}$
	COARE3.6	$y = (1 - 10.15\zeta)^{\frac{1}{3}}$	$y = (1 - 34.15\zeta)^{\frac{1}{3}}$

E

Data Processing R/V Meteor

E.0.1. Euler Angels over Time

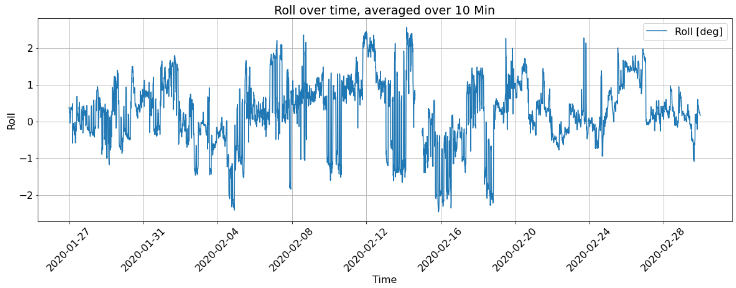

(a) R/V Meteor roll angle, averaged over 10 min

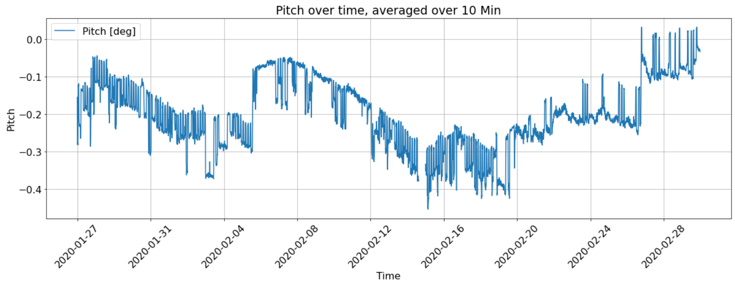

(b) R/V Meteor pitch angle, averaged over 10 min

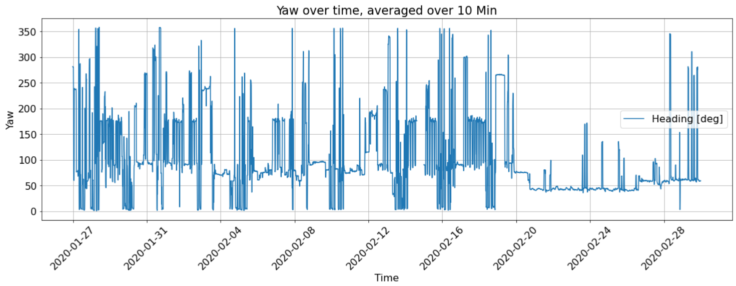

(c) R/V Meteor yaw angle, averaged over 10 min

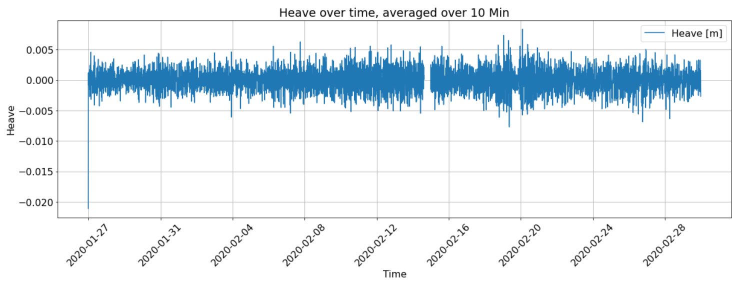

(d) R/V Meteor heave, averaged over 10 min

Figure E.1: Ship motion measurements on R/V Meteor averaged over 10 minutes

E.0.2. Results motion correction

Following time shifting and spike removal, the raw data collected from the R/V Meteor undergoes correction for ship motions. The corrected data is presented in Figures E.2a to E.1d. It should be noted that the average yaw angle of 98.40° has a significant impact on the X and Y components of the wind speeds. The influence of roll and pitch angles, which have mean values of 0.27° and -0.19° respectively, is relatively minor. The vertical component of the wind speed, denoted as the Z component, undergoes a reduction from an average value of 1.6 to 1.56 m/s. Similarly, the horizontal wind speed, represented by the U component, experiences a decrease from an average value of 9.28 to 8.72 m/s.

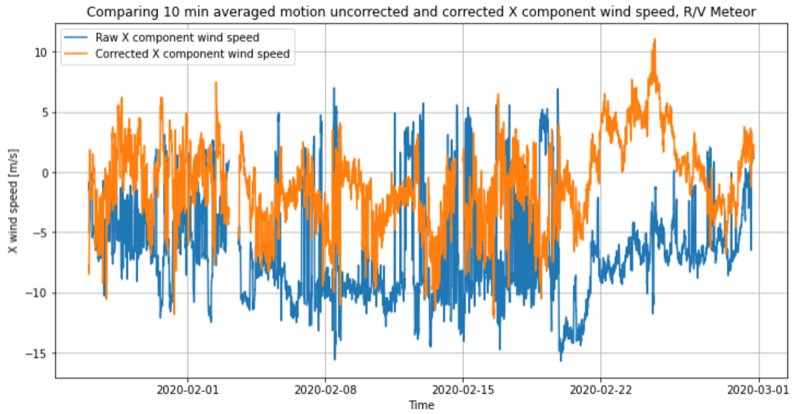

(a) X component wind R/V Meteor

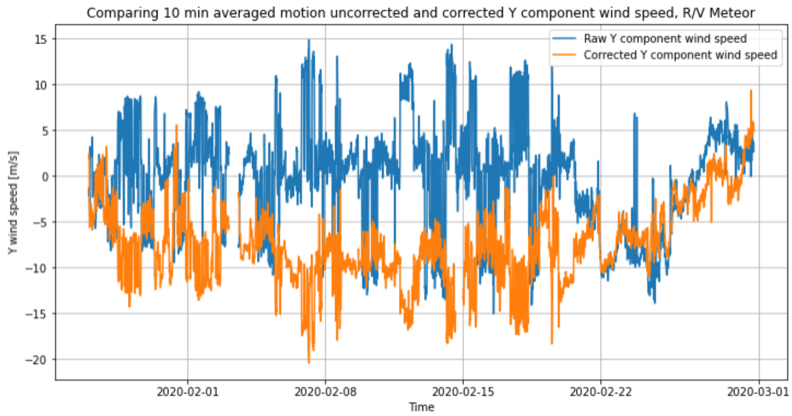

(b) Y component wind R/V Meteor

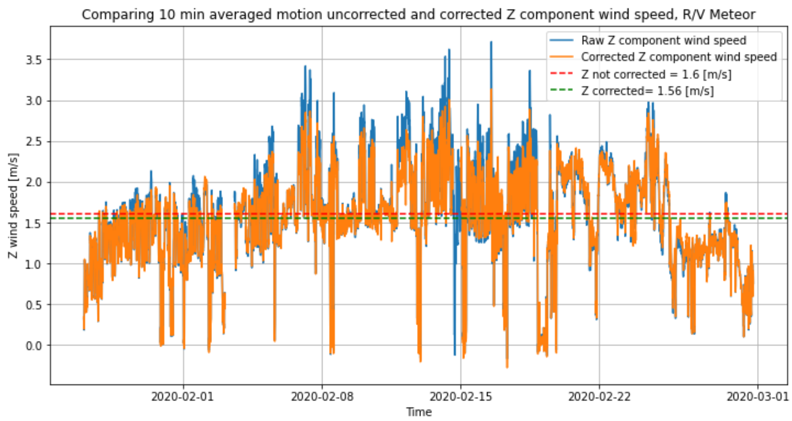

(c) Z component wind R/V Meteor

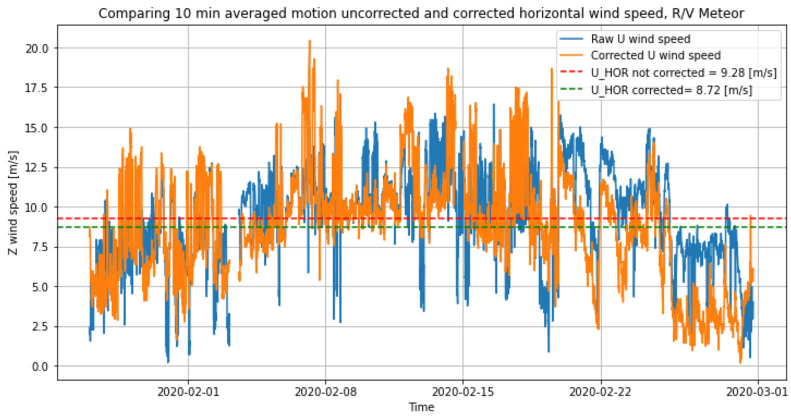

(d) U component wind R/V Meteor

Figure E.1: Effect of motion correction on wind components R/V Meteor

E.0.3. Results masking

The masks employed for the eddy covariance (EC) measurements, as described by (Schirmacher, 2021) in their study on shipborne measurements in the Atlantic, encompass several factors, including waste incineration (mask_chimney), sensor cleaning (mask_before_cleaning), precipitation (mask_rain and mask_DWD_rain), data availability (mask_data_availability), and sea spray (mask_sea_spray). The application of masking enables the identification and exclusion of unreliable or erroneous data points, thereby ensuring the quality and accuracy of the dataset. As depicted in Figures E.2a to E.2c, the application of masks has a significant impact on the EC results. Notably, the removal of outliers and the elimination of incorrect negative latent heat flux (LHF) and sensible heat flux (SHF) values are observed.

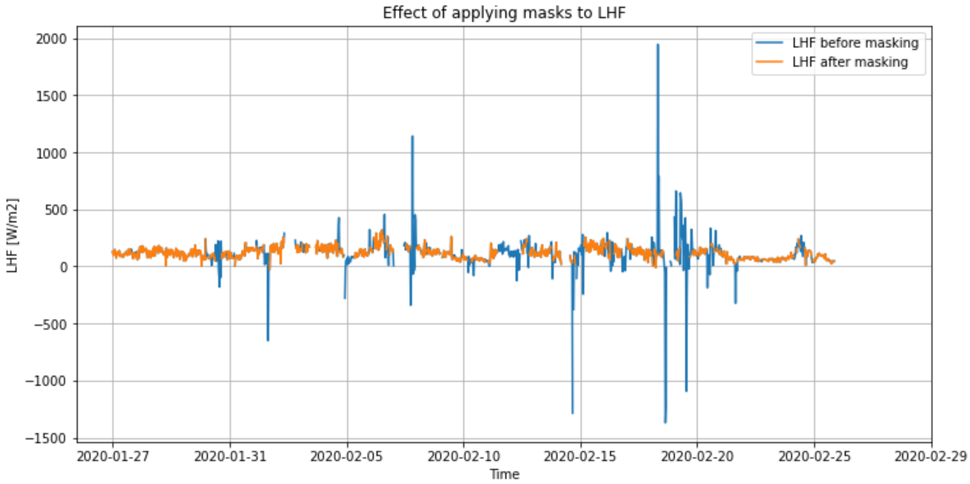

(a) EC LHF R/V Meteor

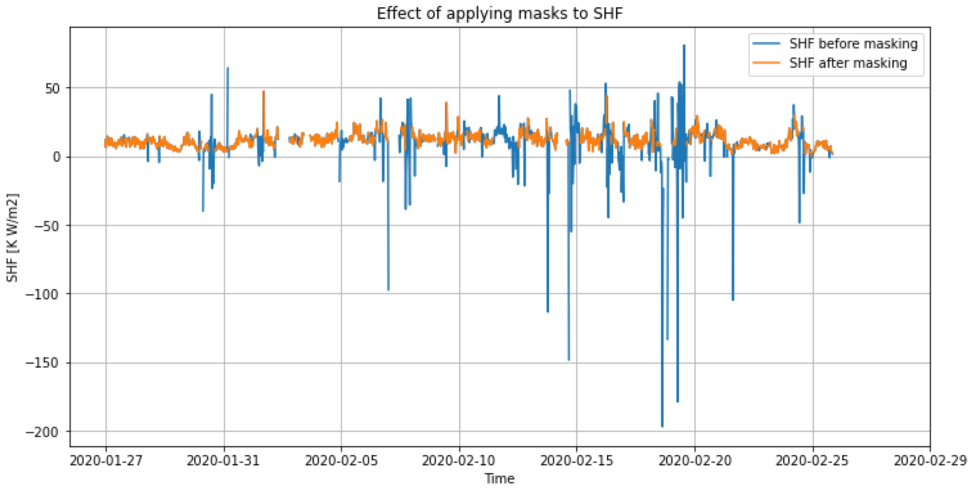

(b) EC SHF R/V Meteor,

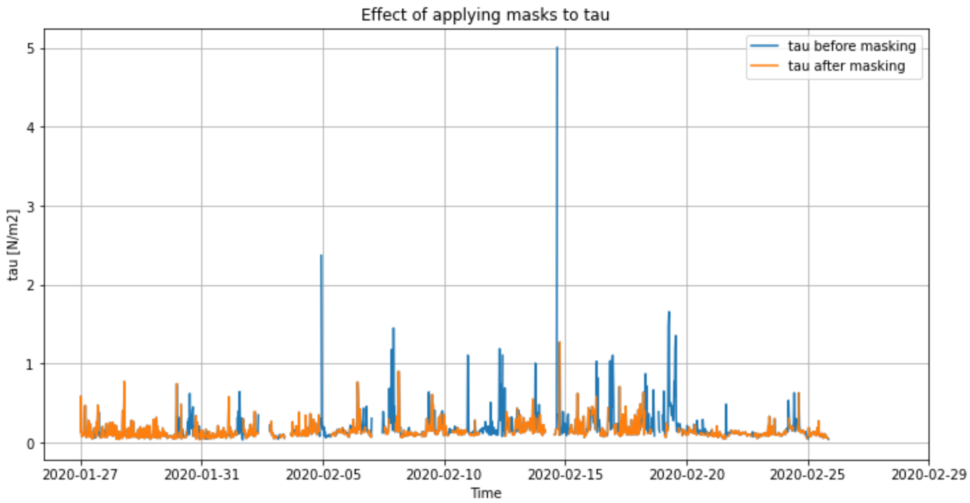

(c) EC Momentum flux R/V Meteor,

Figure E.2: Effect of applying masks to R/V Meteor EC fluxes

F

Masks Uncertainty

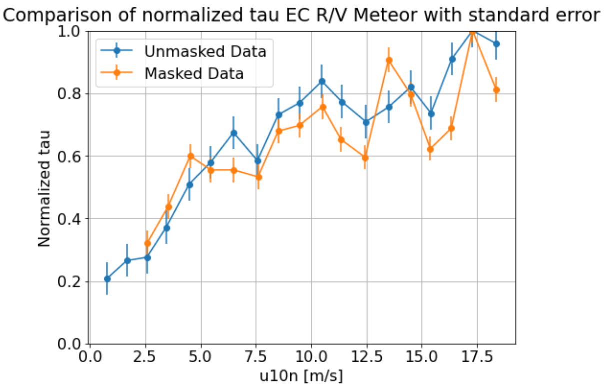

(a) LHF R/V Meteor,

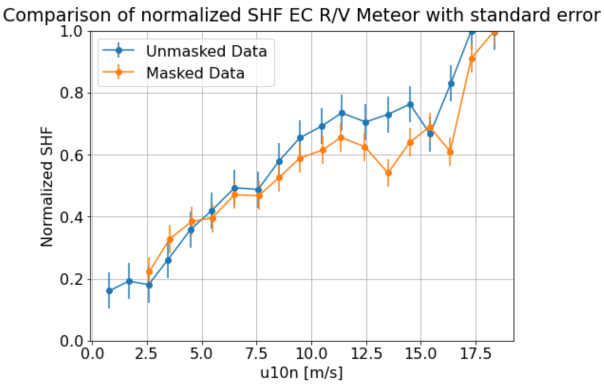

(b) SHF R/V Meteor,

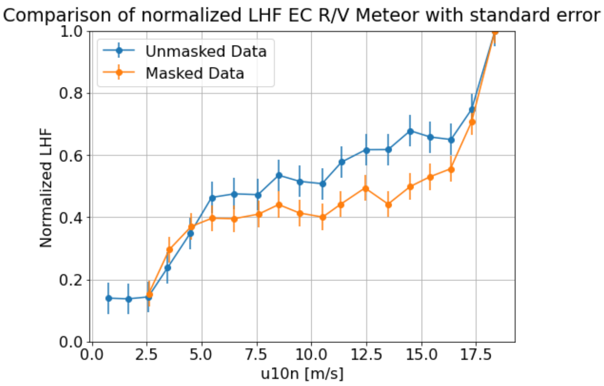

(c) Momentum flux R/V Meteor,

Figure F.1: Comparison of normalized EC fluxes of R/V Meteor, with and without masks, using the standard error

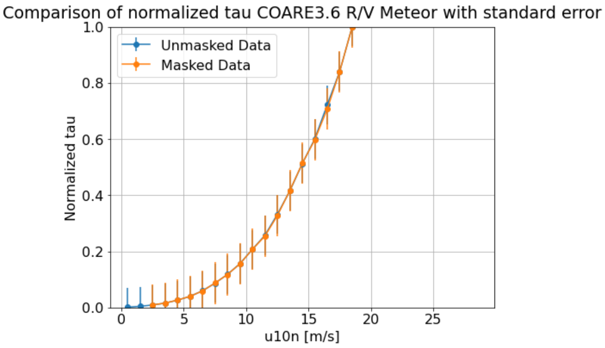

(a) LHF R/V Meteor,

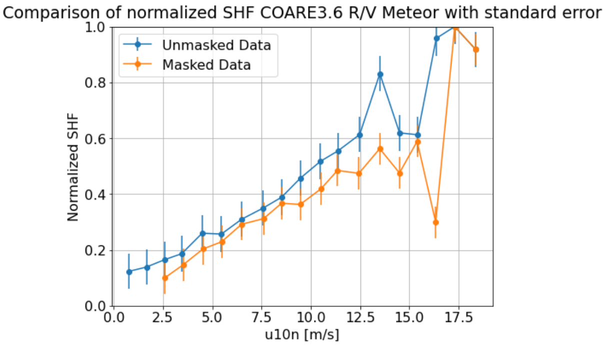

(b) SHF R/V Meteor,

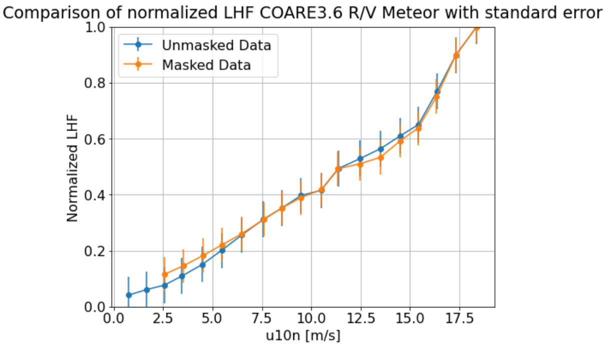

(c) Momentum flux R/V Meteor,

Figure F.2: Comparison of normalized COARE3.6 fluxes of R/V Meteor, with and without masks, using the standard error

G

Temporal Variation of Fluxes

G.1. R/V Ron Brown

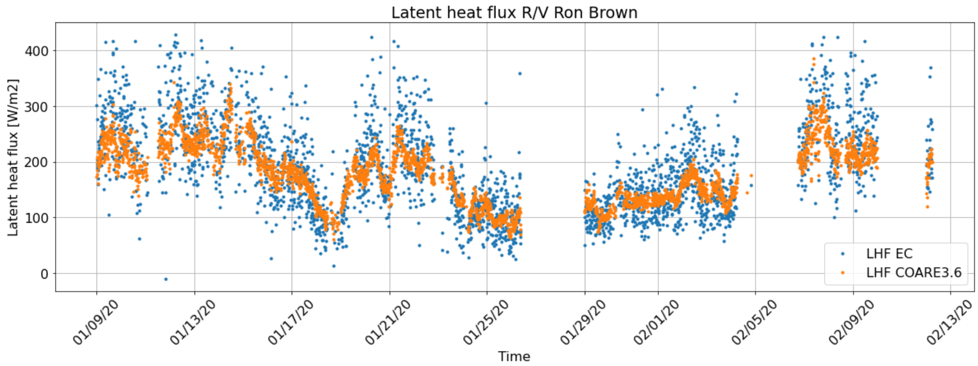

(a) LHF R/V Ron Brown,

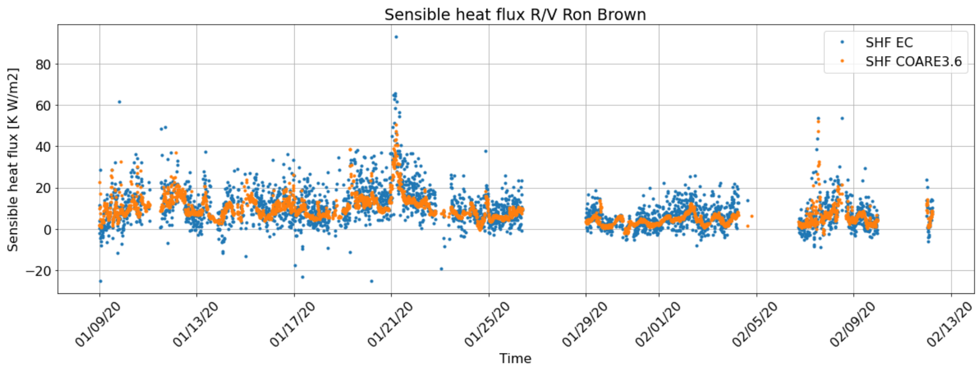

(b) SHF R/V Ron Brown,

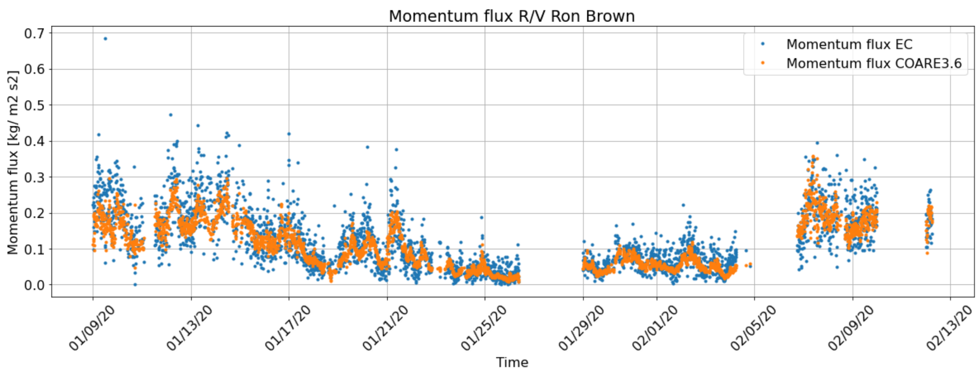

(c) Momentum flux R/V Ron Brown,

Figure G.1: R/V Ron Brown fluxes over time, obtained from EC and bulk method

G.2. R/V Meteor

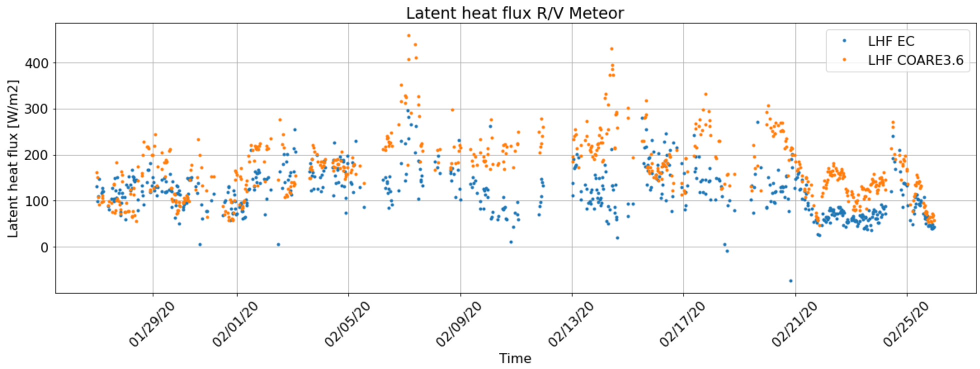

(a) LHF R/V Meteor,

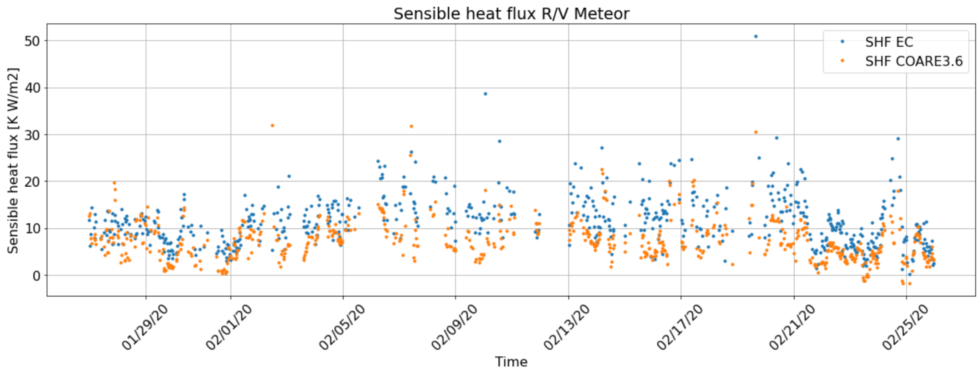

(b) SHF R/V Meteor,

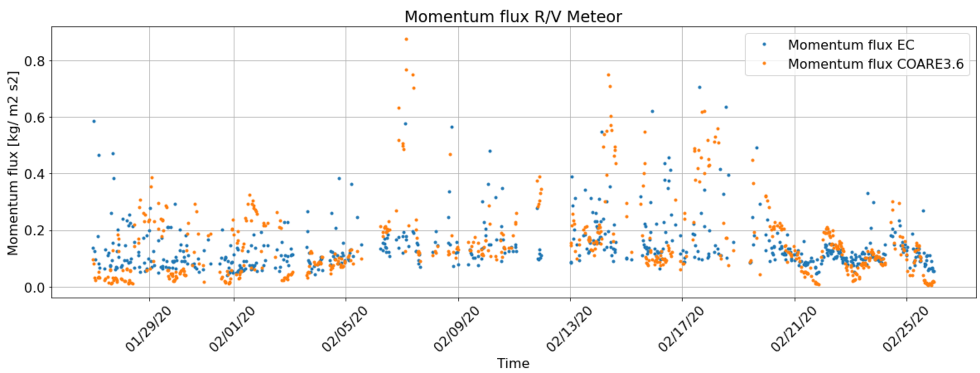

(c) Momentum flux R/V Meteor,

Figure G.2: R/V Meteor fluxes over time, obtained from EC and bulk method

G.3. EC Results Combined

To assess the accuracy of the EC air-sea fluxes obtained from measurements conducted by R/V Ron Brown and R/V Meteor, the results are plotted on a single graph. By examining the overlapping period of the datasets, the accuracy can be examined. However, it should be noted that the results obtained are also dependent on spatial variations.

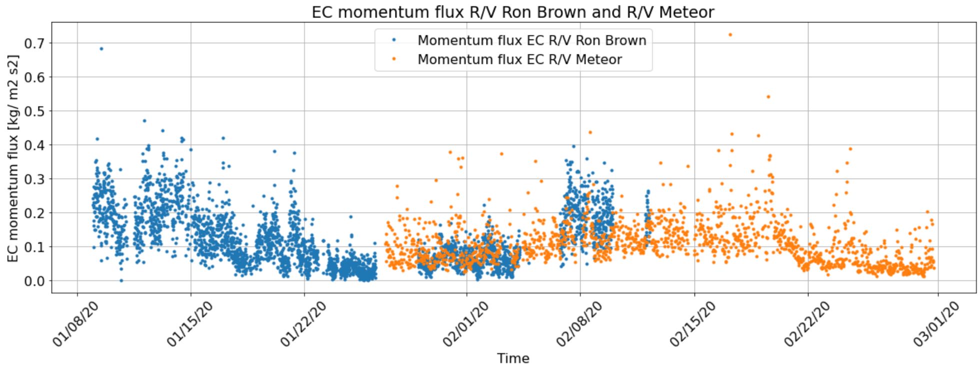

(a) EC LHF R/V Ron Brown and R/V Meteor,

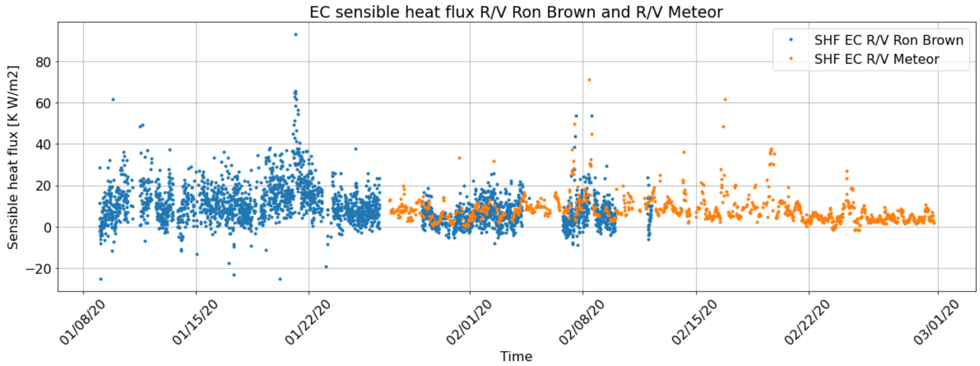

(b) EC SHF R/V Ron Brown and R/V Meteor,

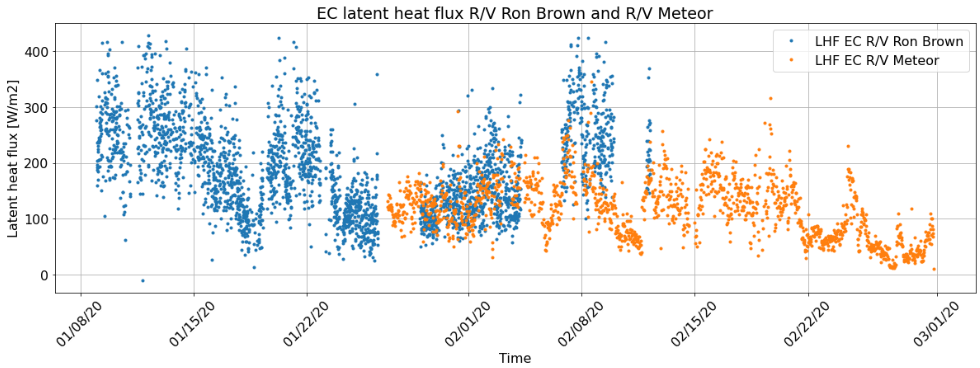

(c) EC Momentum flux R/V Ron Brown and R/V Meteor,

Figure G.3: R/V Ron Brown and R/V Meteor fluxes over time, obtained using the EC method

H

Sensible Heat Flux Diagnostic

H.1. SHF Diagnostics of EC and COARE3.6 obtained from R/V Ron Brown

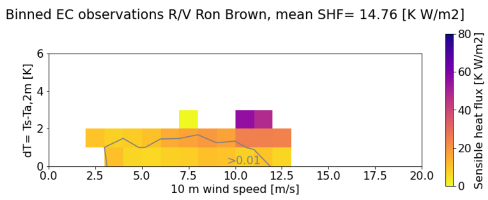

(a) SHF diagnostic EC

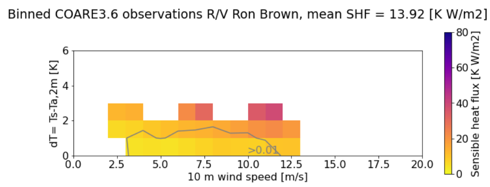

(b) SHF diagnostic COARE3.6

Figure H.1: EC and COARE3.6 SHF diagnostics for R/V Ron Brown

H.2. SHF Diagnostics of EC and COARE3.6 obtained from R/V Meteor

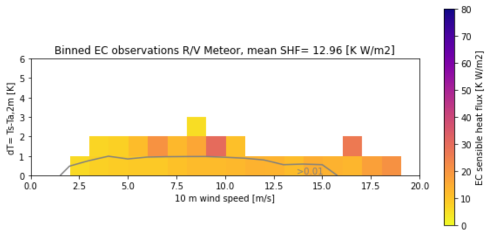

(a) SHF diagnostic EC

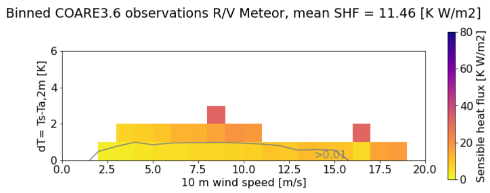

(b) SHF diagnostic COARE3.6

Figure H.2: EC and COARE3.6 SHF diagnostics for R/V Meteor

H.3. SHF Diagnostics of ECUME and ECUME6

H.3.1. R/V Ron Brown domain

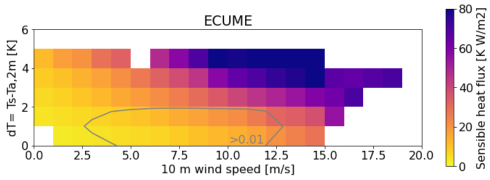

(a) SHF diagnostic ECUME

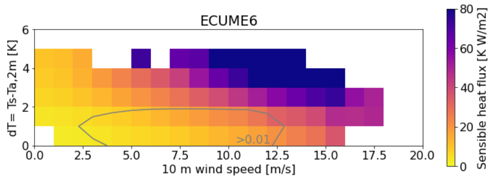

(b) SHF diagnostic ECUME6

Figure H.3: SHF diagnostics for ECUME and ECUME6 using the R/V Ron Brown domain

H.3.2. R/V Meteor domain

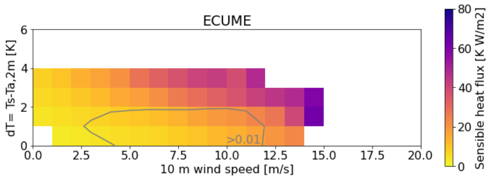

(a) SHF diagnostic ECUME

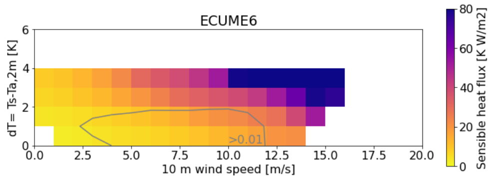

(b) SHF diagnostic ECUME6

Figure H.4: SHF diagnostics for ECUME and ECUME6 using the R/V Meteor domain

Momentum Flux Heat Flux Diagnostic

I.1. Momentum Flux Diagnostic of EC obtained from R/V Ron Brown

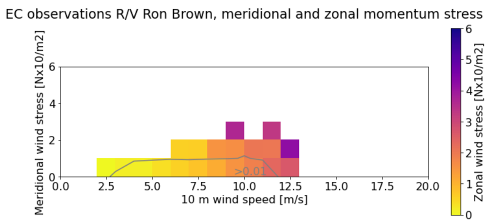

(a) Momentum flux diagnostic zonal wind

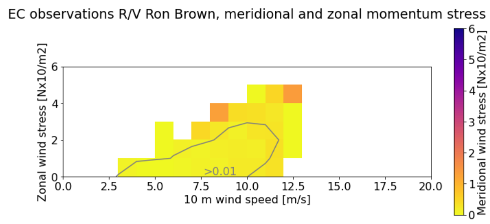

(b) Momentum flux diagnostic meridional wind

Figure I.1: Momentum Flux Diagnostics for EC R/V Ron Brown

I.2. Momentum Flux Diagnostic of EC obtained from R/V Meteor

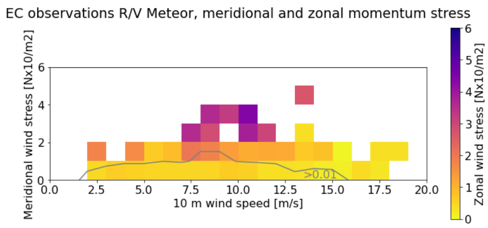

(a) Momentum flux diagnostic zonal wind

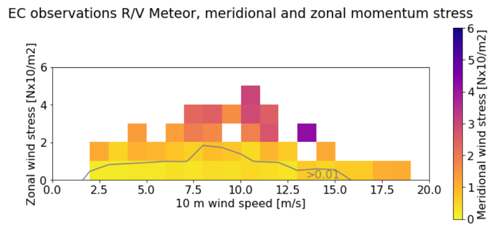

(b) Momentum flux diagnostic meridional wind

Figure I.2: Momentum Flux Diagnostics for EC R/V Meteor

I.3. Momentum Flux Diagnostics of ECUME and ECUME6

I.3.1. R/V Ron Brown domain

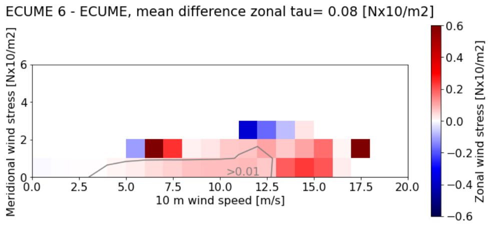

(a) Momentum flux diagnostic zonal wind

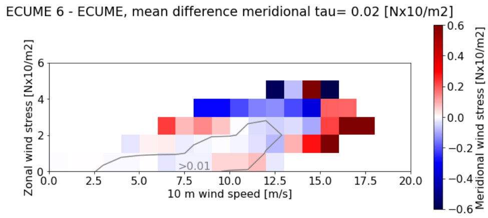

(b) Momentum flux diagnostic meridional wind

Figure I.3: Comparing momentum flux ECUME and ECUME6 using the R/V Ron Brown domain

I.3.2. R/V Meteor domain

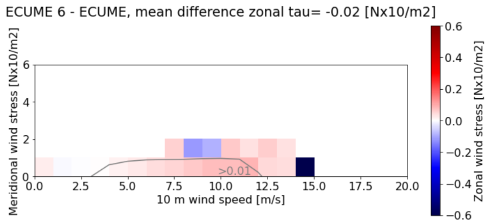

(a) Momentum flux diagnostic zonal wind

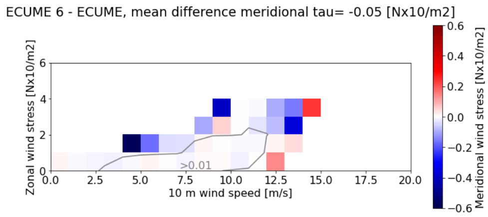

(b) Momentum flux diagnostic meridional wind

Figure I.4: Comparing momentum flux ECUME and ECUME6 using the R/V Meteor domain

I.4. Momentum Flux Diagnostic for ECUME and ECUME6 compared to EC observations

I.4.1. R/V Ron Brown domain

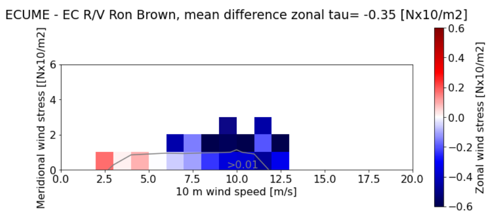

(a) Momentum flux diagnostic zonal wind

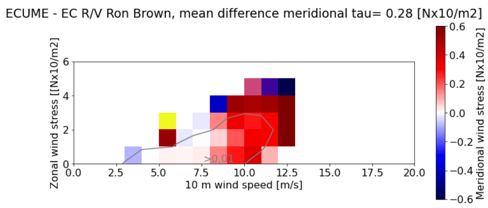

(b) Momentum flux diagnostic meridional wind

Figure I.5: Comparing momentum flux ECUME and EC obtained from R/V Ron Brown

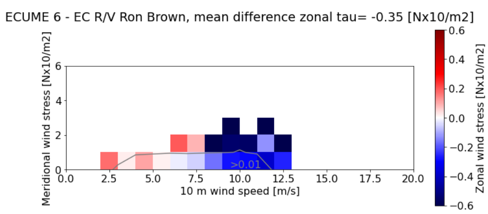

(a) Momentum flux diagnostic zonal wind

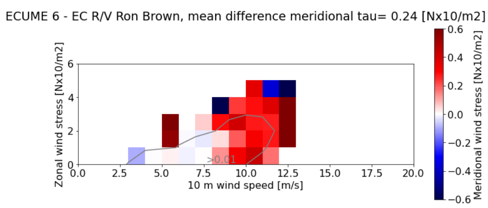

(b) Momentum flux diagnostic meridional wind

Figure I.6: Comparing momentum flux ECUME6 and EC obtained from R/V Ron Brown

I.4.2. R/V Meteor domain

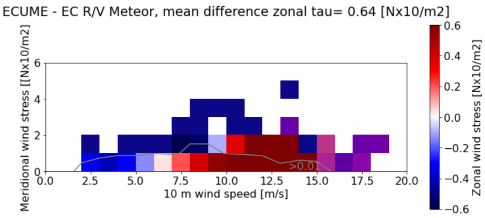

(a) Momentum flux diagnostic zonal wind

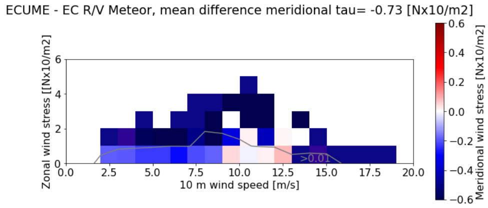

(b) Momentum flux diagnostic meridional wind

Figure I.7: Comparing momentum flux ECUME and EC obtained from R/V Meteor

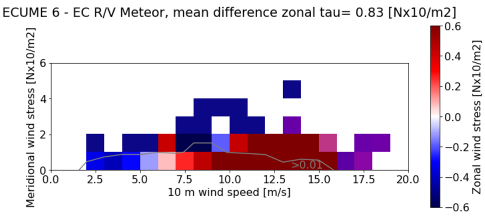

(a) Momentum flux diagnostic zonal wind

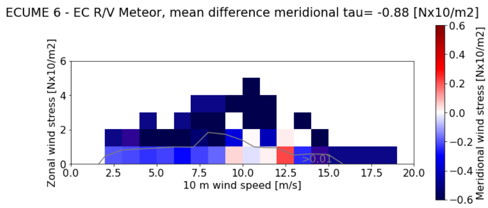

(b) Momentum flux diagnostic meridional wind

Figure I.8: Comparing momentum flux ECUME6 and EC obtained from R/V Meteor

J Relative Error Flux Diagnostic

J.1. Relative Error for Latent Heat Flux Diagnostic

J.1.1. ECUME compared to EC observations

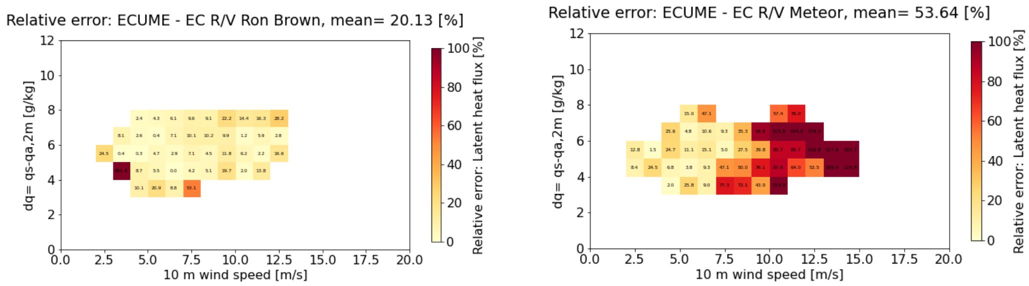

(a) R/V Ron Brown (b) R/V Meteor

Figure J.1: Relative error LHF diagnostic comparing ECUME to EC

J.1.2. ECUME comapred to COARE3.6

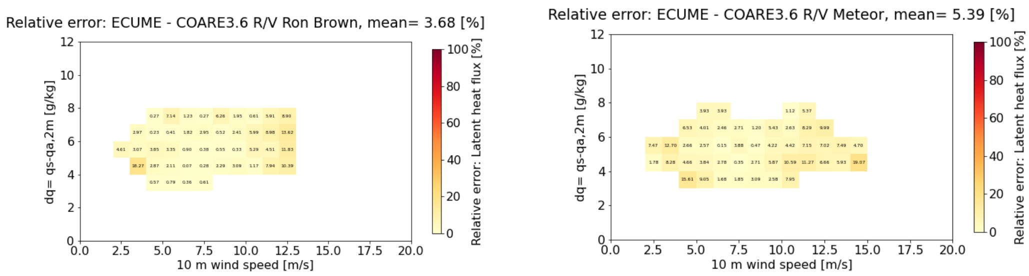

(a) R/V Ron Brown (b) R/V Meteor

Figure J.2: Relative error LHF diagnostic comparing ECUME to COARE3.6

J.1.3. ECUME6 compared to EC observations

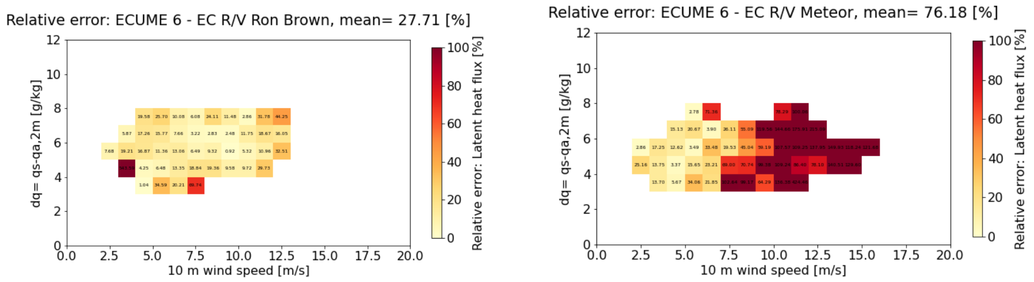

(a) R/V Ron Brown (b) R/V Meteor

Figure J.3: Relative error LHF diagnostic comparing ECUME6 to EC

J.1.4. ECUME6 compared to COARE3.6

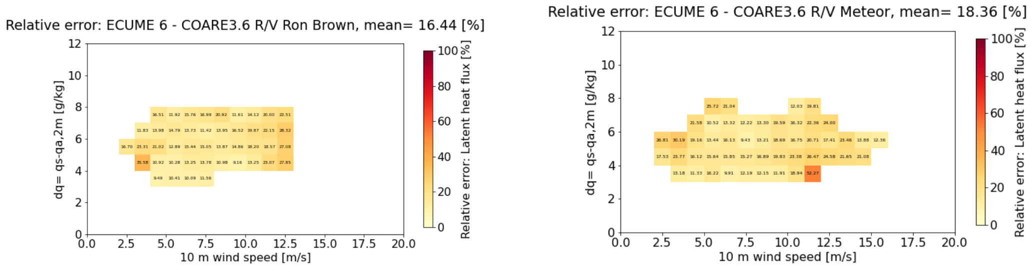

(a) R/V Ron Brown (b) R/V Meteor

Figure J.4: Relative error LHF diagnostic comparing ECUME6 to COARE3.6

J.2. Relative Error for Sensible Heat Flux Diagnostic

J.2.1. ECUME compared to EC observations

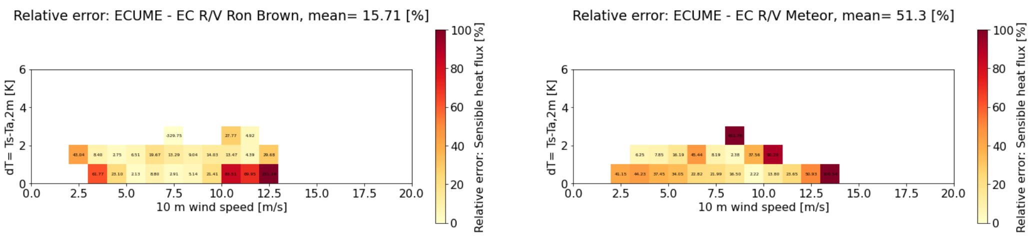

(a) R/V Ron Brown (b) R/V Meteor

Figure J.5: Relative error SHF diagnostic comparing ECUME to EC

J.2.2. ECUME compared to COARE3.6 observations

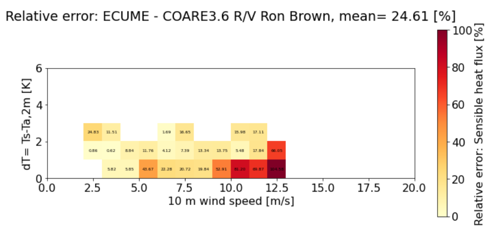

(a) R/V Ron Brown

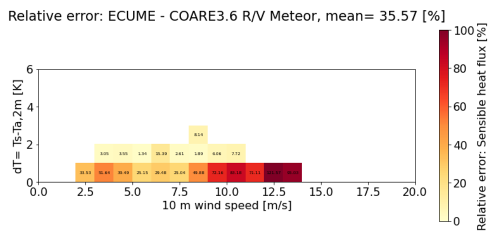

(b) R/V Meteor

Figure J.6: Relative error SHF diagnostic comparing ECUME to COARE3.6

J.2.3. ECUME6 compared to EC observations

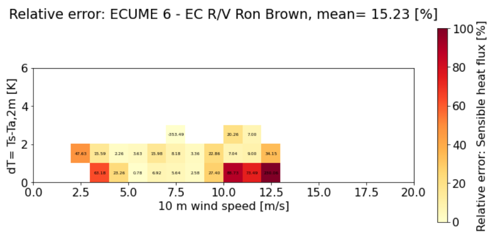

(a) R/V Ron Brown

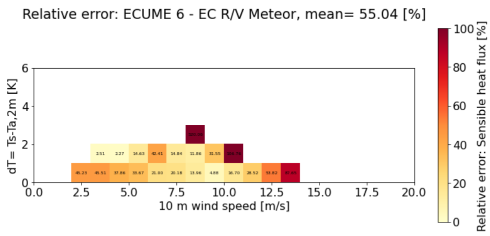

(b) R/V Meteor

Figure J.7: Relative error SHF diagnostic comparing ECUME6 to EC

J.2.4. ECUME6 compared to COARE3.6

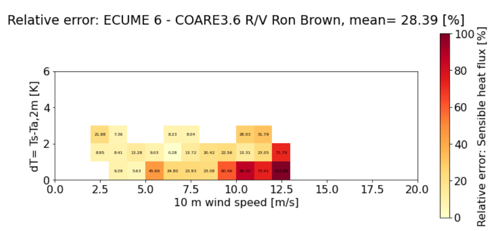

(a) R/V Ron Brown

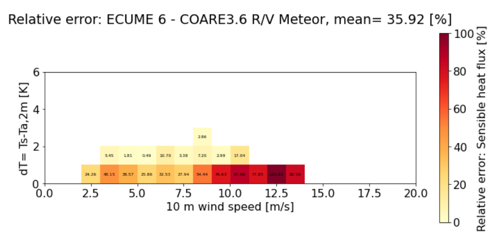

(b) R/V Meteor

Figure J.8: Relative error SHF diagnostic comparing ECUME6 to COARE3.6

K

Characteristic Scales Comparison

Using the developed ECUME and COARE3.6 models, the iteratively obtained characteristic temperature scales (θ_*) and characteristic moist scales (q_*) are compared. The Figures K.1a and K.1b show the results, by plotting against the 10 m wind speed. As depicted, the values for θ_* and q_* are negative, which is attributed to the negative differences $\Delta\theta = \theta_a - \theta_s$ and $\Delta q = q_a - q_s$. The comparison for the friction velocity is represented in Figure 4.30a in Chapter 4.3.4.

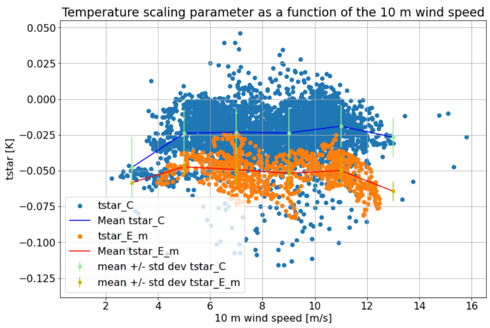

(a) Characteristic temperature scale

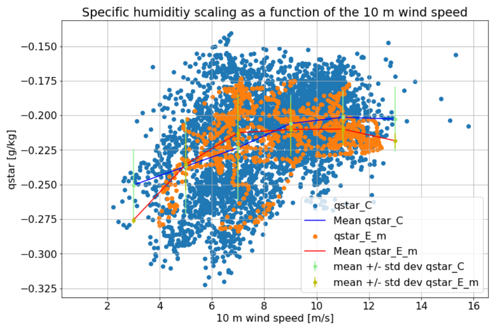

(b) Characteristic moist scale

Figure K.1: Comparing the characteristic temperature (θ_*) and characteristic moist (q_*) scale determined using COARE3.6 and ECUME